



**Collective cancer cell invasion *in vivo*:
function of $\beta 1$ and $\beta 3$ integrins in perivascular invasion and
resistance to therapy**

Kollektive Tumorzellinvasion *in vivo*: Funktion von $\beta 1$ und $\beta 3$ Integrinen
in perivaskulärer Invasion und Therapieresistenz

Doctoral thesis for a doctoral degree
at the Graduate School of Life Sciences,
Julius-Maximilians-Universität Würzburg,
Section Biomedicine

submitted by

Stephanie Alexander

from

Cottbus

Würzburg, 2010

Submitted on: April 30, 2010

Members of the *Promotionskomitee*:

Chairperson: Prof. Ulrike Holzgrabe

Primary Supervisor: Prof. Peter Friedl

Supervisor (Second): Prof. Manfred Scharl

Supervisor (Third): Prof. Helga Stopper

Date of Public Defence:

Date of Receipt of Certificates:

TABLE OF CONTENTS		Page
1	ABSTRACT/ZUSAMMENFASSUNG	7/8
2	INTRODUCTION	9
2.1	Invasion of cancer	9
2.1.1	Principles of cancer cell invasion	10
2.1.1.1	Individual cell migration	10
2.1.1.2	Collective cell migration in morphogenesis and regeneration	11
2.1.1.3	Collective migration and invasion of cancer	13
2.1.1.4	Plasticity of tumor cell migration	14
2.1.2	Molecules involved in migration and invasion	15
2.1.2.1	Cell adhesion molecules	15
2.1.2.2	Matrix degradation	17
2.1.2.3	Pro-migratory signaling	18
2.1.2.4	Cell-cell adhesion molecules	19
2.2	Models of cancer cell invasion	20
2.2.1	Experimental models to investigate migration and invasion	20
2.2.1.1	<i>In vitro</i> models	20
2.2.1.2	Interstitial <i>in vivo</i> models	22
2.2.2	Biological models	24
2.2.2.1	Fibrosarcoma	25
2.2.2.2	Melanoma	26
2.3	Microscopical techniques to study invasion <i>in vivo</i>	27
2.4	Purpose of the study	29
3	RESULTS	30
3.1	Advantages of near-infrared and infrared multiphoton microscopy for intravital imaging	30
3.1.1	Two-photon excitation and emission spectra of red dyes and fluorescent proteins	30
3.1.2	Photobleaching and photodamage	31
3.1.3	Deep tissue imaging	32
3.2	Establishment of a modified orthotopic intradermal tumor xenograft model to monitor <i>in vivo</i> growth and invasion	33
3.2.1	Modification of the dorsal skinfold chamber towards a 3D environment	34
3.2.2	Kinetics of tumor growth	35
3.2.3	Kinetics of mitosis and apoptosis	36
3.2.4	Temperature dependence of intradermal tumor models	37

3.3	Efficient and diverse fibrosarcoma invasion <i>in vivo</i>	38
3.3.1	Diversity of invasion modes	38
3.3.2	Visualizing the tumor-stroma interface and guidance structures of invasion	39
3.3.2.1	Collagen, muscle strands and fat tissue	39
3.3.2.2	Lymphatic Vessels	39
3.3.2.3	Blood Vessels	40
3.3.3	Invasive growth	41
3.3.3.1	Invasion efficiency	41
3.3.3.2	Components of invasive growth	42
3.3.4	Collective invasion in human fibrosarcoma	44
3.4	Growth and invasion of orthotopic melanoma models	44
3.4.1	Growth of orthotopic melanoma lesions	45
3.4.2	Pigment-induced phototoxicity in B16/F10 lesions – limitations for multiphoton microscopy	46
3.4.3.	Invasion pattern	46
3.4.4	Invasive growth of melanoma	48
3.5	Collective invasion: a radioresistance niche	49
3.5.1	Radiation therapy: Heterogeneity of response	49
3.5.1.1	Heterogenous response rate to irradiation	49
3.5.1.2	Heterogeneity between mitosis and apoptosis	50
3.5.1.3	Heterogeneity between main mass and invasion strands	51
3.5.2	Radioresistance of human melanoma (MV3)	53
3.6	Molecular mechanisms of collective invasion and radioresistance	54
3.6.1	Radioresistance despite chemotherapy (doxorubicin)	54
3.6.2	Epidermal growth factor	56
3.6.3	Integrins	57
3.6.3.1	Establishment of stable knockdown cell lines	58
3.6.3.1.1	Knock down of β 1 integrin	58
3.6.3.1.2	Double knockdown of β 1 and β 3 integrin	59
3.6.3.2	<i>In vitro</i> characterization of β 1RNAi and β 1/ β 3RNAi cells	60
3.6.3.3	Role of β 1 and β 3 integrin in tumor progression <i>in vivo</i>	61
3.6.3.3.1	Tumor growth	61
3.6.3.3.2	Role of β 1 and β 3 integrins in collective invasion	63
3.6.3.4	Prevention of radioresistance by β 1 and β 3 integrin knockdown	64

4	DISCUSSION	67
4.1	Improved tissue penetration and imaging of red dyes using IR-MPM	67
4.2	Impact of the implantation site and maintenance temperature on biology of tumor lesions (dorsal skinfold chamber)	68
4.3	Collective cancer invasion in fibrosarcoma and melanoma: principles, guidance and plasticity	69
4.3.1	Diversity of invasion <i>in vivo</i> : Collective invasion is predominant in fibrosarcoma and melanoma lesions	70
4.3.2	Components of invasive growth <i>in vivo</i>	71
4.3.3	Guidance and mechanisms of migration	72
4.3.3.1	Path of least resistance	73
4.3.3.2	Contact guidance	74
	a) Structural components	
	b) Cellular components	
4.3.3.3	Chemotaxis and microenvironmental factors	75
4.3.4	Match of preclinical mouse model with human disease: similarities and differences	76
4.4	Microenvironmental control of altered biology in collective invasion strands: identification of a resistance niche	77
4.4.1	Altered tumor microenvironment	77
4.4.2	Altered biology of tumor cells	78
4.4.2.1	Radiation and chemoresistance	78
4.4.2.2	Importance of $\beta 1$ and $\beta 3$ integrins <i>in vivo</i> : pro-survival rather than pro-invasion functions	80
4.4.2.3	$\beta 1$ and $\beta 3$ integrin mediating radioresistance	81
4.5	Implications for human therapy: be aware of the invasive niche!	82
4.5.1	Deep tissue invasion: a matter of resection margins	82
4.5.2	Anti-angiogenic therapy: no matter regarding early invasion	83
4.5.3	Radio- and chemotherapy: a matter of tumor-compartment	83
4.5.4	Multimodal therapy: Key to success!	84
4.6	Concluding remarks	86
5	MATERIAL & METHODS	87
5.1	Antibodies, Pharmaceuticals, Inhibitors	87
5.2	Cells and cell culture	88
5.3	Generation of stable knockdown cell lines by lentiviral shRNA	88
5.4	In vitro assays for proliferation, migration and protein expression	89
5.4.1	Cell proliferation	89
5.4.2	Cell migration assays	89

5.4.3	Flow cytometry	89
5.4.4	Protein gelelectrophoreses and Western Blot	90
5.5	Dorsal skinfold chamber (DSFC) model	90
5.6	Histochemistry	91
5.6.1	Dorsal skinfold chamber skin	91
5.6.2	Human primary fibrosarcoma samples (carried out by Uta Flucke)	91
5.7	Bright-field time-lapse videomicroscopy	92
5.8	Confocal microscopy	92
5.9	Near-infrared and infrared multiphoton microscopy (NIR- and IR-MPM)	92
5.9.1	Microscope components	92
5.9.2	Spectroscopy	93
5.9.3	Time-lapse microscopy of photobleaching, photodamage and migration	93
5.9.4	Intravital microscopy	94
5.10	Image analysis	94
5.11	Statistical analysis	94
6	REFERENCES	95
7	APPENDIX	106
	Abbreviations	106
	Movie legend	108
	List of figures	109
	List of tables	110
	Acknowledgement	111
	Curriculum vitae including list of publications	112
	Affidavit	115
	CD-ROM with movies	

Pro-migratory signals mediated by the tumor microenvironment contribute to the cancer progression cascade, including invasion, metastasis and resistance to therapy. Derived from *in vitro* studies, isolated molecular steps of cancer invasion programs have been identified but their integration into the tumor microenvironment and suitability as molecular targets remain elusive. The purpose of the study was to visualize central aspects of tumor progression, including proliferation, survival and invasion by real-time intravital microscopy. The specific aims were to monitor the kinetics, mode, adhesion and chemoattraction mechanisms of tumor cell invasion, the involved guidance structures, and the response of invasion zones to anti-cancer therapy. To reach deeper tumor regions by optical imaging with subcellular resolution, near-infrared and infrared excited multiphoton microscopy was combined with a modified dorsal skinfold chamber model. Implanted HT-1080 fibrosarcoma and B16/F10 and MV3 melanoma tumors developed zones of invasive growth consisting of collective invasion strands that retained cell-cell contacts and high mitotic activity while invading at velocities of up to 200 μm per day. Collective invasion occurred predominantly along preexisting tissue structures, including blood and lymph vessels, collagen fibers and muscle strands of the deep dermis, and was thereby insensitive to RNAi based knockdown and/or antibody-based treatment against $\beta 1$ and $\beta 3$ integrins, chemokine (SDF-1/CXCL12) and growth factor (EGF) signaling. Therapeutic hypofractionated irradiation induced partial to complete regression of the tumor main mass, yet failed to eradicate the collective invasion strands, suggesting a microenvironmentally privileged niche. Whereas no radiosensitization was achieved by interference with EGFR or doxorubicin, the simultaneous inhibition of $\beta 1$ and $\beta 3$ integrins impaired cell proliferation and survival in spontaneously growing tumors and strongly enhanced the radiation response up to complete eradication of both main tumor and invasion strands. In conclusion, collective invasion *in vivo* is a robust process which follows preexisting tissue structures and is mainly independent of established adhesion and chemoattractant signaling. Due to its altered biological response to irradiation, collective invasion strands represent a microenvironmentally controlled and clinically relevant resistance niche to therapy. Therefore supportive regimens, such as anoikis-induction by anti-integrin therapy, may serve to enhance radio- and chemoefficacy and complement classical treatment regimens.

ZUSAMMENFASSUNG

Die Progression von Tumorerkrankungen, einschließlich Tumorinvasion, Metastasierung und Therapieresistenz wird unter anderem durch migrationsfördernde Signale aus der Tumorumgebung vermittelt. Zur bisherigen Aufklärung einzelner Schritte des Tumorinvasions- und Progressionsprogramms trugen dabei wesentlich *In-vitro*-Studien bei, jedoch erfordert die Darstellung der Relevanz molekularer Zielstrukturen und deren Funktion im Tumormikromilieu die Validierung in geeigneten *In-vivo*-Tumormodellen. Ziel dieser Studie war, zelluläre und molekulare Mechanismen der Tumorprogression inklusive Proliferation, Überleben und Invasion mittels Echtzeit-Intravitalmikroskopie darzustellen. Untersucht wurden insbesondere die Kinetik und Arten der Tumorzellinvasion, die zugrunde liegenden Adhäsionswege und pro-migratorischen Signale (EGF, SDF-1), beteiligte Leitstrukturen des Tumorstromas, und Strategien, therapeutisch gegen Invasionszonen vorzugehen. Um tiefe Tumorareale mittels subzellulär aufgelöster optischer Bildgebung zu erreichen, wurde nah-infrarote und infrarote Multiphotonenmikroskopie mit einem modifizierten Rückenkammermodell kombiniert. Orthotope Xeno- und Allotransplantate von HT-1080-Fibrosarkom- und B16/F10- oder MV3-Melanomzellen entwickelten dabei ausgeprägte invasive Wachstumszonen bestehend aus kollektiven Invasionssträngen mit intakten Zell-Zell-Kontakten und zeitgleicher Mitoseaktivität, die Geschwindigkeiten von bis zu 200 μm pro Tag erreichten. Diese kollektive Invasion orientierte sich bevorzugt entlang von Funktionsstrukturen der tiefen Dermis wie Blut- und Lymphgefäßen, Kollagenfasern und Muskelsträngen. RNAi-basierende Herunterregulation und/oder Injektion blockierender Antikörper gegen $\beta 1$ und $\beta 3$ Integrine, wie auch Inhibition von EGF führten nur zu minimaler Änderung der Invasioneffizienz. Therapeutische hypofraktionierte Bestrahlung induzierte partielle bis komplette Regression der Tumormasse, nicht jedoch der kollektiven Invasionsstränge, was auf eine kombinierte Invasions- und Resistenznische hinweist. Weder Doxorubicin noch gegen EGFR gerichtete Antikörper steigerten die Radiosensitivität, jedoch führte die simultane Inhibition von $\beta 1$ und $\beta 3$ Integrinen zu einer starken Hemmung von Proliferation und Überleben spontan wachsender Tumoren (Anoikis) und verstärkte die Strahlungssensitivität bis hin zum kompletten Verschwinden von sowohl Tumormasse wie auch Invasionssträngen. Kollektive Invasion ist somit ein wichtiger Invasionsmodus, der sich an vorbestehenden Gewebsstrukturen orientiert und unabhängig von Integrinen und EGF- und SDF-1-Signalen erfolgt. Die kollektiven Stränge entwickeln dabei eine vom Haupttumor verschiedene biologische Reaktion auf Bestrahlung und entsprechen damit einer durch die Mikroumgebung kontrollierten und von Integrinsignalen abhängenden Resistenznische. Somit könnte eine zusätzliche anti-Integrin-Therapie die Effizienz von Bestrahlung und Chemotherapie erhöhen und klassische Behandlungsschemen/-programme ergänzen.

2 INTRODUCTION

Migration and invasion are essential processes for cells to change their position during embryonic development, wound healing, and immune response, as well as, pathologically, during cancer cell invasion and metastasis. The invasive and metastatic potential of tumors is thereby of central importance for prognosis of affected patients. Although many research studies are concerned with the molecular mechanisms underlying invasion, the invasive process *in vivo* and its interdependence with the tumor microenvironment are poorly understood. To date orthotopic tumor models in small animals that reflect pathogenesis of tumors in all its aspects and especially invasion processes are still rare and often poorly validated towards human tumor disease.

2.1 Invasion of cancer

To spread within tissues, tumor cells utilize migration mechanisms similar or identical to those used by normal, non-neoplastic cells during physiological processes like embryonic development, angiogenesis, wound healing, and immune response.

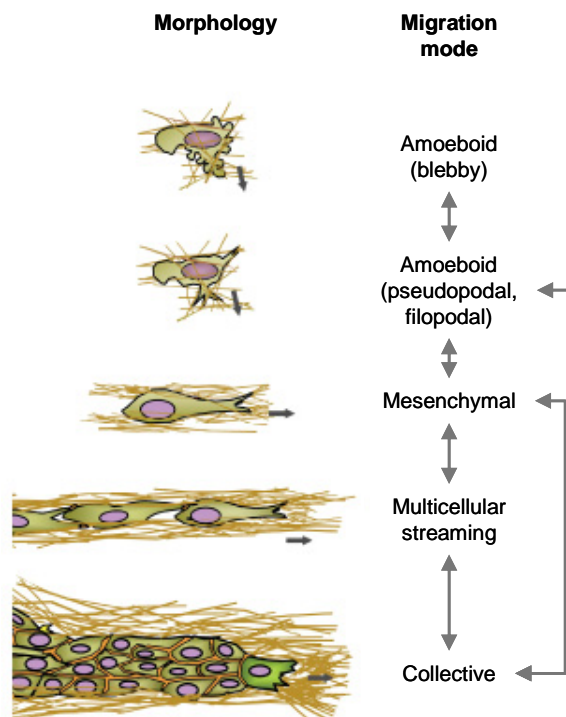


Figure 1. Cell morphologies and nomenclature of migration modes. The nomenclature of interstitial migration modes is based on typical cell morphology (rounded or spindle-shaped) and pattern (individual, loosely connected, or collective). Each migration mode is dependent on a set of molecular mechanisms, the regulation of which can change the style of migration. Most widely studied examples for alterations of migration mode are the mesenchymal-to-amoeboid transition or the collective-to-individual transition. Arrows in morphology schemes, direction of migration. Arrows in between migration modes, described transitions. Taken from Friedl P & Wolf K, 2010¹.

2.1.1 Principles of cancer cell invasion

In vitro and *in vivo* studies have shown that tumor cells invade the surrounding tissue in diverse patterns. They can disseminate as individual cells – amoeboid or mesenchymal, or expand in solid multicellular strands, sheets, files or clusters, termed collective migration (Fig. 1)¹⁻³.

Whereas prerequisites and mechanisms of single-cell cancer migration are well studied, collective invasion is less understood and its investigation is increasingly difficult based on the underlying biological complexity and technical demands on migration models.

2.1.1.1 Individual cell migration

In solid tumors, individual motile tumor cells originate from the interstitial stroma or from a multicellular compartment, such as epithelium. After loosening their cell contacts, individual cells detach and migrate through the adjacent connective tissue⁴. Based on cell type, integrin engagement, cytoskeletal structure and protease production, single-cell migration can occur in different morphological variants:

Mesenchymal movement. Mesenchymal cells move via a five-step migration cycle²: (1) actin-driven protusion of the leading edge, (2) cell-matrix interaction and formation of focal contacts, (3) recruitment of surface proteases to extracellular matrix (ECM) contacts and focalized proteolysis, (4) cell contraction by actomyosin, and (5) detachment of the trailing edge. Further, they appear fibroblast-like spindle-shaped (Fig. 1) and are dependent on integrin-mediated adhesion dynamics^{2,5,6}. Mesenchymal movement is predominantly found in cells from connective tissue tumors, such as fibrosarcoma⁷ or melanoma⁸, in epithelial cancers following progressive dedifferentiation⁹, or in gliomas⁶.

Amoeboid migration. The characteristics of this movement have been established through studies of the single cell amoeba, *Dictyostelium discoideum*¹⁰ and the underlying molecular mechanisms are varying, but generally include weak adhesion to the ECM and physical adaptation to preformed matrix structures, extension of lateral footholds^{11,12}, and the formation of constriction rings at regions of narrow space^{13,14} (Fig. 1). Such shape-driven migration allows cells to circumnavigate, rather than degrade, their ECM barriers. These cells are highly deformable, due to their lack of focal contacts, allowing them to move at 10- to 30-fold higher velocities than cells that use mesenchymal migration mechanisms¹³⁻¹⁵. In higher eukaryotes, signs of amoeboid movement are retained in leukocytes and some tumor cells^{10,16-18}. Amoeboid migration has been shown for lymphoma and myeloic leukaemia cells¹⁹, carcinoma cells from kidney and lung^{20,21}, but also for fibrosarcoma cells after protease blockade¹⁴.

Cell streams and chains. Individual cells can form cell streams and chains (Fig. 1) so they move behind each other along tracks of remodeled ECM, and lack stringent cell-cell junctions but rather maintain repetitive tip-like loose interactions^{22,23}. This type of movement is known from neural crest cell^{23,24} and myoblast migration²⁵. These chains have been further observed in infiltrating lobular or metaplastic breast carcinoma^{26,27}, ovarian cancer²⁸, and melanoma of a vascular-type pattern^{22,29}. The arrangement of invading tumor cells in chains seems to represent a particularly effective penetration mechanism that confers high metastatic capacity and poor prognosis^{26,29}.

2.1.1.2 Collective cell migration in morphogenesis and regeneration

Collective migration differs from single cell migration since cells remain tightly connected during movement^{*}, which results in migrating cohorts and varying degrees of tissue organization³⁰⁻³². Collective migration of cohesive cell groups *in vivo* is particularly prevalent during morphogenesis, but also regeneration, and drives the formation of many complex tissues and organs. A similar collective behavior, known as invasion, is displayed by many invasive cancer types³.

Typically collective cell migration is characterized by³³: (1) physical and functional connections between cells during the migration process to preserve integrity of cell-cell junctions, including desmosomal junctions, tight junctions and, likely, gap junctions^{31,34,35}, (2) generation of traction and protusion force for migration and maintenance of cell-cell junctions by multicellular polarity and 'supracellular' organization of the actin cytoskeleton, and (3) modification of tissue along the migration path, either by clearing the track or by causing secondary ECM modification, including the deposition of a basement membrane (BM)^{33,36}.

Based on morphogenetic studies different types of collective invasion can be distinguished (Fig. 2)³.

Cell sheets. Cell sheet formation and migration as monolayer is known from keratinocyte movement during wound closure³⁷ (Fig. 2a). In epithelial and endothelial sheets cells are connected among each other via respective E- and VE-cadherin. Hereby actin-rich pseudo- and lamellipodia tentatively guide invasion and cells interact via integrins with ECM components like collagen, fibrin and BM molecules. In addition, growth factors secreted by stromal cells are involved in guidance (fibroblast growth factor (FGF), keratinocyte growth factor (KGF), transforming growth factor β (TGF β)).

* Cell streaming or single cell migration coordinated by chemokines, eventually defined as collective migration³² are here not included as these migration types rather base on single cell migration principles than on migration of many cells connected to a bigger, complex functional unit.

Collective invasion with lumen formation and tip cell. In vascular sprouting of newly forming or regenerating vessels (Fig. 2c) a tip cell with filopodial protrusions leads the migration of a multicellular stalk of endothelial cells, which are connected by VE-cadherin at cell–cell junctions and successively form an inner lumen³⁸. Tip and stalk cell fate are determined by differential response to extracellular gradients of vascular endothelial growth factor (VEGF) isoforms and the Notch-Delta axis³⁸. During migration BM components are deposited by both endothelial cells and pericytes and serve as a guidance track. Further, tracheal branching morphogenesis is characterized by formation of pseudo- and filopodia generating tip cells induced by FGF expression of surrounding cells³⁹. High levels of FGF signaling in tip cells additionally increase the expression of the Notch ligand Delta, which, in turn, silences actin dynamics in neighboring stalk cells by rendering them less responsive to the FGF signal⁴⁰.

Collective migration with lumen formation without tip cells. Branching morphogenesis of terminal end buds during breast development is characterized by a collective migration of epithelial cells in coordination with myoepithelial cells jacketing and stabilizing the bud shaft (Fig. 2b)⁴¹. Whereas myoepithelial cells are more loosely connected and migrate along the abluminal surface of ductal epithelial cells, the junctions between luminal cells are tight and baso-apical polarity is maintained during sprouting⁴¹. The extending bud tip forms a blunt-shaped multilayered bulb in which luminal epithelial cells remain laterally connected by E-cadherin but frequently exchange positions⁴¹. Because defined tip-cell and actin-based cell protrusions are lacking, terminal end bud protrusion could be the consequence of a pushing, rather than a pulling mechanism. After proteases released from stromal cells and probably also by the bud cells locally degrade the preexisting ECM⁴², secondary remodeling leads to deposition of a BM around the duct by both ductal and myoepithelial cells⁴². Mammary gland sprouting and branching are dependent on FGF receptor 2 (FGFR2)⁴³, similar to tracheal branching.

Collective migration of cell clusters. (a) The primordium of the zebrafish lateral line organ is a cohesive cohort composed over 100 cells that migrate along the flank of the embryo and become assembled into a series of connected epithelial rosette-like mechanosensory organs⁴⁴. Molecules that ensure coordinated cell movements are still elusive, but intravital imaging revealed that during migration not exclusively tip cells form filo- and pseudopods, but cytoplasmic processes are also found at cells migrating at the side of the primordium, indicating that many cells respond directly to extrinsic guidance cues⁴⁵. The directional persistence of the group is determined by the stromal cell-derived factor 1 (SDF-1/CXCL12) - CXCR4 signaling axis⁴⁶. Whereas all cells express CXCR4, only cells at the leading tip need to activate this receptor to direct the entire group⁴⁵. (b) Border cells form a tightly packed cluster of six to ten follicle cells surrounding two less motile polar cells during oogenesis in *D. melanogaster*, which migrate together along nurse cells in the egg chamber^{31,47} (Fig. 2e). Border cells

generate anterior Rac-dependent actin-rich protrusions in one or two leading cells⁴⁸, and are connected via E-adherin with surrounding nurse cells⁴⁹. The directional migration of the border cell cluster occurs along epidermal growth factor (EGF), PVF1 (platelet-derived growth factor- and VEGF-related factor 1) and PVF2 gradients⁵⁰.

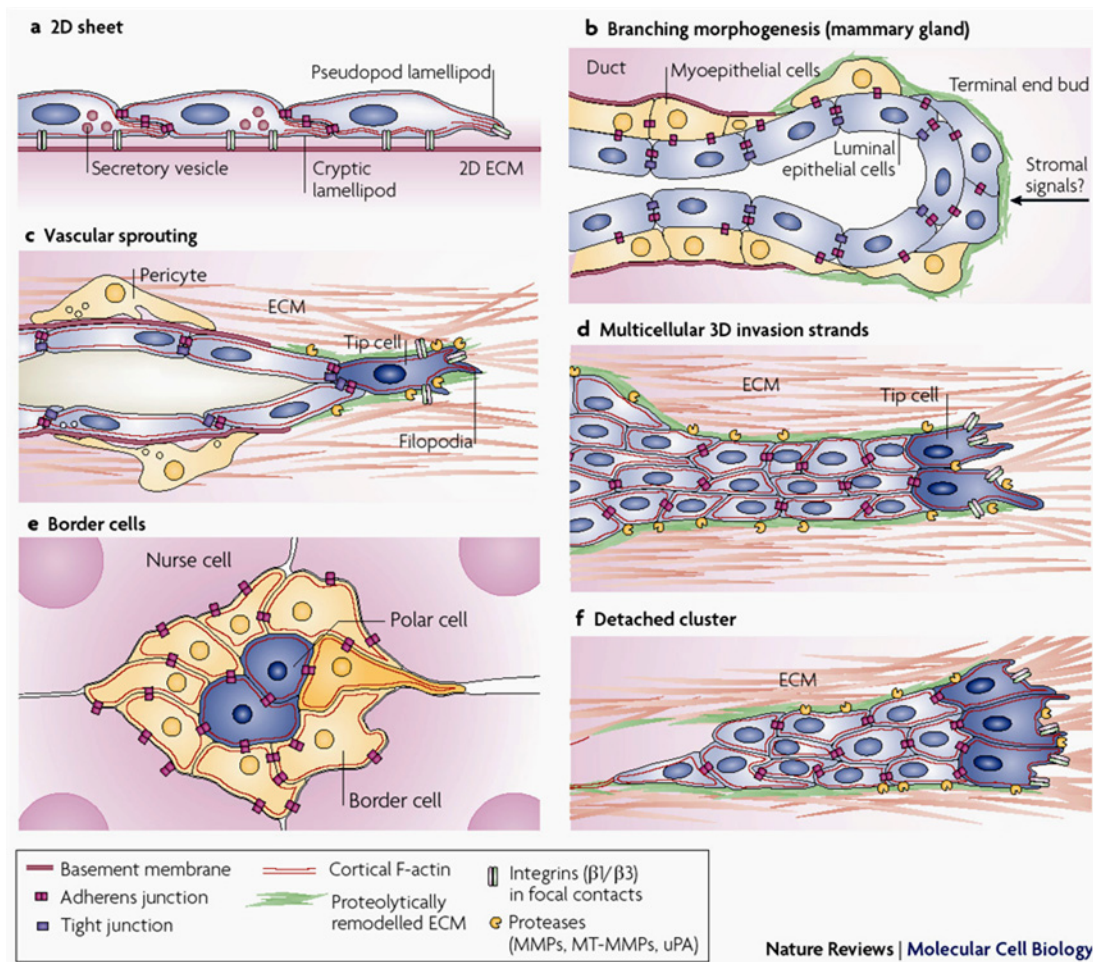


Figure 2. Types and variants of collective cell migration. Cell morphology and cell–cell and cell–extracellular matrix (ECM) adhesion in different forms of collective migration. Adapted from Friedl P & Gilmour D, 2009³.

2.1.1.3 Collective migration and invasion of cancer

As time-resolved studies of cancer invasion *in vivo* are difficult to proceed, less is known about the frequency and mechanisms of collective invasion of cancer and most observations are indirect. These few findings result from histopathological analyses, tissue explants, and two- (2D) and three-dimensional (3D) *in vitro* culture experiments, yet direct *in vivo* evidence is lacking. When explanted into a 3D environment, many cancers including rhabdomyosarcoma, oral squamous cell carcinoma, colorectal carcinoma and melanoma exhibit predominantly collective cell invasion and form migrating multicellular strands and clusters^{35,51-53} (Fig. 2d, f). Likewise, cell lines from

melanoma, colorectal carcinoma, breast cancer, fibrosarcoma and endometrial carcinoma move as 2D sheets or as 3D strands (Fig. 2d) in scratch wound⁵⁴⁻⁵⁶ or spheroid-invasion cultures¹⁴, respectively (O. Iliyina, K. Wolf, A. Khalil, P. Friedl personal communication and own unpublished observations). In fixed histopathological samples, most epithelial cancers display the hallmarks of collective invasion into surrounding tissues, including intact cell-cell junctions, expression of cadherins and/or expression of other homophilic cell-cell adhesion receptors in tumor regions deep inside the normal stroma^{35,57}. Likewise, in some invasive cancer types such as melanoma⁵⁸, breast⁵⁹, pancreas⁶⁰ or oral carcinoma⁶¹ cell-cell coupling and multicellular organization are likely retained, suggested by detected cell-cell adhesion and gap junctional proteins⁶². Moreover, *in vitro* studies investigating fibrosarcoma strand and colorectal sheet invasion highlight the importance of ECM remodeling by matrix metalloproteinases especially MT1-MMP^{14,63}. Comparison of types and mechanisms of collective cancer cell invasion discovered so far to morphogenetic or regenerative collective processes suggests that cancer cells are mimicking and reactivating embryonic pathways and patterns of cell movement³.

2.1.1.4 Plasticity of tumor cell migration

Although many cell types prefer a certain type of migration, cells can also adapt their migration mode to changed microenvironments and/or changed or impaired protein expression¹ (Figs. 1, 3).

One of the best described transitions from one to the other migration type is epithelial-to-mesenchymal transition (EMT). EMT is involved in many developmental processes and in invasive cancers like breast, colorectal or ovarian carcinoma^{4,34}, and includes downregulation of epithelial markers, mainly the loss of E-cadherin, and the upregulation of motility and invasiveness increasing molecules like proteases^{4,34}. Currently, also the reverse transition MET (mesenchymal-to-epithelial) is discussed in the process of metastasis seeding of breast cancer⁶⁴ or during progression of mesenchymal tumors e.g. synovial carcinomas⁶⁵. *In vitro* a collective-to-amoeboid transition can be observed when integrin or protease blockade induce disintegration of collective strands or clusters resulting in individual, amoeboid migrating cells^{14,52}. Conversely, if individually moving cells up-regulate cell-cell adhesion molecules, then cell aggregation leads to individual-to-collective transition⁴. Mesenchymal-to-amoeboid transition is mainly caused by an inhibition or downregulation of Rac and a stimulation or upregulation of Rho/ROCK signaling⁶⁶ and can be further provoked by blockade of pericellular proteolysis⁷.

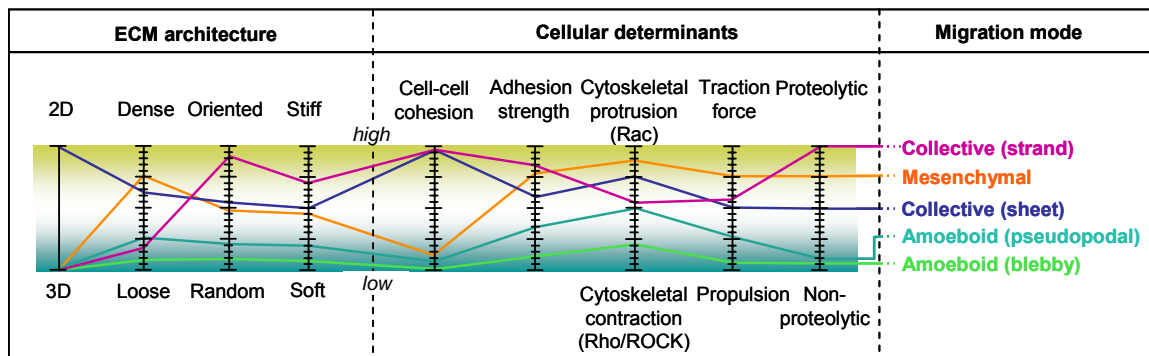


Figure 3. The tuning model of cell migration. An integrated multiscale model to combine multiple interdependent parameters that impact migration mode. Each parameter is experimentally testable individually; however, in most cases they are interconnected with others. Approximated parameter profiles of selected migration modes are indicated (coloured lines). Modulation by increasing or decreasing the magnitude of any parameter may impact the resulting migration mode as well as the input strength of co-regulated parameters. Adapted from Friedl P & Wolf K, 2010¹.

Various factors regarding the cell itself or its environment influence the migration pattern¹ (Fig. 3). Cell intrinsic factors influenced by protein expression are (1) strength of cell-cell contacts, (2) expression of adhesion molecules, (3) cytoskeletal contractility, (4) generated traction force, and (5) proteolytic capacity¹. Environmental factors include (1) matrix density, whereby migration is fastest if ECM gaps match cell size^{11,67}; (2) stiffness or matrix rigidity – cells tend to migrate towards the substrate of greater stiffness, termed durotaxis⁶⁸; and (3) orientation of ECM molecules - alignment of ECM molecules favors multicellular streaming in chainlike patterns in 3D tissue¹.

2.1.2 Molecules involved in migration and invasion

2.1.2.1 Cell adhesion molecules

The integrin superfamily and its members are the most important receptors for adhesion to the ECM and affect thereby all migration modes. Besides ECM substrates also cell surface and soluble ligands can be bound⁶⁹ (Table 1). Integrins form $\alpha\beta$ heterodimers integrated into the cell membrane whereby both chains are required for ligand-binding and cytoplasmic coupling to the actin cytoskeleton. To date 18 α and 8 β subunits are known in humans that form 24 heterodimers.

The major receptors for fibrillar collagen are $\alpha2\beta1$, for laminin $\alpha3\beta1$ and $\alpha6\beta1$, for fibronectin $\alphaV\beta3$ and $\alphaV\beta5$ (Table 1). Integrin signaling is bidirectional; intracellular signals influence integrin binding activity to the ECM (inside-out-signaling) and integrin binding to ECM molecules transmit signals into the cell (outside-in-signaling)⁷⁰. The binding is reversible and calcium dependent, and results in coupling to the actin cytoskeleton and further signaling molecules (PI3K/Akt, JNK/Jun, or Ras/Raf/MEK/Erk) via adaptor proteins, including talin, paxillin, α -actinin or focal adhesion kinase (FAK)⁷¹. The accumulation and clustering of integrins, cytoskeletal and signaling proteins is called

focal adhesion or contact². After the initial formation of focal adhesions, ECM contacts and adhesion can be stabilized and strengthened by stress fibers consisting of polymerized actin (F-actin). If the cell is in a migrating state, dynamic extensions like filopodia and lamellipodia are formed at the leading edge. The polymerization and contraction of F-actin networks is controlled by small GTPases of the Rho-family. Whereas Rho supports increasing adhesion by induction of focal adhesion and stress fiber formation⁷², Cdc42 and Rac induce filo- and lamellipodia formation, respectively, which favor cell migration^{73,74}. The same events occur cyclically during cell migration as cells extend lamellipodia and form focal adhesions to derive the traction necessary for movement. Integrins are of major importance in the adhesion process on 2D substrata, but 3D culture and *in vivo* studies have delivered controversial results. Studies showed that e.g. $\alpha 2\beta 1$ and $\alpha V\beta 3$ integrin can support invasion in melanoma⁷⁵ or ovarian cancer⁷⁶, respectively, however, also impede invasion in breast carcinoma cells⁷⁷ or melanoma⁷⁸, respectively.

Table 1. Ligand-binding specificities of human integrins. Adapted from Takada Y et al. 2007⁶⁹.

Integrins	Ligands
$\alpha 1\beta 1$	Laminin, collagen
$\alpha 2\beta 1$	Laminin, collagen, thrombospondin, tenascin
$\alpha 3\beta 1$	Laminin, thrombospondin, uPAR
$\alpha 4\beta 1$	Thrombospondin, MAdCAM-1, VCAM-1, fibronectin, osteopontin, ADAM, ICAM-4
$\alpha 5\beta 1$	Fibronectin, osteopontin, fibrillin, thrombospondin, ADAM, COMP, L1
$\alpha 6\beta 1$	Laminin, thrombospondin, ADAM, Cyr61
$\alpha 7\beta 1$	Laminin
$\alpha 8\beta 1$	Tenascin, fibronectin, osteopontin, vitronectin, nephronectin
$\alpha 9\beta 1$	Tenascin, VCAM-1, osteopontin, uPAR, plasmin, angiostatin, ADAM, VEGF-C, VEGF-D
$\alpha 10\beta 1$	Laminin, collagen
$\alpha 11\beta 1$	Collagen
$\alpha V\beta 1$	Fibronectin, osteopontin, L1
$\alpha L\beta 2$	ICAM, ICAM-4
$\alpha M\beta 2$	ICAM, iC3b, factor X, fibrinogen, ICAM-4, heparin
$\alpha X\beta 2$	ICAM, iC3b, fibrinogen, ICAM-4, heparin, collagen
$\alpha D\beta 2$	ICAM, VCAM-1, fibrinogen, fibronectin, vitronectin, Cyr61, plasminogen
$\alpha IIb\beta 3$	Fibrinogen, thrombospondin, , fibronectin, vitronectin, vWF, Cyr61, ICAM-4, L1, CD40 ligand
$\alpha V\beta 3$	Fibrinogen, vitronectin, vWF, thrombospondin, fibrillin, tenascin, PECAM-1, fibronectin, osteopontin, BSP, MFG-E8, ADAM-15, COMP, Cyr61, ICAM-4, MMP, FGF-2, uPA, uPAR, L1, angiostatin, plasmin, cardiotoxin, Del-1
$\alpha 6\beta 4$	Laminin
$\alpha V\beta 5$	Osteopontin, BSP, vitronectin, CCN3
$\alpha V\beta 6$	Fibronectin, osteopontin, ADAM
$\alpha 4\beta 7$	MAdCAM-1, VCAM-1, fibronectin, osteopontin
$\alpha E\beta 7$	E-cadherin

Not otherwise used abbreviations: ADAM, a disintegrin and metalloprotease; BSP, bone sialic protein; CCN3, an extracellular matrix protein; COMP, cartilage oligomeric matrix protein; Cyr61, cysteine-rich protein 61; L1, CD171; iC3b, inactivated complement component 3; PECAM-1, platelet and endothelial cell adhesion molecule 1; uPA, urokinase; uPAR, urokinase receptor; VEGF, vascular endothelial growth factor; vWF, von Willebrand Factor.

In addition to their well-established role in migration and invasion, integrins also regulate proliferation and survival⁷¹. Integrin binding to receptors controls the expression of key cell cycle proteins, including cyclin D1⁷⁹ and the cyclin-dependent kinase inhibitor family, which regulate entry into the S-phase of the cell cycle⁸⁰. Moreover, ligated integrins prevent pro-apoptotic signaling cascades initiated by integrin-mediated death/anoikis (cell death induced by inadequate or inappropriate cell-matrix interactions)⁸¹, and increase survival signaling by upregulation of anti-apoptotic proteins and p53 inactivation, as well as activation of the PI3K/Akt pathway and NF- κ B signaling^{71,82}.

Other, non-integrin adhesion molecules are CD44, mediating binding to hyaluronic acids and, at lower affinity, to chondroitin sulfate, heparan sulfate, fibronectin, and osteopontin⁸, discoidin domain receptors (DDR1 and 2) binding to collagen⁸³, and surface proteoglycans forming complexes with other proteoglycans, hyaluronans and fibrous matrix proteins such as collagen of the ECM.

2.1.2.2 Matrix degradation

The engagement of integrins and other adhesion receptors leads to the recruitment of surface proteases towards attachment sites, which, in turn, degrade ECM components that are in close proximity to the cell surface. Besides serine, cysteine and aspartic proteases, the family of matrix metalloproteinases (MMPs) strongly contributes to cell migration in general. MMPs are either secreted as soluble proteases or transmembrane proteases which together degrade diverse substrates including virtually all structural extracellular matrix proteins⁸⁴. Proteases can directly bind to integrins e.g. membrane-type MMP-1 (MT1-MMP), an important collagenase, and MMP2 co-localize with β 1 or β 3 integrins as they adhere to collagen fibers^{7,85,86}. ECM degradation occurs while the advancing cell body gains volume towards the ECM scaffold and is likely to provide the space required for cell expansion and migration, leaving behind tube-like matrix defects along the migration track that can be used by following single cells or associated cell collectives^{14,22,87}.

The requirement for proteases during cancer progression is controversially discussed. The upregulation of MMPs, uPA and cathepsins is a uniform process in many different cancer cell types, and has been positively correlated with tumor progression and metastasis^{88,89}. So far, studies of protease influence are mainly performed on *in vitro* migration processes^{14,90} or the metastatic potential after orthotopic implantation^{91,92}. In this context it could be shown that interference with MMPs can affect the invasive potential of tumor cells dramatically. Dependent on the density of the ECM inhibition of MT1-MMP results in mesenchymal-to-amoeboid transition^{7,93} or complete migration arrest⁹⁴. *In vivo*, the direct influence of proteases invasion is elusive, but for instance the metastatic efficiency

is not diminished by protease inhibitors in breast⁹⁵, oesophageal and ovarian carcinoma models⁹⁶. Clinical trials on MMP inhibitors in late-stage cancer patients have yielded an inconsistent outcome — in some cases, significant progression occurs despite treatment, so that the clinical relevance of matrix proteases in cancer metastasis awaits direct proof⁹⁷.

2.1.2.3 Pro-migratory signaling

Besides the intrinsic ability of a cell to migrate, the microenvironment plays a fundamental role in cell migration. Cell invasion can be initialized and guided by signals provided by stromal cells and mechanisms known from morphogenetic and regenerative processes are often also relevant in cancer cell migration. In Table 2 soluble factors provided by the microenvironment are listed that guide morphogenetic and cancer cell invasion.

Table 2. Soluble factors that induce migration/are involved in metastatic dissemination secreted by stromal cells.

<i>Soluble factor</i>	<i>Morphogenetic/regenerative migration processes</i>	<i>Cancer cells</i>	<i>Secreted by</i>
EGF	Border cell migration ⁵⁰	Breast CA ^{98,99}	Tumor-associated macrophages (TAM)
FGF	Wound healing ³⁷ /Tracheal branching ¹⁰⁰	Pancreas CA ¹⁰¹	Stromal cells
TGFβ	Wound healing ³⁷	Breast CA ¹⁰²	Stromal cells
HGF	Migration of muscle progenitor cells during generation of skeletal muscle ¹⁰³	Gallbladder ¹⁰⁴ , non-small and small cell lung ¹⁰⁵ , cervical ¹⁰⁶ , and oral squamous cell CA ¹⁰⁷ , breast cancer ¹⁰²	Stromal cells
SDF-1	Primordium migration ⁴⁵	Breast CA ¹⁰⁸	Myoepithelial cells, myofibroblasts

Downstream signaling of growth factors includes besides various effects on cell proliferation and survival also migration-associated signals. Binding of EGF to EGFR results mainly in signaling via the MAPK and PI3K/Akt pathway triggering pro-proliferative and anti-apoptotic signals, but also has multiple effects increasing cell motility mediated by PI3K/FAK and the small GTPases Rac, Rho and Cdc42¹⁰⁹. Moreover, as consequence of binding, MMPs are upregulated via Ras signaling, and cell-cell adhesion molecules like E-cadherin are downregulated¹⁰⁹. Similarly, FGF and TGFβ increase invasiveness^{101,102}. FGF is shown to induce EMT in breast and pancreatic tumor cells via its receptor FGFR1 and associated MAPK signaling¹¹⁰. Although TGFβ is known to induce growth arrest and apoptosis it can also result in EMT-promoting gene transcription via Ras and Smad signaling and activation of Cdc42 and Rho^{111,112}. In addition, integrin and growth factor signaling is tightly connected^{109,113}. On the one hand, integrin-binding to ECM molecules can induce transactivation of growth factor receptors without ligand

binding^{109,113}. On the other hand, FGF binding might cause upregulation of $\alpha 5\beta 1$, TGF β binding upregulation of $\beta 1$ and $\beta 5$ and further *de novo* synthesis of $\alpha V\beta 6$ ¹¹³. Although best characterized for its role in the recruitment of haematopoietic cells to sites of injury or infection, the chemokine SDF-1 can be also secreted by stromal cells of the tumor microenvironment; e.g. myoepithelial cells and myofibroblasts close to invasive breast tumors, but not those associated with ductal carcinoma *in situ* or normal breast tissue, secrete SDF-1¹⁰⁸. CXCR4 (the respective receptor) signaling leads to the activation of multiple small G protein pathways includes PI3K/Cdc42/Rac and Raf/MAPK resulting in increased mobility of cells¹¹⁴ including upregulation of integrins such as $\alpha 5\beta 1$ and $\alpha v\beta 3$ ^{115,116}. Reciprocally, integrin binding can regulate CXCR4 expression¹¹⁷.

In addition to pro-migratory molecules provided by the microenvironment, many factors are also produced by the tumor cells themselves, released into the surrounding and act than autocrine such as autocrine motility factor (AMF) thereby stimulating migration¹¹⁸⁻¹²². Further molecules acting as promigratory factors are lysophosphatidic acid, insulin-like growth factor-1, and enzymes degrading ECM components thereby leading to the engagement of integrins².

Taken together, although many soluble factors are known to be involved in cancer cell invasion, the specific role of each factor in tumor cell invasion still needs to be dissected.

2.1.2.4 Cell-cell adhesion molecules

If cells migrate as multicellular groups, an intercellular connection is a prerequisite to retain cell-cell cohesion, mechanical integrity, and cell polarity³³. Known junctions are: (a) *adherens junctions* defined as a cell junction whose cytoplasmic face is linked to the actin cytoskeleton consisting mainly of cadherins, α and β catenin, and transmembrane proteins of the immunoglobulin superfamily like ALCAM or L1CAM³³, (b) *desmosomes* are characterized by a wide intercellular space and attach the cell surface adhesion proteins to intracellular keratin cytoskeletal filaments, (c) *tight junctions* and involved proteins like claudins, occludin and ZO-1 form a virtually impermeable barrier to fluid, and (d) *gap junctions* mainly consist of connexins and directly connect the cytoplasm of two cells, which allows various molecules and ions to pass freely between cells.

The role of specific junctions in collective invasion of cancer cells still needs to be elucidated, but it is already known that the composition of adherens junctions is of main importance: e.g. a slight downregulation of one junctional protein (E-cadherin) and the upregulation of another (N-cadherin) can thereby be sufficient to initiate collective invasion in carcinoma cells¹²³. In contrast to E-cadherin, adhesion forces mediated by N-cadherin are 4- to 7-fold weaker¹²⁴. Similarly the composition of desmosoms might be important for collective invasion. In general, desmosomal proteins are markers of epithelial differentiation, and loss of their expression results in the EMT during

morphogenesis and cancer progression^{125,126}, but for instance a upregulation of desmocollin 1 and 3 can be used as indicator for collective invasion of colorectal adenocarcinoma¹²⁷. Moreover, tight junctions and related proteins are detectable in invasion zones of squamous cell carcinomas and melanomas^{128,129} and can colocalize with N-cadherin¹²⁹. In many cancer cells, including melanoma and lung squamous cell carcinomas, the homotypic gap junction between cancer cells themselves and the heterotypic gap junctions between cancer cells and dermal fibroblasts are mediated by connexins CX26 and CX43, respectively¹³⁰, yet their direct contribution remains to be shown. Besides, also integrins are discussed in context of cell-cell contacts in tumors³³. Blocking of $\beta 1$ integrin can result in disintegration of migrating melanoma cell collectives⁵² and $\alpha 5\beta 1$ integrin was shown to interact with fibronectin along interfaces between ovarian carcinoma cells¹³¹ or fibroblasts¹³². Remarkably, tumor cells can also upregulate leukocyte-specific integrins (LFA-1/ $\alpha L\beta 2$)¹³³ that are able to bind to ICAM molecules expressed e.g. by endothelial cells.

2.2 Models of cancer cell invasion

2.2.1 Experimental models to investigate migration and invasion

To study invasion and migration of cancer cells various *in vitro* and *in vivo* models can be used.

2.2.1.1 *In vitro* models

In comparison to *in vivo* models, *in vitro* models are easy to handle, relatively simple in their application and cheap. They are tightly controllable concerning composition of ECM molecules, participation of cells and interfering molecules, and further multiple ways exist to fast and multifaceted analyze experimental outcome including diverse microscopy techniques as well as protein expression studies by FACS or immunoblotting.

2D migration. 2D migration of adherent, individual or as sheets connected cells can be studied on plastic cell culture dishes or glass and easily combined to microscopy techniques (time-lapse videomicroscopy, confocal microscopy etc.). To investigate the role of ECM components, such as collagen, fibrin, BM components (Matrigel) or fibronectin coating of plastic dishes or glass can be performed prior to seeding of cells. Cell-cell interaction can be further studied by seeding cells of interest onto an adherent layer of a second cell type. Sheet migration can be tested by the wound closure/scratch assay, which was recently translated to high-content imaging¹³⁴. As cells are not embedded in thick matrices subsequent cellular immunostaining of molecules of interest and their analysis are easy to perform.

Boyden chamber transwell migration. A popular method to study motility of cells is the transwell migration assay consisting of an upper and a lower compartment separated by a porous polycarbonate membrane with defined pore sizes that cells need to pass through to migrate from the upper to lower filter surface¹³⁵. This model is popular for studying chemotaxis effects by adding chemoattractants to or by seeding cells in the lower compartment. Migration through ECM or BM can be tested by coating of the filter membrane with respective components¹³⁶. Inversely, migration of cells attached to the lower filter surface through the filter and ECM layers can be tested¹³⁷. Moreover the assay can be easily combined with confocal microscopy and ultrastructural analysis¹³⁸.

3D migration. During the past 20 years differences between 2D and 3D cell movement have been taken into account resulting in a wealth of 3D models of cell migration aiming at improvement of *in vivo* relevance^{15,139,140}.

(A) Popular is the use of fibrillar *collagen lattices* composed of pepsinized or non-pepsinized collagen molecules, substituted or not with additional ECM components like vitronectin, matrigel, fibronectin and others⁹³. Here within either individual cells (also suspension cell-culture cells such as leukocytes), cell spheroids, or tissue explants can be embedded or seeded on top. Importantly, migration modes depend on the type of implantation; imbedded individually, cells perform single-cell migration^{7,8}, whereas spheroids or tissue explants bear in addition collective invasion types^{14,52}. To reflect *in vivo* complexity in humans, layers of different density or composition can be combined; e.g. organotypic skin models consist mostly of different layers of collagen partially mixed with cellular components like fibroblasts and/or keratinocytes¹⁴¹⁻¹⁴³.

(B) Fresh human dermis (left-over from skin surgeries) and sectioned, cryopreserved skin¹⁴⁴ serve as more complex substrates for 2D and 3D migration studies. Likewise, off-the shelf scaffolds comprise cadaveric human or porcine acellular dermal matrices which have been developed for skin grafting on acute and chronic wounds¹⁴⁵ can be used further to study interaction of cells with ECM.

In vitro migration and invasion can be assessed by time-lapse bright-field or fluorescence microscopy techniques¹⁴⁶. Computer-assisted cell tracking and analysis allows thereby quantification of migration parameters such as distances, velocities, but also other cellular parameters like cell shape^{146,147}. The use of confocal or multiphoton microscopy facilitates not only detailed observation of tumor cells, but also enables display of e.g. collagen fibers by reflection and second harmonic generation microscopy, respectively⁹³.

Consequently, the choice of an *in vitro* model is strongly dependent on the cell type, the migration mode of interest, the manipulations and interferences that should be tested, and finally the strived convergency to the *in vivo* situation.

2.2.1.2 Interstitial *in vivo* models

To fully reflect *in vivo* complexity which depends upon the interaction between cancer cells and the reactive tumor stroma, *in vivo* monitoring of tissue invasion is required. Besides releasing invasion promoting factors such as growth factors and chemokines (see paragraph 2.1.2.3), the tumor stroma provides complex interfaces and anatomic structures including various cell types and ECM components arranged in different composition and density. Further, the tumor stroma contains blood and lymph vessels which ultimately serve for distant metastatic dissemination and determine the perfusion state of the lesion. All these factors massively determine if and how efficient cancer cells invade the surrounding environment¹⁴⁸⁻¹⁵⁰.

Orthotopic *in vivo* models of cancer combined with histopathology allow reconstruction of the outcome of cancer growth and invasion^{151,152}, but for direct examination of microvascular structures, cell dynamics, tumor-stroma interactions or early steps of tumor metastasis, models are necessary that provide additionally access to microscopy techniques⁹³.

Connective tissue models. The connective tissues from different locations (i.e. mesenterium, cremaster muscle, skull dermis of the frontoparietal scalp, back dermis, mammary fat pad) contain fibrillar collagen networks of very heterogeneous architecture; structurally loose areas with gaps and clefts of various sizes (up to 20 μm) are bordered by denser regions of thick collagen bundles partially aligned in parallel in the absence of obvious gaps and spaces⁹³. The mesenterium displays a well-vascularized, thin connective tissue membrane with high collagen density which has been used preferably from rats or rabbits¹⁵³. It is amenable to study microvessel dynamics and leukocyte extravasation¹⁵³. The highly vascularized cremaster muscle holding and regulating the vicinity of the testes towards the abdomen is also suitable and accessible for imaging of leukocyte migration¹⁵⁴. The muscle is laterally bordered by thick, loose collagen layers, where fibers are mainly organized in parallel⁷. Skin of the frontoparietal mouse scalp consists of several collagen-rich connective tissue layers in the dermis underneath an epidermis with heterogeneous structure and density which can be used for the injection of fluorescently labeled cells to study invasion pattern and parameters of tumor cells⁷. Similarly, migration behavior of tumor cells after injection or prior tumor implantation into lateral and dorsal skin of the mouse can be observed in the skin flap model^{155,156}. To date, these models have been used to study only single cell migration^{7,153,154}. The great advantages of these models are the relatively easy accessibility also by bright-field microscopy techniques^{153,154} and the simple tissue preparation. However, they have in common that they require fresh tissue preparation on the anesthetized animal and thereby prohibit long-term studies and repeated imaging of a specific site of interest, last but not least also due to scar generation and possible infections.

Window models. Window models allow repetitive optical and often high-resolution observations of cell and tissue dynamics, including microcirculatory function, angiogenesis, tumor cell-host interactions and invasion, and evaluation of effects of various treatments on these factors¹⁵⁷.

Table 3. Established window models for cancer studies.

<i>Window model</i>	<i>Tissue</i>	<i>Tumor studies</i>		
		<i>Microcirculatory function</i>	<i>Angiogenesis</i>	<i>Tumor-host cell interaction</i>
Cranial window	Brain	Mostany et al ¹⁵⁸	Goldbrunner et al ¹⁵⁹	
	Brain – experimentally metastasized lung CA and melanoma cells			Kienast et al ¹⁶⁰
Mammary window	Mamma	/	Shan et al ¹⁶¹	Kedrin et al ¹⁶²
Dorsal skinfold chamber	Subcutis of dorsal skin	Asaichi et al ¹⁶³ , Boucher et al ¹⁶⁴ , Leunig et al ¹⁶⁵ , Reyes- Aldasoro et al ¹⁶⁶	Boucher et al ¹⁶⁴ , Guba et al ¹⁶⁷ , Leunig et al ¹⁶⁵	Vajkoczy et al ¹⁶⁸ (not orthotopic)

Established models for cancer studies (Table 3) are developed for skin tissue of the mouse, hamster or rat back (dorsal skinfold chamber)¹⁵⁷, mammary tissue (mammary window)¹⁶² and brain tissue of the mouse (cranial window)¹⁵⁹. Further window models, not used for cancer research so far, are the femur chamber¹⁶⁹ and the 'body window' to the kidney capsule¹⁷⁰. The dorsal skinfold chamber (DSFC) is the most widely used *in vivo* model in preclinical cancer research for drug testing, angiogenesis and tumor progression studies, as well as vascular leakage and intratumoral pressure measurements of various cancer types including melanoma and fibrosarcoma^{157,163-167}. As technical variants, cells are implanted between the dermal fascia and the cover slip of the chamber, either as tumor cell suspensions^{164,165}, pellets¹⁶⁷, and spheroids¹⁷¹, or solid tumor explants¹⁶³, with or without a carrier such as matrigel¹⁷². As the prepared tissue is covered by a cover slip a closed system is formed which is less susceptible to infections. During the experimental period the tumor and surrounding tumor stroma are easily accessible and can be constantly observed using diverse microscopy techniques including bright-field and epifluorescence microscopy¹⁵⁷. To visualize cellular and stromal details high-resolution is necessary. Recently multiphoton microscopy became the method of choice for intravital deep tissue imaging¹⁷³⁻¹⁷⁵ (see paragraph 2.3), but although this technique is available and imaging access to the interface between tumor and stroma is guaranteed by the DSFC, studies of tumor invasion of orthotopically implanted cancer cells are still absent. Extension of the skin also due to gravity and fluid coalescence in the visual field limit the DSFC model and observation of tumor progression to a two weeks time window.

Chick embryo CAM model. The chorioallantoic membrane (CAM) of the chick embryo is a traditional model for monitoring tumor growth and dissemination, related angiogenesis, and metastasis^{93,176}. The CAM displays a specialized, highly vascularized tissue that mediates gas exchange between the developing chick embryo and the atmosphere through the calcified eggshell. The fully developed CAM (day 10 of embryonic development) consists of ectoderm, mesoderm, and endoderm, whereby the approximately 100 μm thick mesoderm comprises a loose collagen-rich connective tissue containing blood vessels and capillaries¹⁷⁶. The collagen meshwork is, in contrast to mouse connective tissue, of quite homogeneous order with gap diameters ranging from 4 to 10 μm ⁹³. Invasion is generally monitored from the ectodermal layer across a basal membrane into very loose connective tissue and, within few days, metastasis seeding into the chick embryo is detectable.

Zebrafish and medaka model. Also *D. rerio* (zebrafish) and *O. latipes* (medaka) can be used as model to investigate tumor cell invasion and metastatic processes¹⁷⁷⁻¹⁷⁹. Human cancer cells or small tumor explants e.g. from gastrointestinal tumors can be fluorescently labelled and xenotransplanted orthotopically into zebrafish embryos thereby allowing rapid analysis of invasion and metastasis formation combined with easy imaging access¹⁷⁸. Further, early steps of metastasis like intravasation and influence of metastasis promoting factors can be studied in adult translucent zebrafish¹⁷⁹.

In summary, diverse *in vivo* models are available that allow imaging of tumor cell migration processes in different animals. In contrast to invasive connective tissue models where imaging is restricted to a single time point, translucent and non/once-invasive models like the CAM or xenografting in fish allow time-course specific observation of tumor progression. Nevertheless, the latter cases are in disadvantage regarding the evolutionary distance to humans. Window models in mammals represent a good compromise to reach comparability to the human system and to study tumor progression in long-term and repetitively.

2.2.2 Biological models

Despite the chosen *in vitro* or *in vivo* tumor migration model, self-evidently the cancer cell type is of main importance determining whether a cell is able to migrate or not; and if able, which migration modes it is using (see paragraphs 2.1.1 and 2.2.1). Although invasiveness is considered to be linked to the metastatic potential of a tumor, the direct connection between invasion and metastasis is not fully established. Some locally highly invasive cancer types like basal cell carcinoma¹⁸⁰ or glioma¹⁸¹ form very rarely distant metastasis. Moreover, invasion is often defined differentially between cancer types. Whereas in epithelial cancer invasion is defined by cells breaking through the BM, in

sarcomas invasion more generically is linked to cell spread into the surrounding, non-neoplastic tissue. To adapt to a mesenchymal way of movement and acquire the capability to invade, naturally resident epithelial cells like breast cancer cells have to undergo EMT⁴ (see also paragraph 2.1.1.4) and/or need the assistance of stromal cells¹⁴⁹. In contrast, many highly invasive cancer cell lines constitutively generate mesenchymal migration *in vitro* such as fibrosarcoma or melanoma cells (see also paragraph 2.1.1.1), thereby providing direct inside into the mechanisms required for migration.

2.2.2.1 Fibrosarcoma

Fibrosarcoma belong to the heterogeneous malignant group of soft tissue sarcomas (STS) arising from fibrous tissues (tendons and ligaments), i.e. mesenchymal stem cells¹⁸². STS have an incidence of 1 – 2% of all malignancies in adults and 5 – 8% of paediatric solid tumors¹⁸². They are highly invasive, often form locally secondary tumors, and have also after treatment a high rate of local recurrence¹⁸². Approximately 50% of all patients develop metastatic disease, most frequently to the lung, and if untreated, the median survival-time is < 12 months¹⁸².

Little is known about the mechanisms underlying fibrosarcoma invasion *in vivo*. A few histopathological analyses of fibrosarcoma or invasive dermatofibrosarcoma protuberans material from patients or animal models show a multicellular invasion pattern as well as diffuse infiltration into the surrounding^{14,183,184}, and since dynamic intravital studies are absent, invasion efficiency is measured from the outcome of distant metastasis¹⁸⁵. *In vitro* fibrosarcoma cell migration and invasion was shown to be diverse. Experimentally dispersed human HT-1080 fibrosarcoma move as single cells mainly mesenchymally and generate proteolytic migration tracks^{14,186}. After blockade of matrix proteases HT-1080 cells can switch to an amoeboid type of movement comparable to leukocytes characterized by shape change and formation of constriction rings⁷ (Fig. 1). In these cells, the blockade of integrins ($\beta 1$ and αV) results in a residual minimal blebby amoeboid movement (Fig. 1). If implanted as multicellular spheroids into a 3D fibrillar collagen matrix, migration of HT-1080 cells, similar to other cancer cell types, may occur as collective strands within proteolytic migration tracks of least physical resistance generated by MT1-MMP dependent collagenolysis¹⁴. After interference with pericellular proteolysis or knockdown of MT1-MMP transition from collective to amoeboid migration occurs in these cells¹⁴. Thus, fibrosarcoma cells appear to utilize diverse migration modes *in vitro* and dispose substantial plasticity. Besides the involvement of integrins and proteinases, further *in vitro* studies highlight the importance of NF- κB ¹⁸⁵ and Met signaling¹⁸⁷ for fibrosarcoma migration.

However, despite this abundant literature about *in vitro* invasion patterns and participating mechanisms, little is known about their relevance for fibrosarcoma invasion into host tissue *in vivo*.

2.2.2.2 Melanoma

Malignant melanoma is the most aggressive form of skin cancer arising *de novo* from normal melanocytes or from potential precursor lesions, such as atypical dysplastic or congenital nevi¹⁸⁸. Melanomas are generally highly invasive and metastatic. Relapse rates range between 20 and 80% dependent on the staging of the primary tumor¹⁸⁹. Historically, the most important prognostic factors in patients without metastases are the tumor thickness¹⁹⁰ and, to a lesser extent, the level of invasion¹⁹¹. With early detection and treatment, the cure rate for melanoma is about 95%; 5-year survival with distant metastasis 16%. 70% of diagnosed cases belong to the superficial spreading melanoma which are characterized by an prolonged radial growth phase, where the lesion remains thin, eventually followed by a vertical growth phase where the tumor increases in thickness¹⁹². In contrast, the nodular melanoma (about 15% of diagnosed cases), the most aggressive form, has no detectable radial growth phase, but grows in vertical direction from the outset and very fast (months)^{192,193}.

Since melanoma cells are of neuroectodermal origin (derived from neural crest cells), mechanisms were found to be important comparable to neural crest cells, including single cell migration in spindle-shaped, mesenchymal mode and, often, multicellular streaming *in vitro*⁸. In addition, using explant culture, collective cluster migration was reported⁵², and further, derived from histopathological sections, in patients strand-like multicellular invasion into deep dermal layers (vertical growth) could be detected¹⁹². Taken together, similar to fibrosarcoma, melanoma cells dispose a spectrum of invasion modes, yet dynamic microscopical studies investigating the early steps of melanoma invasion and underlying principles in an intravital model are missing.

Integrins are of major importance for the invasiveness of melanoma cells in collagen based migration models. *In vitro* studies reveal a $\alpha 2\beta 1$ integrin-dependency of migration; interference with $\beta 1$ integrin thereby results in migration abrogation in single cells⁸, or loss of cluster polarity, disruption and collective-to-amoeboid transition⁵². Furthermore, application of an αV integrin blocking antibody decreased cell adhesion to fibronectin, migration and invasion in a transwell assay *in vitro*¹⁹⁴. As indicated in paragraph 2.1.2 integrin expression and adhesion to the ECM is influenced by a variety of other molecules. For instance, also ephrinB2, part of a cell-cell signaling system that directs cellular migration during development^{195,196}, is expressed in the invasive front of malignant melanoma and was shown to increase integrin-mediated ECM adhesion and motility in transwell and scratch assays *in vitro*¹⁹⁷. Comparable to other tumor models,

also proteases support melanoma cell invasion^{185,188}; they are upregulated in the invasive front of malignant melanoma, increase the invasiveness *in vitro* and the metastatic potential *in vivo*¹⁸⁸. Similarly, chemokines play an important role in mediating melanoma cell invasion. For instance it has been shown that CCL21 secreted by lymph endothelial cells in a constitutive manner can attract melanoma cells towards lymphatic vessels¹⁹⁸. Moreover, melanoma cells are able to induce chemokine production (IL-1B, IL-8, IL-6 and CCL2/MCP1) in tumor-associated stromal cells generating thereby a pro-invasive microenvironment for themselves¹⁹⁹.

Similar to studies investigating fibrosarcoma invasion many molecules are known which influence the migratory behavior *in vitro*, but the *in vivo* correlation is mostly measured as metastatic outcome without clear link to invasion programs.

2.3 Microscopical techniques to study invasion *in vivo*

To directly visualize cancer invasion in deep tissues in a living animal fluorescence microscopy is the method of choice. Thereby the use of fluorescent molecules and proteins to stain tumor cells allows separation of invading cells from the surrounding host tissue. For overview imaging and for purposes that require low resolution epifluorescence microscopy is suitable¹⁵⁷, but to resolve topographic complexity at cellular level and provide a time-resolved read-out from the same sample, non-invasive intravital confocal or multiphoton imaging of cancer lesions provides kinetic resolution by serial reconstruction over an extended observation period¹⁷³.

Multiphoton microscopy (MPM) has emerged as a significant detection and visualization method for intravital and live cell studies in neuroscience, immunology, and cancer research. The main advantage of MPM over other imaging approaches is its ability to observe cell migration, cell-cell interaction, and intracellular signaling deeply inside dense tissues and organs in live animals with unmatched resolution and photodamage¹⁷³⁻¹⁷⁵. Compared to confocal microscopy that relies on single-photon excitation, MPM utilizes near-infrared (NIR) radiation that increases the maximum imaging depth from a few 10 μm up to nearly 1 mm in certain types of tissues, such as brain²⁰⁰. Further advantages over confocal microscopy are an inherent submicron spatial resolution that still allows revelation of subcellular details and fine tissue structures; reduced scattering and absorption due to longer excitation wavelengths and significantly reduced phototoxicity and photobleaching in out-of-focus regions²⁰¹. All other currently available optical imaging techniques either lack the capability to image deeply in scattering tissue or lack submicron spatial resolution. In addition, MPM enables excitation of the characteristic ultraviolet absorption bands of endogenous fluorophores and second harmonic generation (SHG) of anisotropic biological structures like collagen and skeletal muscle fibers that possess large hyperpolarisabilities²⁰²⁻²⁰⁴.

However despite these advantages, MPM up to now faces significant limitations. In biomedical research, MPM is typically carried out using a Titanium:Sapphire (Ti:Sa) laser that emits light in the range of 680 to 1080 nm. These lasers excite blue, green and yellow fluorophores and fluorescent proteins with satisfactory efficiency. In contrast the excitation of red and NIR fluorophores is inefficient without applying very high laser powers that provoke light-induced toxicity²⁰⁵. Moreover, penetration depth and the associated spatial resolution decrease with increasing optical density in connective and cell-rich tissues like skin²⁰⁶, muscle²⁰⁷ or tumors¹⁴⁸ caused by light scattering²⁰⁸.

To investigate invasion of cancer cells and interaction with surrounding host-tissue the improvement of these mentioned limitations is of particular importance. The use of red and NIR dyes in addition to blue to yellow dyes would broaden the spectrum of structures that could be visualized simultaneously in the living animal and facilitate spectral separation. Moreover, many red-shifted dyes have become standard sensors for transcutaneous detection of deep tissue lesions in live animals, including whole-body imaging²⁰⁹. Last but not least, an increase in depth for subcellular resolved microscopy is necessary to visualize processes happening deep in the tumor such as central necrosis or tumor-host-cell interaction in the tissue depth.

2.4 Purpose of the study

Although aspects of cancer invasion in general and especially fibrosarcoma and melanoma invasion are known from *in vitro* studies, these data neglect the complexity of live tissue whereas orthotopic *in vivo* models usually lack sufficient transparency and controlled stability for direct and repetitive access to the invasion cascade.

The general aim of this study was to set up an orthotopic model for visualizing the key steps leading to tumor growth and invasion into healthy tissue and exploit this model for molecular studies on cancer invasion and response to therapy.

The specific aims were:

- to technically modify multiphoton microscopy for improved tissue penetration, imaging of red fluorophores, and visualization of interaction between the tumor and the surrounding tissue;
- to establish an *in vivo* model for HT-1080 fibrosarcoma and B16/F10 or MV3 melanoma cell invasion in interstitial mouse dermis as a matching model to previously used 3D collagen lattices;
- to validate *in vivo* migration pattern found *in vitro*;
- to determine molecular basics of invasion *in vivo*;
- to test consequences of clinical standard treatments on invasion, particularly ionizing radiation and chemotherapy, but also molecular and innovative therapy approaches (anti-EGFR, anti-integrin).

3 RESULTS

3.1 Advantages of near-infrared and infrared multiphoton microscopy for intravital imaging

Multiphoton microscopy (MPM) is the method of choice for investigating cells and cellular functions in deep tissue sections and organs. To make MPM feasible for deep tumor imaging initial experiments aimed to optimize excitation and detection efficiency for the used tumor model and fluorescent dyes.

3.1.1 Two-photon excitation and emission spectra of red dyes and fluorescent proteins

The measurement system consisted of a Ti:Sa femtosecond laser synchronously pumping an optical parametric oscillator (OPO) with a periodically poled crystal tuned in the ranges of 715 to 980 and 1060 to 1450 nm, respectively¹⁴⁴.

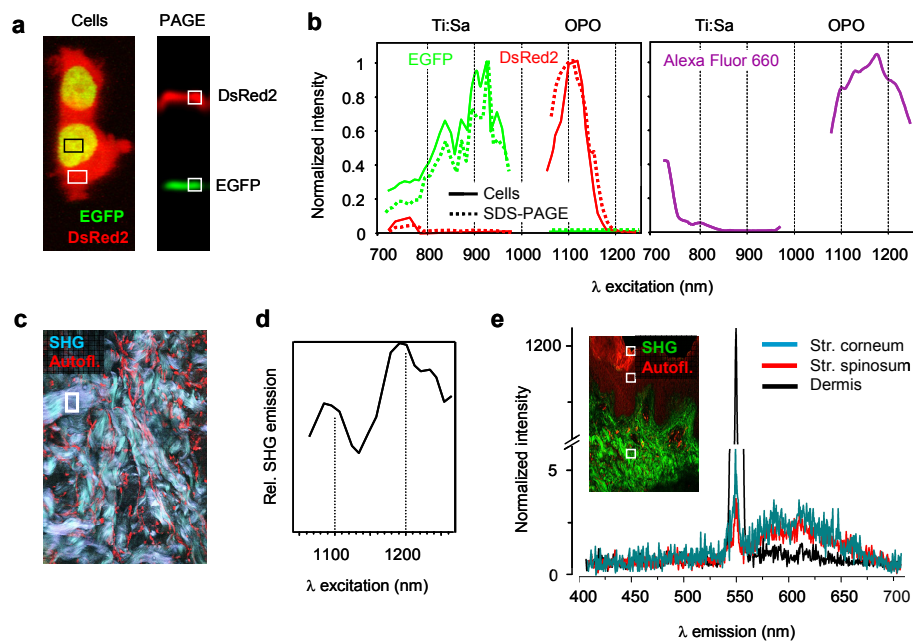


Figure 4. NIR and IR 2-photon excitation and emission spectra. (a) HT-1080 cells expressing cytoplasmic DsRed2 and Histone-2B-EGFP before and after SDS-PAGE under native conditions. Boxes, regions of measurement. (b) 2-photon excitation spectra of EGFP, DsRed2, and Alexa Fluor 660. Solid lines, isolated protein in SDS-PAGE or soluble Alexa Fluor 660. Dashed lines, living dual-color cells. (c) IR 2-photon generated second harmonic signal. Box, region of measurement. (d) SHG spectra from collagen-rich regions of native human dermis. (e) Emission spectra at 1100 nm from human skin. The boxes indicate the regions in stratum corneum, epidermis, and dermis where the spectra were taken from. The SHG peak for fibrillar collagen is at half of the excitation wavelength.

The excitation and emission spectra of EGFP and DsRed2 were obtained from living dual-color human fibrosarcoma cells (HT-1080) expressing both nuclear EGFP/Histone-2B (H2B) and cytoplasmic DsRed2²⁰⁹ and isolated proteins, extracted from the cells and electrophoretically separated (Fig. 4a). The most efficient excitation of EGFP was at 930 nm, as reported²¹⁰, but it could not be excited above 1060 nm (Fig. 4b). In contrast, DsRed2

showed a minor excitation peak at 760 nm and highly efficient excitation from 1090 to 1120 nm (Fig. 4b). Alexa Fluor 660 showed a strong excitation band between 1070 to 1300 nm with peaks at 1100 and 1180 nm (Fig. 4b). To simultaneously detect fluorescence and other specific signals emitted from tissue structures like second harmonic generation (SHG), optimal laser wavelengths for combined excitation were determined. Fibrillar collagen exhibited narrow SHG bands from a broad input wavelength range with peaks at 1100 and 1180 nm (Figs. 4c, d). The ratio of SHG to autofluorescent signals was approximately 500:1 which exceeds typical SHG to autofluorescence ratios obtained with Ti:Sa lasers (Fig. 4e).

Thus, 1100 nm is a suitable wavelength emitted by the OPO for simultaneous excitation of DsRed2, Alexa Fluor 660 and SHG of collagen-rich tissue. For excitation of EGFP a subsequent scan with near-infrared wavelengths is necessary.

3.1.2 Photobleaching and photodamage

For live microscopy, photobleaching of fluorophores is associated with *de novo* formation of reactive oxygen intermediates and heat causing cytotoxicity²¹¹ and critically limits imaging sensitivity and cell viability during repeated exposure to laser light.

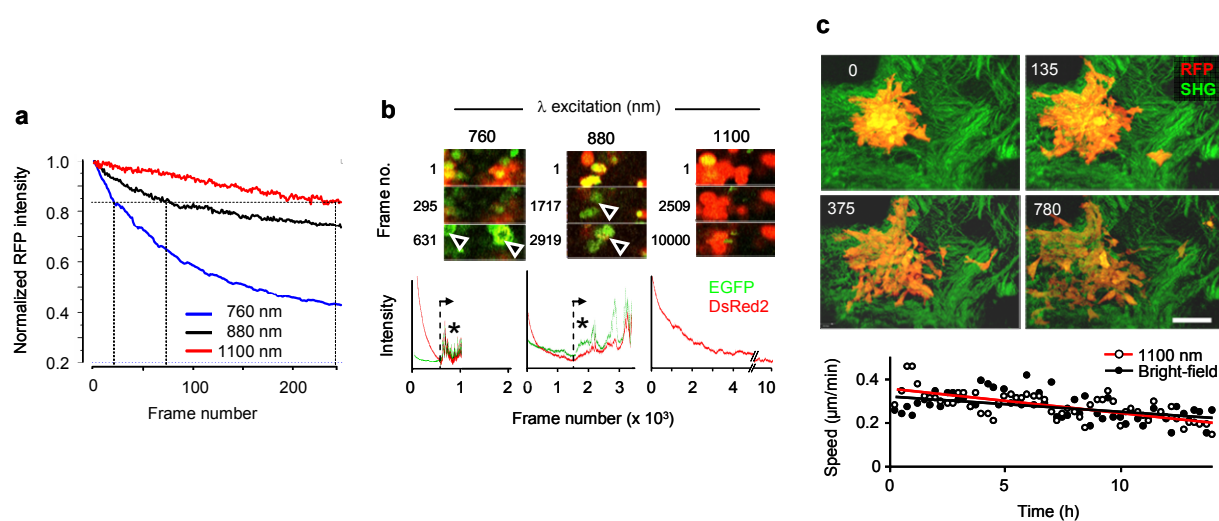


Figure 5. Photobleaching, phototoxicity, and tissue penetration of IR-MPM. (a) Photobleaching of DsRed2 measured as decrease in emission during consecutive scanning at 760, 880, and 1100 nm excitation wavelengths and a power of 75 mW. The samples were subjected to 250 consecutive scans and the emission intensity was quantified as average pixel intensity of the entire scanning field and normalized to the intensity of the first frame. Dashed lines, bleaching efficiency normalized to the end-point of the decay of emission intensity at 1100 nm. (b) Protein condensation due to continuous excitation. Continuous imaging of dual-color HT-1080 cells at a high excitation power (110 mW) and a frame rate of 2.8 fps. Arrowheads and asterisks indicate aggregates of condensed protein. (c) Undiminished emigration of HT-1080 cells from a multicellular spheroid on a dermis slice during continuous excitation at 1100 nm and 117 mW power in the focus. The numbers indicate the elapsed time (min). The population velocity obtained by cell tracking was compared to cells monitored by conventional bright-field microscopy. The near-completely overlapping regression curves of migration speed are shown. Bar, 150 µm.

Photobleaching of DsRed2 in live cells at 1100 nm was 4- and 10-times lower compared to excitation at 880 and 760 nm, respectively (Fig. 5a). At high laser power of 117 mW, respective aggregation of EGFP and DsRed2 in live cells was reached after 500 and 1700

consecutive scans corresponding to 3 and 10 min illumination time at 760 nm and 880 nm (Fig. 5b). In contrast, no protein aggregation was detected after up to 10000 scans or 1 hr of exposure time using an excitation wavelength of 1100 nm (Fig. 5b). To exclude latent photodamage, actin-driven cell migration was tested due to its immediate energy-dependency and sensitivity to physical or chemical assault. No signs of compromised migration or laser-induced toxicity including cell rounding, protein condensation, or loss of fluorescence were detected despite continuous sample exposure to 1100 nm excitation over 14 h (Fig. 5c). Thus, IR-MPM shows low levels of photobleaching and photodamage.

3.1.3 Deep tissue imaging

In contrast to visible light NIR radiation is poorly absorbed by water. Nevertheless water absorption increases for excitation wavelengths above 900 nm²¹² and thus imposes a potential limitation of IR-MPM for biomedical applications in live, hydrated tissues. Despite this increase in light absorption by water, the maximum imaging depth for fibrillar collagen in native human dermis was increased by 2-fold for SHG excitation at 1100 nm compared to 880 nm excitation (Fig. 6a).

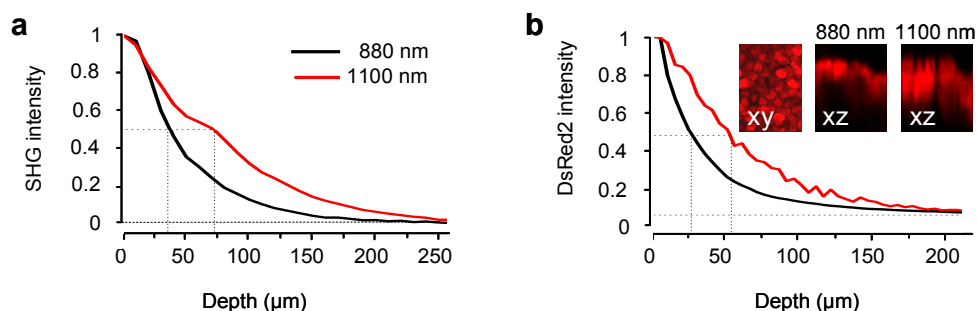


Figure 6. Deep IR multiphoton microscopy. Penetration depth measurements for SHG (a) of 4 mm thick native human dermis slice and for fluorescence (b) of dual-color HT-1080 cell spheroid of 1 mm in diameter. For both, 3D dermis or multicellular spheroid, excitation of 880 and 1100 nm was used at an intensity of 75 mW and the respective SHG or fluorescence emission was collected at identical PMT sensitivity. Dashed lines in (a) and (b) indicate 50% emission signal intensity measured as normalized mean pixel intensity of the entire scanning field.

Likewise, DsRed2 fluorescent cells in aqueous medium could be detected in 2-fold deeper layers within a solid multicellular spheroid (Fig. 6b). Consequently, in thick xenografts of dual-color HT-1080 cells, eight days after implantation into the mouse dermis, the detection of DsRed2 signal at 1100 nm was also increased 2-fold reaching up to 500 μm tissue penetration, compared with excitation at 880 nm (Figs. 7a–c).

Another limitation for deep tissue MPM compromising image quality is the decrease in spatial resolution with increasing imaging depth. Figure 7d shows that despite sufficient signal coming out of deep tissue regions, the resolution of cell borders and subcellular detail is strongly affected in scattering tumor tissue. However, compared to NIR-MPM IR-MPM provides resolution sufficient to image cellular details like the negative signal of the nucleolus in invasion areas close to the tumor edge down to 200 μm depth (Fig. 7e;

arrowhead, EGFP-negative nucleolus). Thus, for a certain depth window and dependent on tissue density IR-MPM delivers images of unrivaled quality.

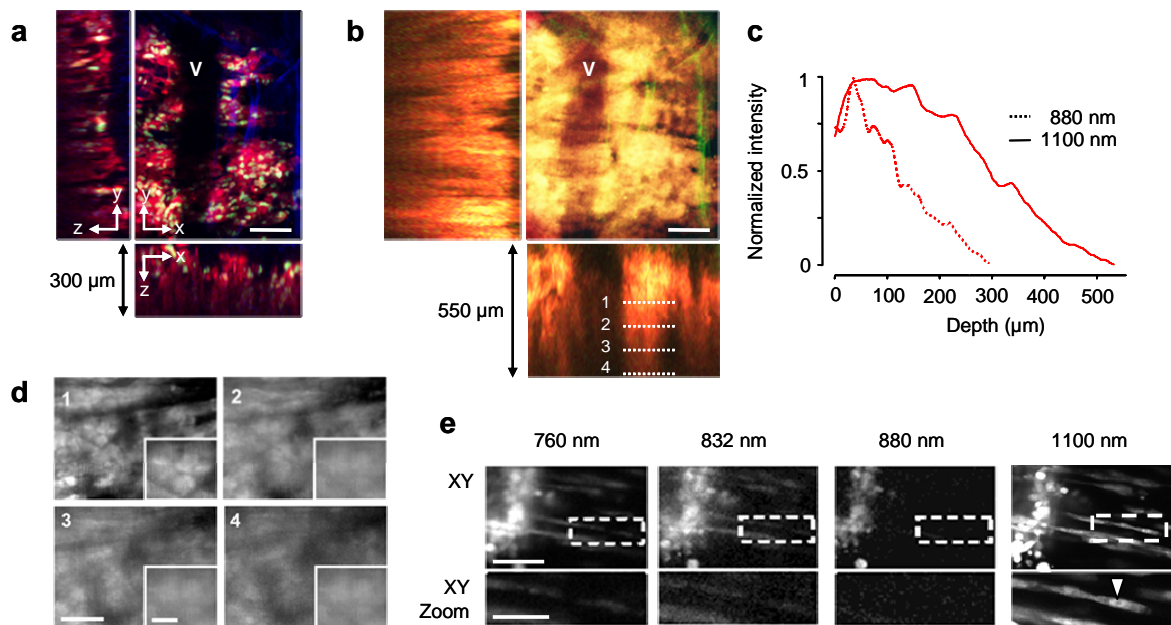


Figure 7. Deep tissue IR-MPM of DsRed2 expressing xenografts *in vivo*. (a), (b) 3D data stack of human dual-color xenograft of HT-1080 fibrosarcoma cells implanted into the mouse dermis using (a) 880 and (b) 1100 nm excitation at a power of 75 mW in the sample. Step-size in z-direction was 5 μm. V indicates a region with a large blood vessel (negative contrast). (c) Normalized fluorescence intensity for DsRed2 as a function of penetration depth. The initial slope of the intensity profile corresponds to the position of the lesion 10 to 50 μm below the dermis interface. (d) Decrease in spatial resolution with increasing penetration depth using 1100 nm excitation in the z-planes indicated by the dashed lines in (d). The insets show magnified details from the overview images. (e) Deep tumor region (170 μm) with invading cells at different excitation wavelengths. Excitation power in the focal plane (125 mW) and PMT sensitivity were kept constant. Amplification of residual signal. Bars, 100 μm ((a), (b), (e)), 50 μm ((d)); (e), XY details and 20 μm ((d), insets).

Taken together, IR-MPM is superior to NIR-MPM regarding excitation efficiency of red dyes and internal tissue signals, reduced phototoxicity and imaging depths. Consequently, to display blue and green emission together with red fluorescence signal combined IR and NIR excitation was used throughout this study.

3.2 Establishment of a modified orthotopic intradermal tumor xenograft model to monitor *in vivo* growth and invasion

To establish an orthotopic xenograft model for mechanistic studies on tumor cell invasion pattern and kinetics *in vivo* the dorsal skinfold chamber (DSFC) model was set up to allow repetitive non-invasive imaging of the same lesions over time. Additionally, stably transfected, double-labeled (H2B-EGFP, cytoplasmic DsRed2) variants of established cancer cell lines (human fibrosarcoma cell line HT-1080; human amelanotic MV3 melanoma cells; murine melanotic B16/F10 melanoma cells) allowed direct visualization of tumor development *in vivo* without any staining procedures.

3.2.1 Modification of the dorsal skinfold chamber towards a 3D environment

First, cell application into the skinfold chamber as drop-on of pelleted tumor cells onto the dermal tissue was tested (Fig. 8a, c). It resulted in tumor growth between two different interfaces: (i) the underlying mouse dermal tissue and (ii) the overlying cover slip. Within few days after application, concentric, spherical tumors were formed that induced *de novo* angiogenesis yet lacked signs of cell invasion onto the host tissue (Fig. 8c, details). To provide better access to the surrounding host tissue and thereby avoid tumor growth at a 2D interface between dermis and cover slip, in a second trial pelleted tumor cells were injected directly into the deep dermis and adjacent subcutaneous connective tissue layers (Fig. 8b, d). This modified application procedure allowed to monitor early tumor stages, including early growth and tissue invasion (Fig. 8d).

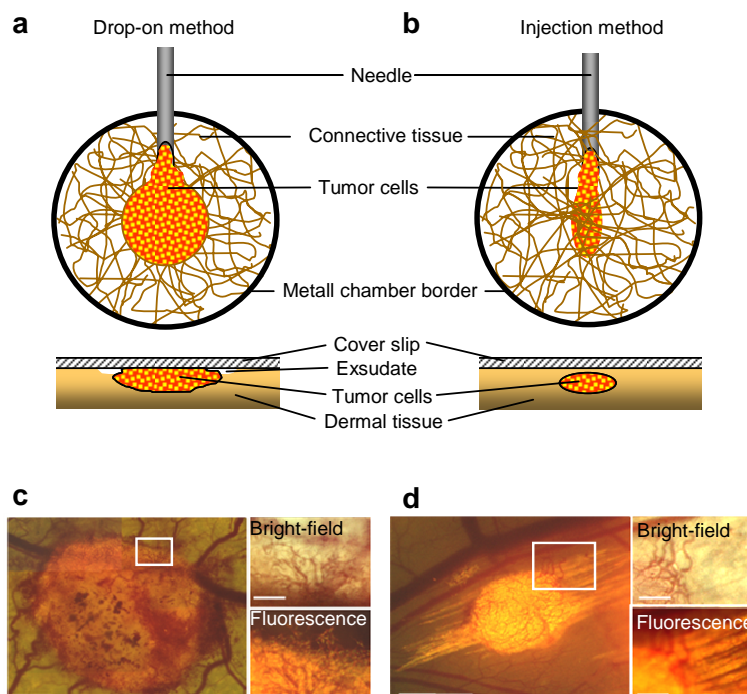


Figure 8. Comparison of drop-on and injection methods of HT-1080 fibrosarcoma cells in the dorsal skin-fold chamber. Principle of cell application, position of growth (a, b), and macroscopic tumor morphology after 6 (c) and 7 days (d) visualized by bright-field and epifluorescence microscopy. In established models a suspension or a pellet of cells is allowed to adhere to the interface of the surgically prepared dermis, leading to 3D tumor growth between the dermis layer and cover slip (a, c). The injection of a cell pellet with a small needle into the dermis prevents interaction with the cover glass and yields growth inside the dermis (b, d). Bars, 1 mm (overview) and 250 μ m (details).

Using NIR-excited MPM it could be proven that tumors were completely surrounded by dermal and subcutaneous tissue structures (Figs. 9a-d, compare to skin layers in 9e; see also Movie 1). The upper tumor region was bordered by stroma (Fig. 9a; stromal cell nuclei visible in 9f, detail) including collagen fibers (Fig. 9a, black arrowheads) and striated muscle strands (Fig. 9a, white arrowheads) visualized by SHG, as well as perfused blood vessels of the deep dermal plexus. By contrast to anatomically ordered, linear blood vessels surrounding the tumor margin (Fig. 9a, green arrowheads), inner tumor regions contained irregularly-shaped, newly-formed vessels (Fig. 9d, blue arrowheads) and, with increasing penetration depth rarefied collagen fiber networks (Figs. 9b-d).

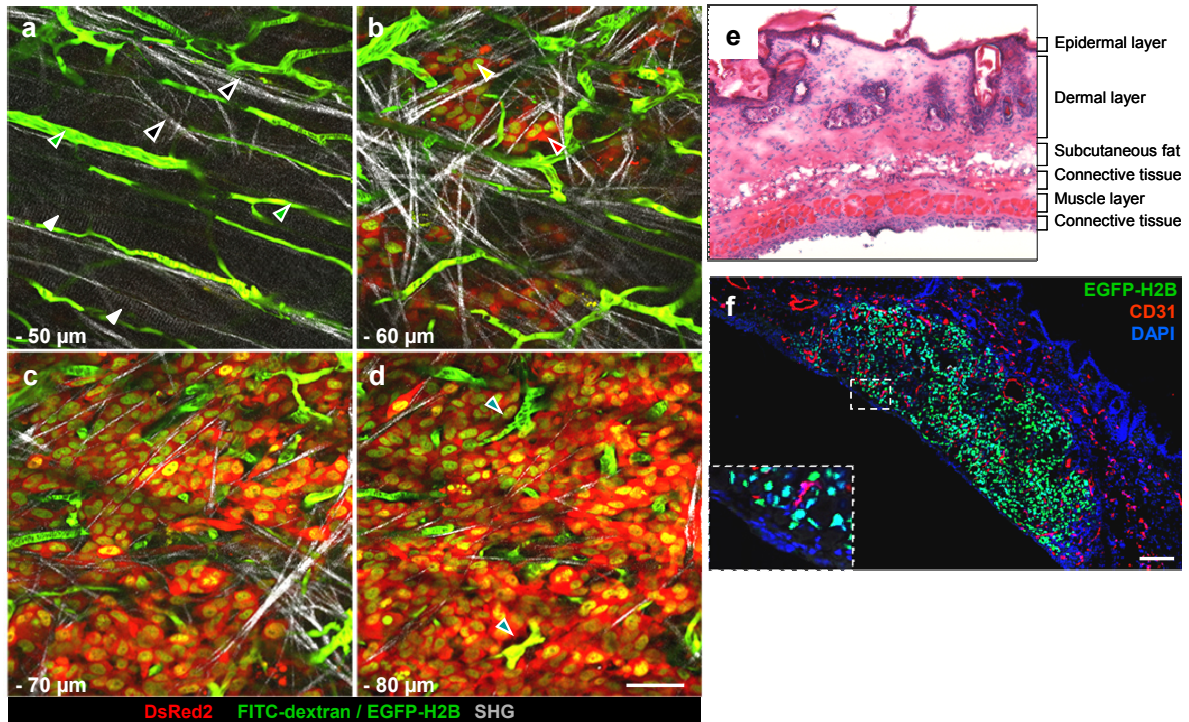


Figure 9. Dermal surrounding of HT-1080 dual color tumors (**a-d**) Near-infrared multiphoton microscopy. Z-series from the tumor margin (-50 μm) to intratumoral region (-80 μm) of a 6 day-old tumor (cytoplasm, red; nuclei, yellow). Perfused blood vessels (green) were visualized by FITC-dextran injection, preexisting linear-shaped (green arrowheads) and irregular-shaped neo-vessels (blue arrowheads). Collagen fibers (black arrowheads) and muscle strands (white arrowheads), detected by second harmonic generation (gray scale). Bar, 50 μm . See also Movie 1. Compare to (**e**) Dorsal skin-fold chamber skin preparation. H&E staining. Skin layers are named. (**f**) Cross-section of skin containing a xenograft monitored by confocal microscopy. Tumor mass visualized by tumor nuclei containing H2B-EGFP (green/cyan), blood vessels stained by CD31 (red); stromal cell nuclei stained by DAPI (blue). Inset illustrating that tumor is surrounded by stromal cells on coverslip side. Bar, 250 μm .

Thus, after intradermal injection, the tumors are surrounded by an intact tumor-stroma interface including extracellular matrix, muscle cells, and blood vasculature.

3.2.2 Kinetics of tumor growth

In the modified DSFC model, xenograft growth led to sphere- to ovoid-shaped tumors in the horizontal plane (i.e. in parallel to the cover glass of the chamber) and an ellipsoid, bean-shaped cross-section (Fig. 9f). Consequently, the formula to calculate spherical tumor volumes (Tumor volume (V) = (tumor width)² x (tumor length)/6) was modified and additionally divided by two to best approximate the flattened vertical dimension. Growth of human fibrosarcoma xenografts (HT-1080) started initially slowly (volume doubling within 6 days), but after the onset of angiogenesis (between day 3 and 4; Fig. 10a, insets), a second growth phase yielded in accelerated growth (volume doubling within 3 to 4 days; Figs. 10b). The onset of invasion occurred 2 to 3 days after implantation and new invasion zones appeared during the complete observation period (Fig. 10a, white arrowheads). Thus, the kinetics of angiogenesis and exponential tumor

growth are here also connected, as described for other tumor models²¹³ whereas local invasion occurred independently.

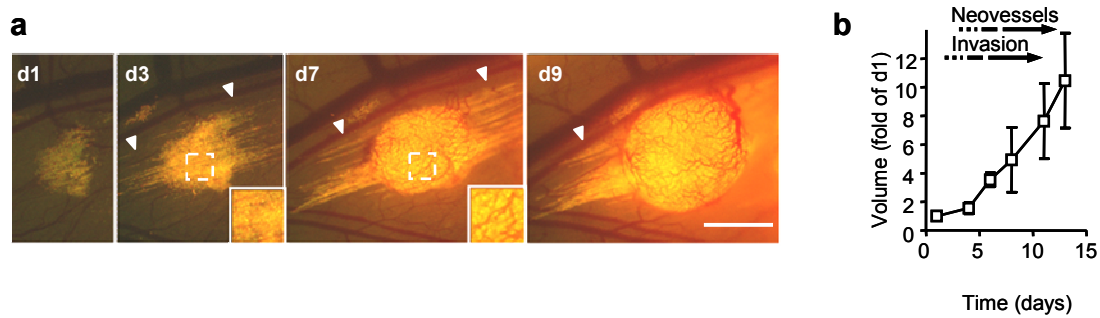


Figure 10. Phases of HT-1080 tumor growth. (a) Representative time course of xenograft growth and invasion (white arrowheads) monitored by epifluorescence microscopy. Insets, absence (day 3) and presence (day 7) of neovessels. Bar, 1 mm. (b) Tumor volume growth normalized to the size of day 1. Mean values \pm SD (n = 9).

3.2.3 Kinetics of mitosis and apoptosis

In addition to volume measurement, the underlying mechanisms were derived from the presence of mitotic and apoptotic nuclear morphologies *in situ*.

Cells that underwent mitosis were determined using NIR-MPM of the H2B-EGFP label (Fig. 11a). The high spatial resolution allowed the identification of all mitotic stages (Fig. 11a, details). Dividing cells of mitotic prophase showed condensed chromosomes with thread-like EGFP signal, in metaphase the chromosomes were aligned, and during anaphase segregated again (Fig. 9a, details). The Mitotic frequencies varied between 0% and 6% in the course of tumor progression with a steady-state average of 1 to 2% (Fig. 9b).

Likewise, the frequency of spontaneous apoptosis as a measure of cell viability was derived from the H2B-EGFP label based on EGFP-positive nuclear fragments and averaged below 1% (Fig. 9).

Thus, net tumor growth is determined by mitotic rates that exceed the apoptotic incidence.

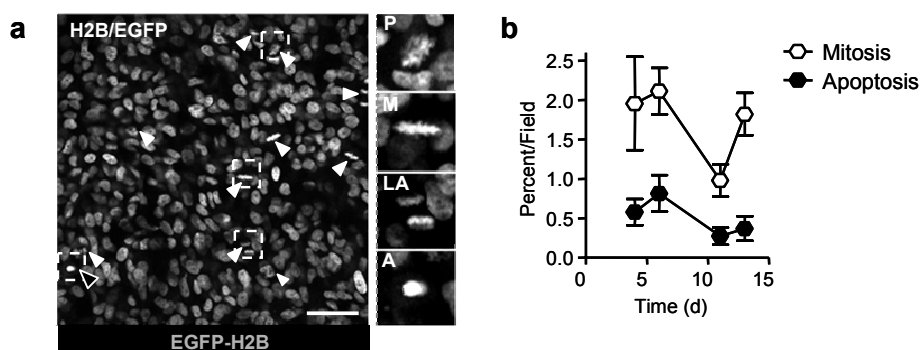


Figure 11. Quantification of mitotic and apoptotic fractions. Intravital detection of nuclear morphology of tumor cells containing expressing H2B-EGFP. (a) 3D reconstruction of a central tumor zone using multiphoton microscopy at excitation wavelength of 832 nm. Mitotic (white arrowheads) and apoptotic figures (black arrowhead) at d6. Bar, 50 μ m. Insets show prophase (P), metaphase (M), late anaphase (LA) and apoptotic figure (A). (b) Time-resolved quantification of the frequency of mitotic and apoptotic nuclei. Data show the means \pm SEM of 10 to 20 independent fields from 3-4 independent tumors.

3.2.4 Temperature dependence of intradermal tumor models

Establishing an orthotopic tumor model includes not only the correct implantation site but also environmental conditions. Mice are kept usually at room temperature (21°C), thus we hypothesized that the metal chamber on the back could cool down the tissue contained therein and thereby negatively impact tumor cell activity, such as mitosis or motility. Therefore, we tested whether the maintenance of mice at lower (21°C) or higher temperature (28°C) has an influence on tumor growth and invasion, using HT-1080 human fibrosarcoma and murine B16/F10 melanoma cells.

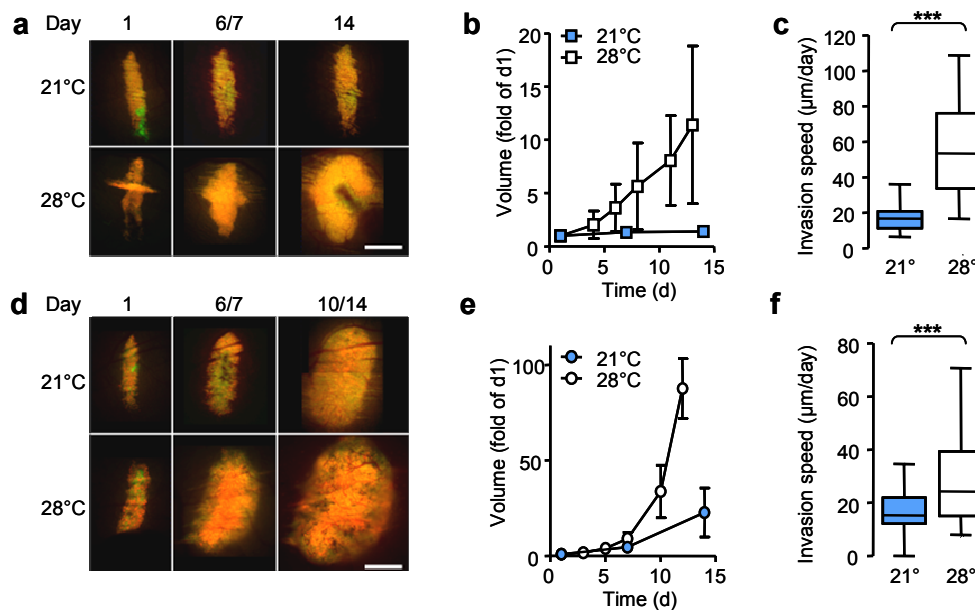


Figure 12. Tumor growth and collective invasion dependent on temperature of mouse housing. Time-course of HT-1080 (a-c) and B16/F10 (d-f) xenograft growth and invasion at 21°C and 28°C monitored by epifluorescence microscopy. Bars, 1 mm. Reduced tumor growth of HT-1080 (a) and B16/F10 (e) at 21°C compared to 28°C. Mean values \pm SD (n = 3-19). Quantification of HT-1080 (c) and B16/F10 (f) collective invasion speed between d7 and d14 at 21°C and 28°C. Median, 25th and 75th percentile (box) and 5th/95th percentiles (whiskers; 38 to 51 strands). *** p<0.001 (unpaired Mann-Whitney U-test).

Compared to 21°C, tumor growth in mice maintained at 28°C was strongly accelerated in both, HT-1080 fibrosarcoma (Figs. 12a, b) and B16/F10 melanoma grafts (Figs. 12d, e). HT-1080 xenografts at 28°C entered an accelerated growth phase between day 4 and 6 and reached a 10-fold volume at day 13, whereas tumors from mice maintained at 21°C did not show growth exceeding the initial volume. Neovascularization was delayed by seven days at 21°C compared to 28°C housing temperature, but largely intact (Fig. 12a). Likewise, invasion activity was significantly reduced (Fig. 12c). Between d7 and d14 after implantation HT-1080 cells invaded in average 50 μ m/d at 28°C, at 21°C this was decreased to 15 μ m/d. The progression of dual-color B16/F10 melanoma lesions was also temperature-sensitive. The tumor volume at the end-point of maintenance at 28°C (day 12) reached approx. 100-fold of the initial size, whereas at 21°C a 20-fold volume was

reached (Figs. 12d, e), corresponding to growth inhibition of 80%. Likewise, the invasion efficiency of B16/F10 cells was reduced by 40% (Fig. 12f).

Thus, the biological activity of two different tumor models is compromised if mice carrying the DSFC are housed at room temperature. This includes cell growth, neoangiogenesis and local invasion. Consequently, to obtain a temperature environment for tumors comparable to the conditions in natural skin, tumor bearing mice were housed at 28°C.

3.3 Efficient and diverse fibrosarcoma invasion *in vivo*

As direct consequence of an intact 3D stroma-tumor interface fibrosarcoma cells were able to engage with stromal components and invade into the surrounding tissue.

3.3.1 Diversity of invasion modes

Different morphological and functional types of cell invasion into non-tumor regions developed spontaneously, including single cell and collective invasion modes (Fig. 13a). Whereas a minor proportion of tumors lacked invasion or showed dissemination of individual single cells that lost cell-cell junctions, the majority of the lesions exerted collective invasion (Fig. 13b). Two types of collective invasion were further distinguished. The diffuse type originated from individual single cells that were followed by an irregularly-shaped mass invasion. Alternatively, solid, well-organized strands containing multiple cells at constant diameter invaded in a finger-like fashion outward from the tumor edges (Fig. 13a). The underlying mechanisms of these different invasion modes are presently unclear, but likely reside in structural and molecular heterogeneity of the tissue structures encountered by tumor cells.

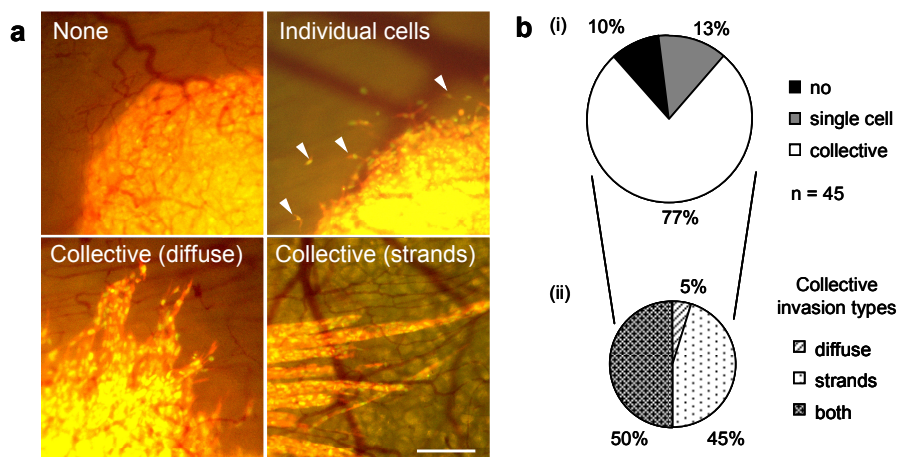


Figure 13. Invasion modes of HT-1080 dual color cells *in vivo*. **(a)** Classification of invasion types 6 days post injection. Lack of invasion (top, left) and disseminating single cells (top, right; white arrowheads), diffuse or compact strand-like collective invasion (lower panels). Bar, 250 μ m. **(b)** Frequency of different invasion modes displayed in **(a)** from 45 consecutive independent tumors. Bar, 100 μ m.

3.3.2 Visualizing the tumor-stroma interface and guidance structures of invasion

Tumor cell migration and invasion are dependent on the physical interaction of the tumor cell with surrounding structures or extracellular or cellular stroma components to generate (protrusion or traction) force. The tissue structures which guide invasion *in vivo* were thus monitored by intravital multiphoton imaging.

3.3.2.1 Collagen, muscle strands and fat tissue

SHG microscopy revealed that a fraction of collective fibrosarcoma strands was associated with aligned collagen fibers or adjacent striated muscle fibers (Fig. 14a). Conversely, nearby fatty connective tissue predominant single-cell invasion was observed to be followed by diffuse and/or collective invasion (Fig. 14b). Here, individual cancer cells moved along fat cells, which were visible by their negative fluorescence signal (Fig. 14b, white asterisks) caused by the absorption of the laser light. Eventually this migration of tumor cells was followed by complete inclusion of fat cells by the tumor mass.

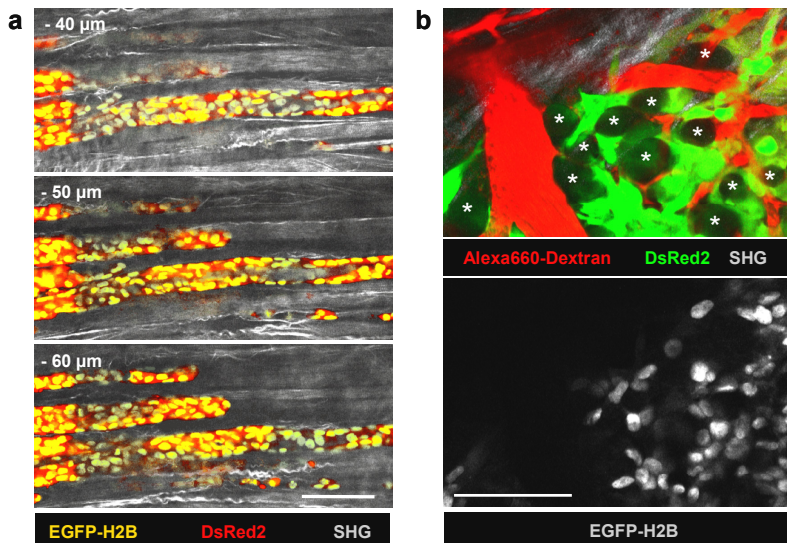


Figure 14. Collagen and fat tissue as guidance structures of invasion. **(a)** Orientation of collective invasion strands along striated muscle fibers on day 11. Imaging depth is indicated. **(b)** Single cell invasion into fat tissue followed by diffuse and, in part, collective invasion. Contrast-deficient roundish fat cells (asterisks) surrounded by HT-1080 cells. Excitation wavelength was 1100 nm for detection of perfused blood vessels (Alexa Fluor 660-dextran, red), tumor cytoplasm (false-color green), SHG (grayscale) and 832 nm for tumor cell nuclei (white). Bar, 100 μm.

3.3.2.2 Lymphatic Vessels

Further pro-invasive tissue structures were lymphatic vessels (Fig. 15). The small FITC-tagged peptide LyP-1 binds to the cell surface protein p32 on macrophages incorporated into walls of tumor-associated lymphatic vessels²¹⁴. After intravenous injection it bound to lymph vessels of the tumor margin, but not to those in the central region of the tumor (data not shown). Individually migrating cells and multicellular strands were aligned along the outer surface of lymph vessels (Fig. 15; black arrowheads). In addition, a small

proportion of fibrosarcoma cells was also located inside lymph vessels, suggestive of early lymphatic intravasation (Fig. 15, white arrowheads).

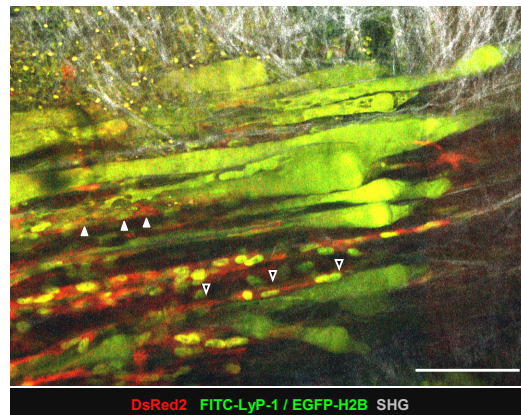


Figure 15. Invasion of HT-1080 cells along lymphatic vessels detected with FITC-conjugated LyP-1 peptide. Intra- (white arrowheads) and perilymphatic invasion (black arrowheads). Projection of 3D stack. Bars, 100 μ m.

3.3.2.3 Blood Vessels

Moreover, collective invasion occurred along blood vessels aligned to the longitudinal tissue of the deep dermis (Fig. 16).

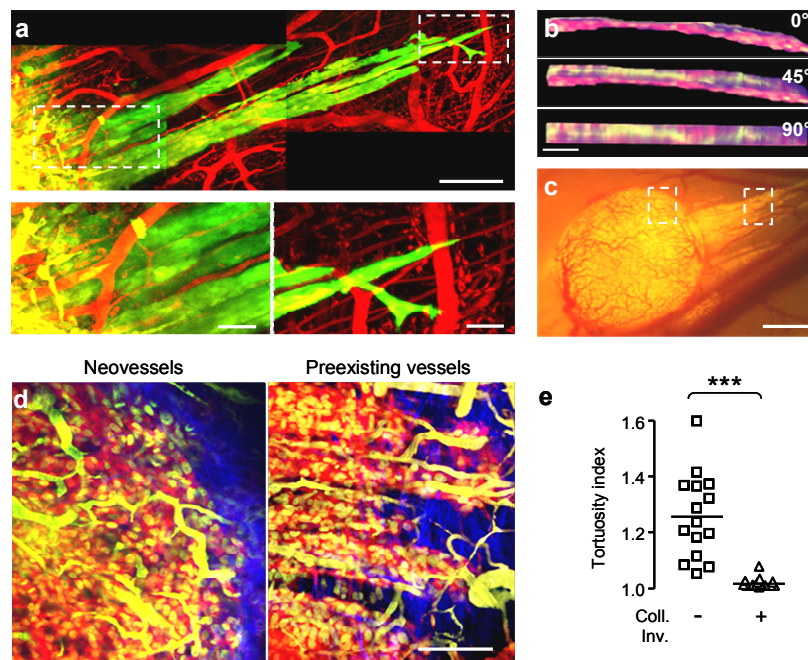


Figure 16. Collective invasion guided by preexisting blood vessels. (a) Collective invasion strands in parallel alignment with perfused blood vasculature. Reconstruction at 1100 nm excitation of tumor cells (DsRed2, false-color green) and blood vessels (Alexa Fluor 660; red) of 250 μ m deep zone. Details, strand alignment along blood vessels at the tumor basis as well as the leading edge (dashed boxes). Bars, 100 μ m and 25 μ m (details). (b) Still images of 3D rotation of multicellular tumor strand (red) cuffing a central blood vessel (green). See also Movie 2. Overview epifluorescence (c) and high-resolution MPM reconstruction (d) of collective invasion along linear but not irregularly-shaped vessels. Bars, 50 μ m (a), 1 mm (c), 100 μ m (d). (e) Tortuosity of vessels in regions devoid of invasion compared to vessels associated with collective invasion strands. Data show the medians (horizontal line) of individual vessels from 5 independent lesions. *** $p < 0.001$ (unpaired Mann-Whitney U-test).

To test whether collective strands directly engaged with blood vessels, vessel structures were fluted with fluorescently labeled dextran solutions after intravenous injection. Dextran molecules of 40 kD size were washed out rapidly after 2 to 3 min into the vessel

surrounding tissue, whereas the 70 kD variant was retained within blood vessels for longer time periods, allowing imaging for 3 to 4 hours (data not shown). The conjugation of dextran molecules with Alexa Fluor 660 further increased the imaging quality allowing sustained detection of vessels together with cellular morphology and nuclear states by sufficient spectral separation from H2B-EGFP and cytoplasmic DsRed2.

Blood vessel display revealed that multicellular strands were in direct anatomic association with perfused capillaries and small vessels either adjacent to or completely embedding individual vessels (Figs. 16a, b; see also Movie 2). This vessel guided invasion was selective, as only anatomically linear, constitutively preexisting vessels but not irregularly shaped, more tortuous neovessels promoted collective invasion (Figs. 16c-e). The lack of an invasion-promoting role of neovessels was further supported by the onset of invasion 1 to 3 days prior to tumor-induced neoangiogenesis (Figs. 10a).

Taking the availability of various guidance structures into account, fibrosarcoma invasion *in vivo* is diverse in response to the heterogeneity of encountered tissue structures.

3.3.3 Invasive growth

Time-lapse MPM imaging of collective strands revealed collective invasion as multi-component process which included cell movement, the retention of cell-cell junctions, and mitotic activity (Fig. 17, see also Movie 3).

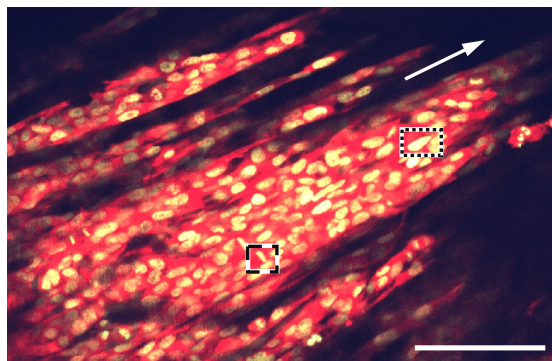


Figure 17. Invasive growth: collective invasion coupled to proliferation in HT-1080 dual-color xenografts. Multicellular collective invasion zone (cytoplasm red, nuclei yellow). Dotted box, position nuclear dynamics comp (Fig. 18b). Dashed box, position mitotic dynamics comp (Fig. 19a). Arrow, direction of invasion. See also Movie 3. Bar, 100 μm .

3.3.3.1 Invasion efficiency

To determine the invasion speed of collective invasion time-lapse MPM at various organizational and time levels was used for quantitative analysis.

Using different observation intervals, i.e. for individual nuclei minutes (Fig. 17, dotted box; Fig. 18a; see also Movie 3), for individual strand tips hours (Fig. 18b), and for complete invasion strands days (Fig. 18c), a uniform mean velocity of 100 $\mu\text{m}/\text{day}$ was measured (0.1 $\mu\text{m}/\text{min}$; Fig. 18d) with an absolute range from $-125 \mu\text{m}$ (spontaneous retraction) to 260 μm . This migration speed is approximately 3- to 5-fold slower than

single-cell speeds obtained from in 3D collagen lattices *in vitro*¹⁴ and 30-fold slower compared with amoeboid single cells in the MMTV breast cancer model *in vivo*^{155,173}.

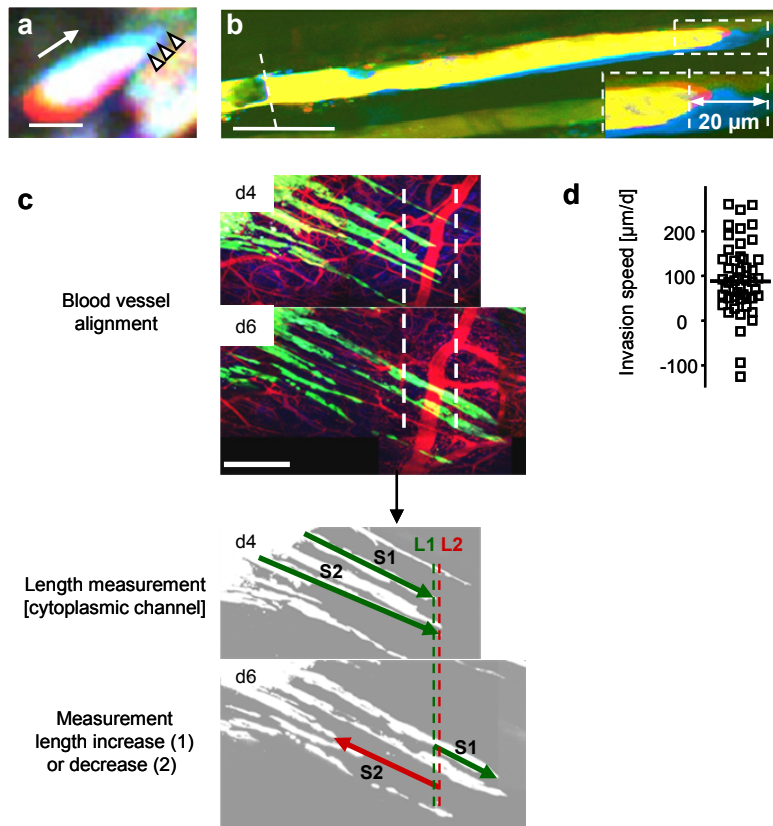


Figure 18. Collective invasion speed. (a) Nuclear dynamics in multicellular invasion zone obtained from dotted box in (Fig. 17). Arrowheads, position of nuclear tip at different time points: 0 min, white; 15 min, cyan; 30 min, blue. Arrow, direction of invasion. (b) Protrusion of the tip of a multicellular invasion strand monitored by time-lapse MPM. The strand was normalized in position (dashed line) and the movement within 4 h displayed in false color (t1, yellow; t2, magenta; t3, blue; arrows, position change of the leading edge). (c) Invasion speed of multicellular strands obtained from repetitive 3D microscopy over days. Collapsed MPM stacks (1100 nm excitation) were obtained at different time-points and aligned in position using the (constant) blood vessel pattern (white lines). Fluorescence channel with cytoplasmic signal used to measure length of various strands e.g. strand 1 and 2 (S1, S2). Starting from former position of strand tip (S1 = L1, S2 = L2) increase (S1, green) or decrease (S2, red) in length is measured at time point 2. (d) Invasion speed of collective strands. The migrated distance per day was measured from the position change of individual tips from d4 to d6. Negative values represent occasional retraction of the tip of a strand. Horizontal line, median.

To generate representative and statistically robust data of invasion speed, 3D stacks were collapsed and the invasion distance of each strand was quantified for subsequent days of tumor progression (Fig. 18c). As topographic reference blood vessels in non-invaded dermis were found to be stable in position and primarily used to identify similar regions for alignment of images taken in the course of 2 weeks (Fig. 18c, white dashed lines). The cytoplasmic DsRed2 signal was then used to determine strand lengths. Starting from the former position of a strand tip (Fig. 18c, colored dashed lines) length increase (further invasion; Fig. 18c, S1, green arrow) or decrease (spontaneous retraction; Fig. 18c, S2, red arrow) to a second imaging time point was measured as positive or negative speeds, respectively.

3.3.3.2 Components of invasive growth

Short-term time-lapse microscopy of nuclear DNA using the H2B-EGFP label confirmed not only nuclear movement in collective strands but also concurrent mitotic activity (Fig. 17, dashed boxes; Fig. 19a). Mitotic frequency amounted during tumor progression to 0 to 6 % of all nuclei, corresponding to values determined in cells migrating in 3D collagen matrices *in vitro* (data not shown) and in the main mass. Strikingly, mitotic planes were

preferentially oriented perpendicular to the invasion direction as detected from the angle distribution (Figs. 17, 19; see also Movie 3), suggesting that cells remain coupled in their orientation during collective invasion.

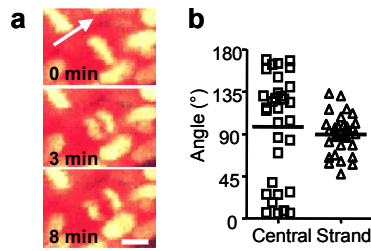


Figure 19. Mitotic activity in collective strands. (a) Segregation of chromosomes from time-lapse sequence of H2B-EGFP obtained from the box in (Fig. 17). Arrow, direction of invasion. Bar, 10 μm . (b) Angle distribution of mitotic planes relative to the invasion direction in collective invasion strands and the adjacent main tumor mass. Horizontal line, median.

To test whether cell proliferation contributes to cell strand protrusion efficiency, tumor growth and mitotic activity were arrested by low-dose fractionated irradiation (Figs. 20a, 43; irradiation protocol) and thereby uncoupled from the migration activity (Figs. 20b-g). Despite mitotic arrest (Figs. 20d, e) collective invasion persisted for several days at velocities ranging from 50 to 120 $\mu\text{m}/\text{d}$ during the irradiation phase, until it slowed down after irradiation was terminated (Figs. 20f, g).

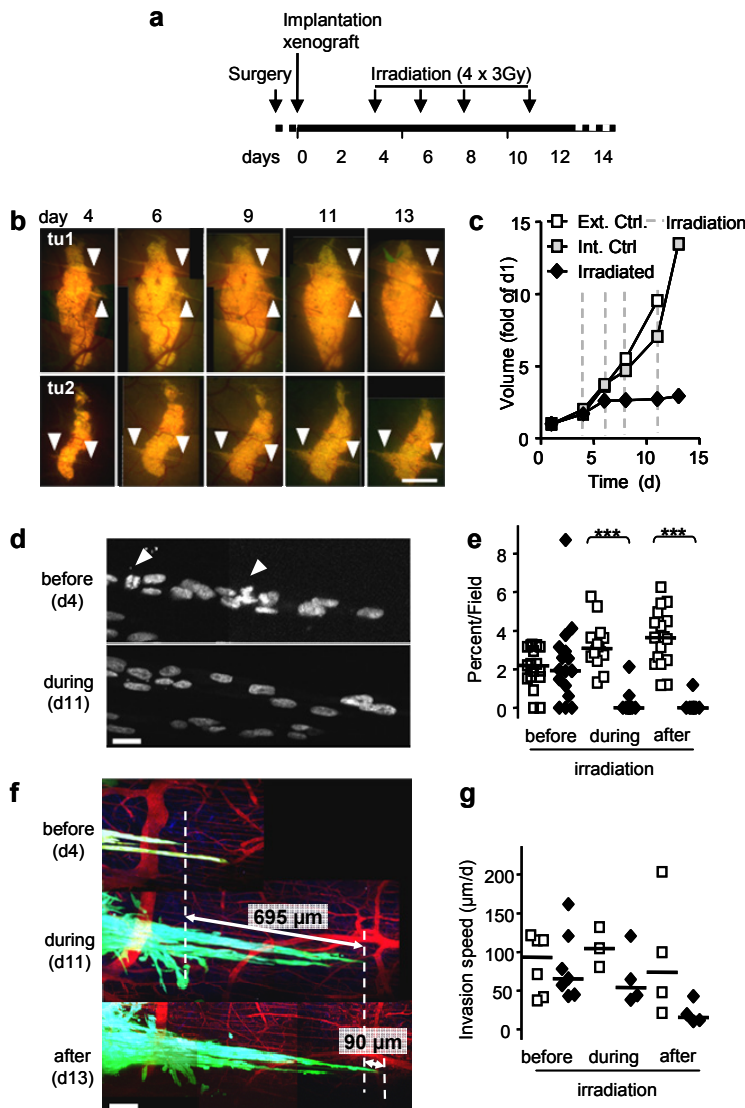


Figure 20. Uncoupling of mitotic activity from collective invasion. (a) Time scale and dosing overview for anti-proliferative, fractionated low-dosis irradiation of HT-1080 xenografts (cumulative dose 12 Gy). (b) Growth arrest in 2 xenografts during (d4 to 11) and after (d11-13) irradiation. Day 6 to 13 show ongoing collective invasion (arrowheads) despite stable tumor volume after d6. (c) Arrested growth in irradiated lesions, compared to untreated separate mice (external control) or a non-irradiated contralateral xenograft in the same mouse (internal control). Dashed lines, time points of irradiation (4 x 3 Gy). Data show the means \pm SD for 2 to 9 independent lesions. (d) Loss of mitotic figures (arrowheads) before and during irradiation detected from H2B-EGFP label of tumor nuclei. (e) Mitotic activity before, during and after irradiation quantified from independent fields of view. (f) Progressing invasion despite mitotic arrest. Collapsed MPM stacks (1100 nm excitation). The number indicates invasion distance of the upper collective strand during and after irradiation. (g) Invasion speed of individual collective strands determined before, during and after irradiation. (e,g) Horizontal line, median. *** $p < 0.001$ (unpaired Mann-Whitney U-test). Bars, 1 mm (b), 25 μm (d), 100 μm (f).

Thus, HT-1080 fibrosarcoma xenografts generate a predominant collective invasion pattern together with ongoing mitotic activity; whereas the invasion process occurs independently of cell division, proliferation is a supporting factor mid-term, possibly by aiding volume expansion or supporting cell polarity.

3.3.4 Collective invasion in human fibrosarcoma

The histomorphological characteristics of the 3D spheroid injection model, in particular the topology of invasion, were validated using human lesions of the classical fibrosarcoma type (Fig. 21).

Human fibrosarcoma invaded the adjacent stroma as multicellular strands with sharp boundary to the reactive connective tissue (monitored by α -smooth muscle actin positive fibroblasts) (Fig. 21a). Collective strands oriented along regular-shaped, erythrocyte-containing blood vessels with peripheral pericytes which frequently were located inside the invasion strands (Fig. 21b). Lastly, mitotic planes in human fibrosarcoma were oriented in perpendicular direction to strand extension (compare Fig. 17, dashed squares; Fig. 21c).

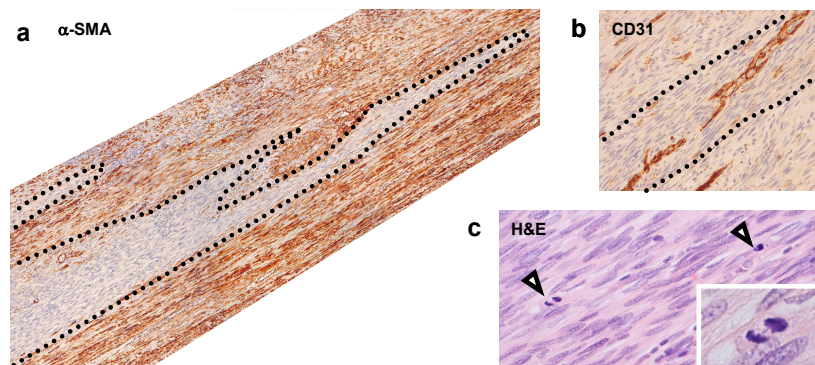


Figure 21. Collective invasion pattern in human adult fibrosarcoma (primary lesion in subdiaphragmal location). (a) Multicellular elongated strand bordered by reactive α -smooth muscle actin (SMA) positive stroma (b) along regularly-shaped CD31-positive preexisting vessels. (c) Mitotic figures perpendicular to strand orientation. Arrowheads, mitotic cells.

Thus, collective invasion along regular perfused blood vessels and concurrent mitotic activity are hallmarks of invasive growth in both orthotopic mouse model and human fibrosarcoma lesions.

3.4 Growth and invasion of orthotopic melanoma models

To establish a second, independent invasion model in the skinfold chamber, growth and invasion of melanoma allo- and xenografts were established and compared to fibrosarcoma invasion. Murine B16/F10 and human MV3 melanoma cells were used as dual-color variant (cytoplasmic DsRed2, H2B-EGFP) and injected into the dermis as described for HT-1080 cells (Fig. 8).

3.4.1 Growth of orthotopic melanoma lesions

B16/F10 and MV3 cells grew with different efficiency; B16/F10 tumors developed exponential growth at doubling rates of 1-2 days (Figs. 22a, b), whereas MV3 xenografts showed a near-linear growth with a doubling time of 6-10 days (Figs. 22c, d).

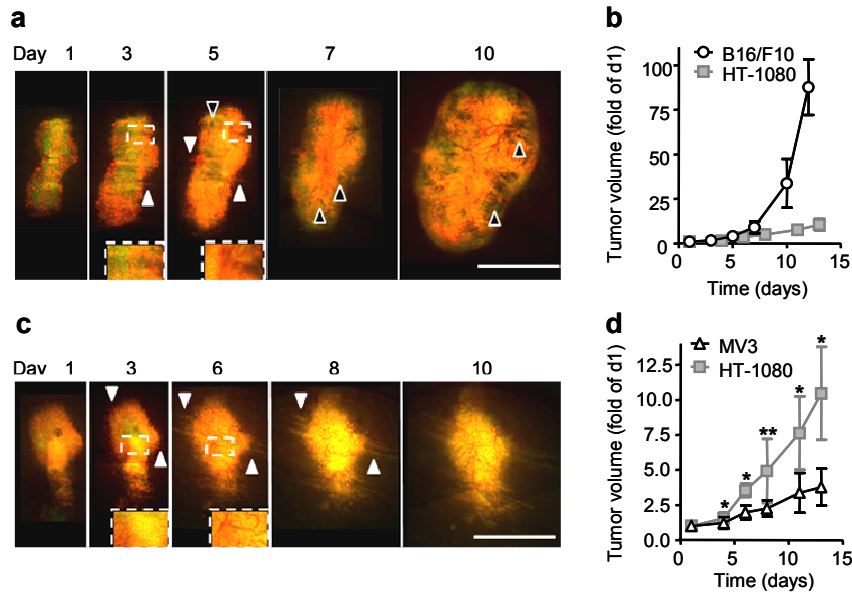


Figure 22. Melanoma growth after implantation into the mouse dermis. (a,c) Time-course of B16/F10 (a) and MV3 (c) xenograft growth and invasion (white arrowheads) monitored by epifluorescence microscopy. Insets, absence (day 3) and presence (B16/F10: day 5, MV3: day 6) of neovessels. Generation of melanin (black arrowheads). Bars, 1 mm. (b,d) Tumor volume growth of B16/F10 (b) and MV3 (d) tumors compared to HT-1080 and normalized to the volume of day 1. Mean values \pm SD (n = 4-9). * p<0.05 ** p<0.01 (unpaired Mann-Whitney U-test).

To better understand these differences in growth, the mitotic and apoptotic frequencies were compared (Fig. 23a). Both melanoma cell lines showed significantly more cell divisions than the HT-1080 cells, but no significant differences in apoptosis (Fig. 23a). Although MV3 divide 2-fold more often, xenografts grew slower (Fig. 22d). To explain this discrepancy the net survival was calculated for all cell lines (average mitotic frequency divided by average apoptosis rate; Fig. 23b). The mitosis/apoptosis index (MAI) was 6.5 in B16/F10, consistent with rapid tumor growth (Fig. 22b) and 2.3 for MV3 and HT-1080 lesions, consistent with moderate volume expansion of the lesion (Fig. 22d).

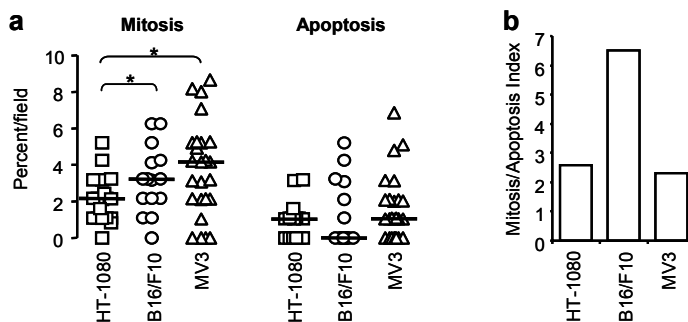


Figure 23. Mitosis and apoptosis in tumor main masses of HT-1080, B16/F10 and MV3 grafts. (a) Quantification of mitotic and apoptotic frequencies (HT-1080, MV3: day 6; B16/F10: day 3). Data show mean proportions of independent microscopic fields from 2 to 4 independent tumors. (b) Net survival (Mitosis/Apoptosis Index).

3.4.2 Pigment-induced phototoxicity in B16/F10 lesions – limitations for multiphoton microscopy

Although B16/F10 cells are amelanotic in cell culture *in vitro*, xenografts produced melanin starting at day 5 (Fig. 22a).

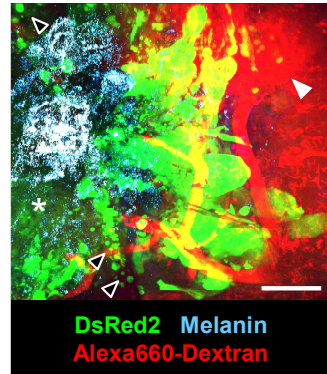


Figure 24. Tissue destruction (loss of cytoplasmic DsRed2 signal, asterisk; fragmented tumor cells, black arrowheads; leaky vessels, white arrowheads) caused by absorption of laser light. MPM reconstruction, excitation wavelength 1100 nm. Bar, 100 μ m.

Melanin absorbs UV light with maximum efficiency as well as, at lower efficiency, NIR and IR wavelengths²¹⁵, which in turn results in the generation of heat and thereby skin damage²¹⁶. Consistent with a previous report²¹⁶ repeated exposure of B16/F10 allografts to NIR irradiation required for *in vivo* microscopy (power range 75 - 125 mW) led to focal necrosis in the main tumor mass (Fig. 24) and associated vessel damage detected by leakage of Alexa 660 dextran (Fig. 24, white arrowhead). In addition, tumor cells became fragmented in regions of photodamage (Fig. 24, black arrowheads), and cytoplasmic DsRed2 signal was lost (Fig. 24, asterisk). In contrast to the main mass collective invasion strands were free of melanin probably due to the lower cell amount (Fig. 22a). Consequently, B16/F10 lesions may be amenable to early monitoring in non-pigmented state and/or single time-point measurements during pigmentation, not however for repetitive imaging required for longitudinal analysis of tumor progression and regression used in this study.

In contrast MV3 tumors produced no melanin up to day 14 which allows MPM to follow tumor development also at late stages (Fig. 22c).

3.4.3. Invasion pattern

After intradermal injection, B16/F10 and MV3 melanoma lesions showed invasion patterns similar to the HT-1080 model. The majority of cells invaded collectively retaining direct cell-cell contacts (Fig. 25). Likewise, individual B16/F10 and MV3 strands oriented along preexisting blood vessels of the deep dermis (Figs. 25c, f; white arrowheads). A considerable proportion of MV3 and B16/F10 collective strands was compact and contained one to 10 cell layers in width (Figs. 25b, e).

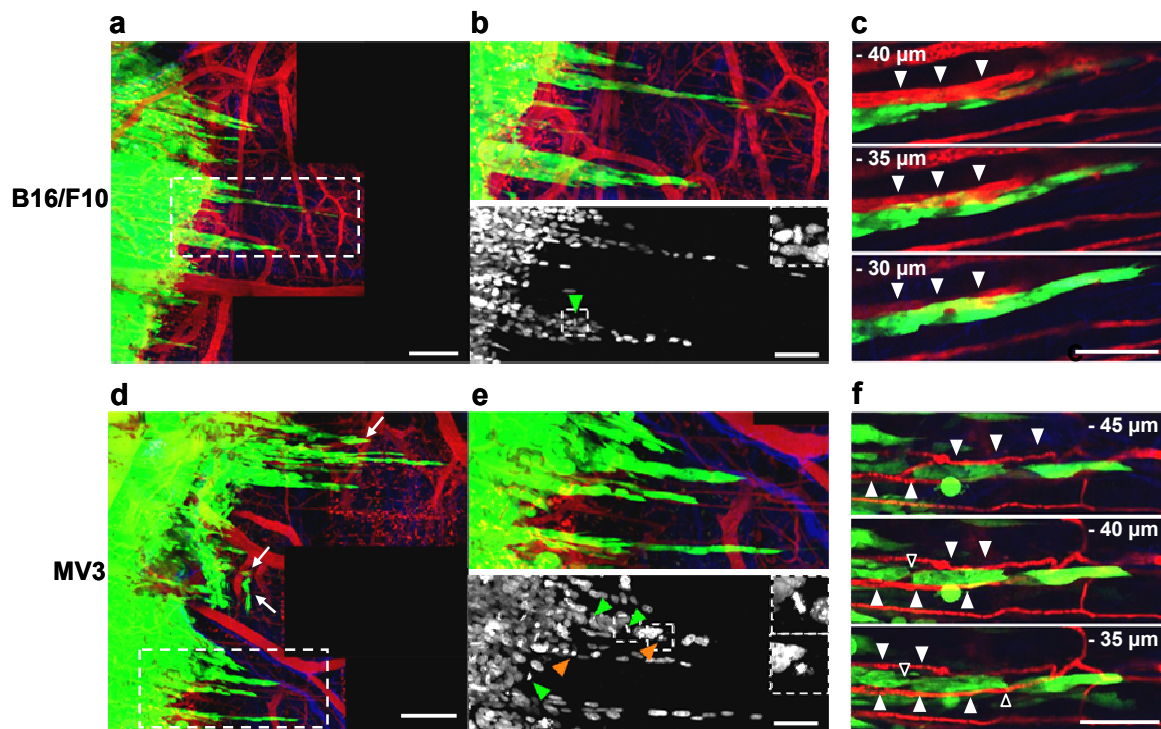


Figure 25. Collective melanoma invasion in skinfold chamber model. (a,d) Exemplary B16/F10 (a-c) and MV3 (d-f) tumor with mainly collective invasion areas. 3D reconstructions using MPM excitation at 1100 nm (B16/F10, d5; MV3, d11). Arrows, detached cells. (b,e) Collective invasion strands. Magnified region from (a, d; squares). Upper row MPM excitation 1100 nm, lower row 832 nm. Green arrowheads, mitosis; orange arrowheads, apoptosis. Insets, exemplary mitotic and apoptotic figures. (c,f) Guidance of collective invasion strands by perfused blood vessels (white arrowheads) in B16/F10 (c) and MV3 (f) tumors. Images are single focal planes with imaging depth indicated. Black arrowheads, loose cell-cell contacts via filopods. (a) – (h) 1100 nm: Tumor cytoplasm (green), Blood vessels and macrophages (red), Collagen (blue). 832 nm: Tumor nuclei (white). Bars, 250 μm (a, d) and 100 μm .

Whereas HT-1080 and B16/F10 lesions developed predominantly compact collective invasion yet limited single-cell dissemination, invasion areas of MV3 xenografts contained a spectrum of invasion patterns, including besides compact invasion strands, chains of multiple cells migrating in more loose collectives with tip-to-tip interactions (Fig. 25f, black arrowheads), as well as the migration of detached cell clusters or individual cells (Fig. 25d, white arrows). In loose chains, cell-cell contacts lacked continuous contact planes between each other but rather maintained filopods (black arrowheads; Figs. 18f, h), which is reminiscent of neural crest migration²⁴. Thus, B16/F10 grafts represent mainly a model for compact collective invasion of limited use for sequential multiphoton imaging, whereas MV3 lesions represent a model for the study of natural variability of cancer invasion, including collective invasion, multicellular streaming as well as single-cell dissemination.

3.4.4 Invasive growth of melanoma

HT-1080, B16/F10 and MV3 cells all invaded collectively into the same microenvironment, but their invasion speed varied substantially (Fig. 26a). Whereas MV3 cells invaded as efficiently as HT-1080 cells ($\sim 100 \mu\text{m}/\text{d}$; Fig. 26a), B16/F10 were by 50% slower ($40 \mu\text{m}/\text{day}$; Fig. 26a). The migration speed of MV3 cells is 3- to 5-fold slower than single-cell speeds obtained from 3D collagen lattices (data not shown) which is comparable to the reduction in velocity of HT-1080 cells. In contrast B16/F10 cells invaded collectively faster as as single cells *in vitro* (data not shown) indicating optimal migration conditions *in vivo*.

Similar to HT-1080 cells, collectively invading melanoma strands contained both mitotic and apoptotic figures (Figs. 25b, e, respective green and orange arrowheads). HT-1080 and MV3 invasion strands showed similar mitotic frequencies which were 2- to 3-fold higher compared to B16/F10 strands (Fig. 26b) whereas apoptotic rates were similar in HT-1080 and B16/F10 strands and 2-fold increased in MV3 strands (Fig. 26b). As consequence of these differences of mitosis and apoptosis rates, the net growth in invasion strands derived from the MAI was highest in HT-1080 cells and lowest in MV3 cells (Fig. 26c). Because MV3 cell strands were as fast as HT-1080 strands, these data indicate that collective invasion may comprise an active, migration driven and a passive, proliferation-driven component both of which differ between MV3 and HT-1080 cells. In B16/F10 strands, the comparably slow invasion speed is consistent with the decreased MAI in invasion strands compared to HT-1080 cells (Fig. 26c).

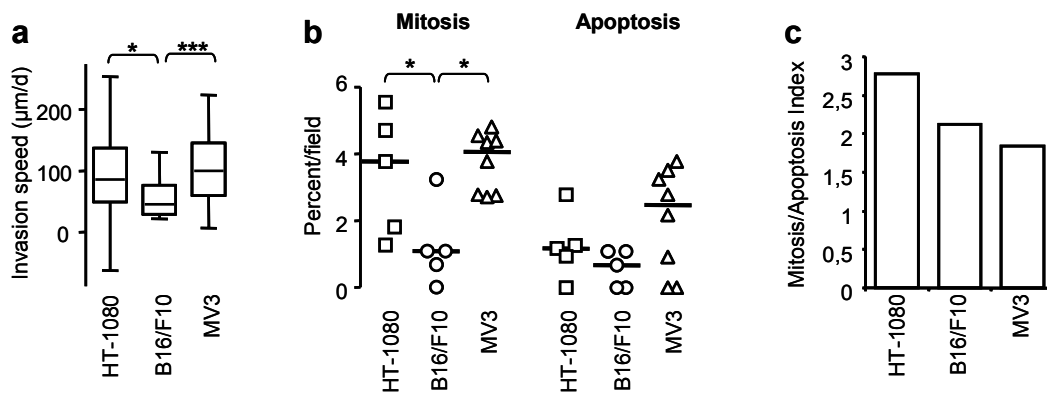


Figure 26. Speed, mitosis and apoptosis in invading collective melanoma strands. (a) Speed of individual collective strands. Median, 25th and 75th percentile (box) and 5th / 95th percentiles (whiskers; 17 to 45 strands). (b) Frequency of mitosis and apoptosis in invasion strands of B16/F10 and MV3 compared to HT-1080 tumors (HT-1080, MV3: day 6; B16/F10: day 3 (earlier time point because of accelerated progression of B16/F10 lesions)). Data points represent independent microscopic fields from 2-4 independent tumors. Line, median. (c) Net-survival as mitosis/apoptosis index. * $p < 0.05$, *** $p < 0.001$ (unpaired Mann-Whitney U-test).

3.5 Collective invasion: a radioresistance niche

3.5.1 Radiation therapy: Heterogeneity of response

In fibrosarcoma and other soft tissue sarcomas, standard post-surgery treatment is achieved by irradiation of the wound bed and adjacent healthy tissue, leading to greatly decreased rates of local tumor relapse¹⁸². The nearby location of invasion strands to blood vessels suggestive of high oxygenation and nutrient delivery^{217,218}; consequently, we hypothesized that collective invasion strands represent a region of particular radiosensitivity.

3.5.1.1 Heterogenous response rate to irradiation

To test the radiosensitivity of HT-1080 fibrosarcoma xenografts, established tumors including progressive invasion and neoangiogenesis were irradiated fractionally with 5 x 4 Gy (Figs. 27a, 43, radiation protocol).

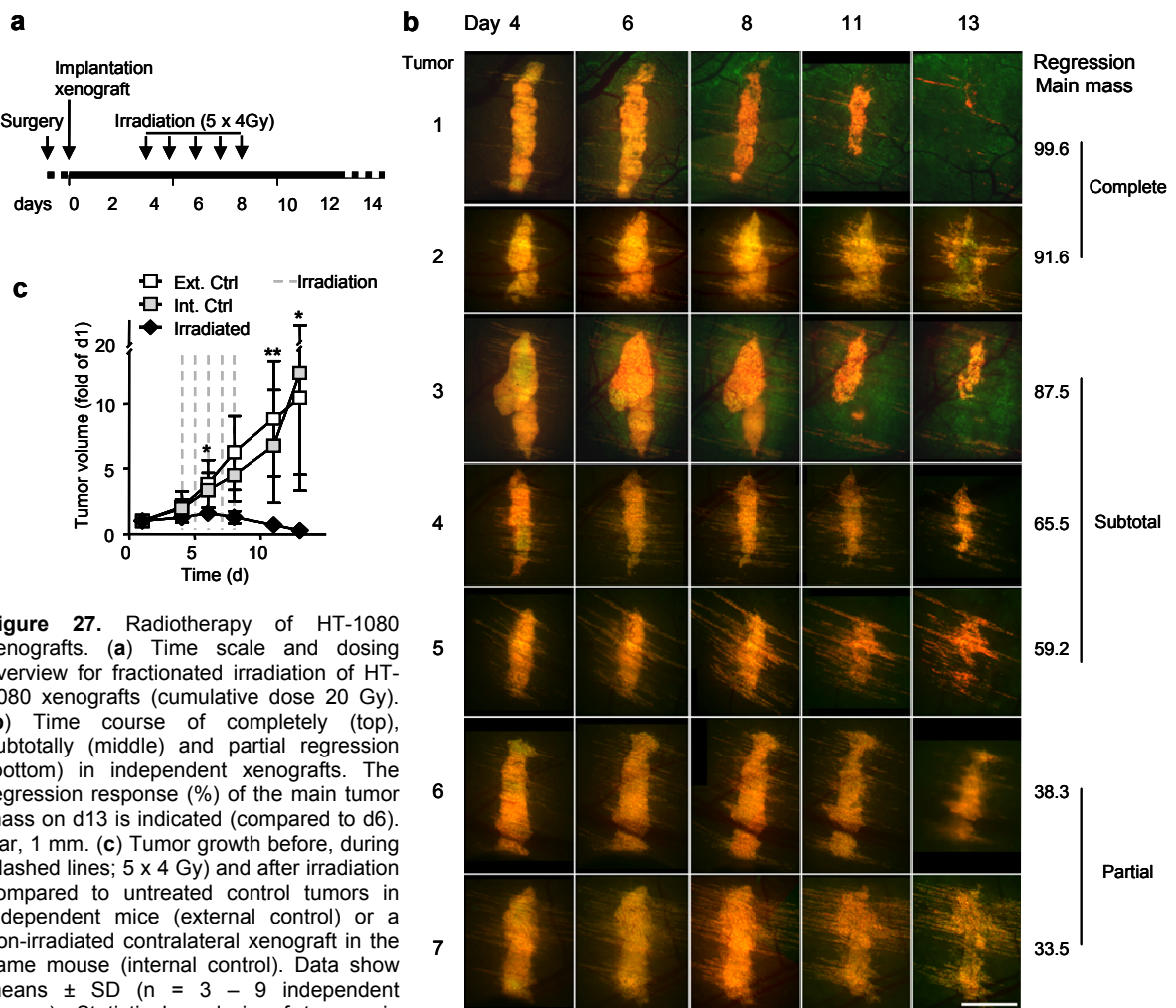


Figure 27. Radiotherapy of HT-1080 xenografts. (a) Time scale and dosing overview for fractionated irradiation of HT-1080 xenografts (cumulative dose 20 Gy). (b) Time course of completely (top), subtotally (middle) and partial regression (bottom) in independent xenografts. The regression response (%) of the main tumor mass on d13 is indicated (compared to d6). Bar, 1 mm. (c) Tumor growth before, during (dashed lines; 5 x 4 Gy) and after irradiation compared to untreated control tumors in independent mice (external control) or a non-irradiated contralateral xenograft in the same mouse (internal control). Data show means \pm SD (n = 3 – 9 independent tumors). Statistical analysis of tumors in independent mice (Ext. Ctrl.) vs. irradiated lesions. * p<0.05, ** p<0.01 (unpaired Mann-Whitney U-test).

This regimen resulted in partial to complete regression ranging from 33.5% (partial regression) to 100% (complete regression; Fig. 27b). Thus, although the same source cell and irradiation regimen was used, tumors could be grouped into high (>50% regression) and low responders (<50%), thereby mimicking the natural variability of response rates after treatment in patients. In high responders reduction of tumor volume started 1 to 3 days after the onset of irradiation, whereas in low responders a phase of persistence was followed by slow regression, usually after irradiation was completed (day 11; Fig. 27b). In most lesions growth slowed down significantly after 2 irradiation cycles (cumulative 8 Gy) and tumors regressed to 30% of the initial volume (Fig. 27c). Thus, albeit at variable time course and magnitude, the irradiation scheme led reproducibly to regression of the main mass of HT-1080 xenografts.

3.5.1.2 Heterogeneity between mitosis and apoptosis

To investigate the underlying mechanisms we determined irradiation response at the nuclear level and the time course of mitotic and apoptotic frequencies of the tumor mass was quantified. Two hours after the first irradiation, proliferation was significantly reduced or even ablated in some lesions (Figs. 28a). After 3 irradiation cycles (cumulative 12 Gy) proliferation was blocked completely in all tumors (Fig. 28a). In contrast, the apoptotic rate remained near-constant immediately after first irradiation (Fig. 28a). During the following days apoptosis rates increased slowly and finally doubled with a peak 168 h after the onset of irradiation (Figs. 28a). Thus, cell damage induced by radiotherapy first prevents cell division probably by cell cycle arrest to allow damage repair²¹⁹, and leads delayed to cell death²¹⁸.

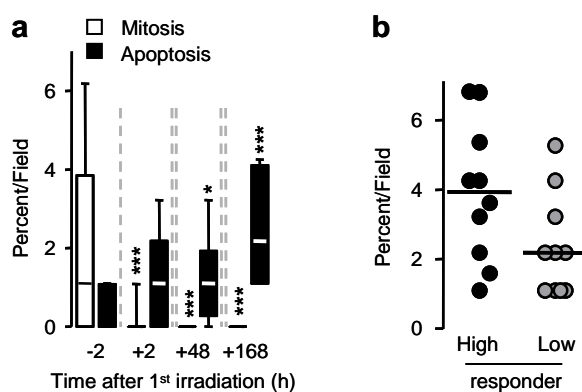


Figure 28. Impact of radiation therapy on mitosis and apoptosis rates in the main tumor mass. **(a)** Rapid proliferation arrest 2h after first irradiation whereas apoptosis rates remained constant (> 48 h and 5 irradiations). Time course of mitotic (white) and apoptotic fractions (black). Data show mitotic and apoptotic fraction of 20 independent fields of view from 3 – 4 independent lesions; median, 25th and 75th percentile (box) and 5th / 95th percentiles. Grey dashed lines, irradiation. Statistical comparison: time points after 1st irradiation vs. initial fraction 2h before irradiation. **(b)** Reduced apoptotic response of high vs. low-responding tumors after completed irradiation (d11 and 13). Horizontal line, median. * $p < 0.05$, *** $p < 0.001$ (unpaired Mann-Whitney U-test).

Differentiation of high and low responders showed that positive outcome was associated with higher apoptosis frequency compared to poor responders (Fig. 28b), whereas proliferation was completely arrested in all tumors and hence not predictive (data not shown).

3.5.1.3 Heterogeneity between main mass and invasion strands

It is known that microenvironmental factors like the oxidative status or factors secreted by stromal cells have significant impact on the sensitivity or resistance of cancer cells to therapy^{182,218,220}. 3D whole-field reconstructions before, during and after irradiation showed that incipient collective invasion was first insensitive and later partially sensitive to therapeutic irradiation during growth arrest phase (Fig. 29a; see also Movie 4). Although the average invasion speed slowed down dramatically and strands even retracted during regression phase (Fig. 29b), 30% of the strands were forward protruding several days after irradiation was completed (Fig. 29c).

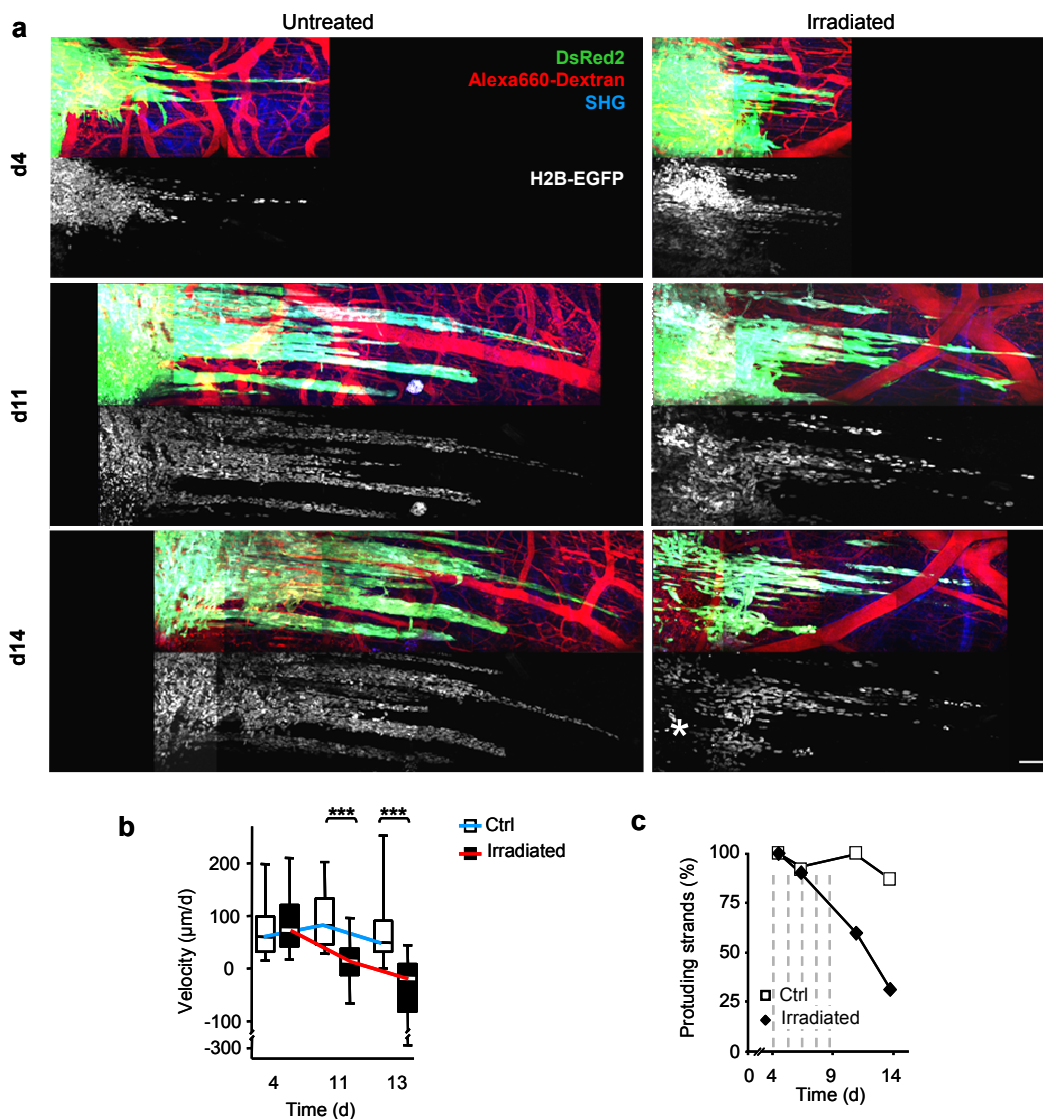


Figure 29. Relative radioresistance of collective invasion strands. (a) Time course of collective invasion efficiency before (d4), during (d11) and after (d14) irradiation compared to untreated control sample. Z-stacks of 120 to 250 µm depth were obtained by 1100 nm excitation and displayed as projections of tumor cytoplasm (DsRed2, green), blood vessels (Alexa Fluor 660-dextran, red) and SHG (blue; top images). A subsequent scan was obtained using 832 nm excitation for detecting H2B-EGFP expressing nuclei (white signal, bottom images). White asterisks, regression of main mass in irradiated tumor. (b) Time-dependent invasion speed of untreated and irradiated strands. Median, 25th and 75th percentile (box) and 5th / 95th percentiles (whiskers; 17 to 45 strands). (c) Fraction of actively protruding strands in control and irradiated tumors as mean value from 20-60 measured strands of 3 independent tumors. Dashed lines, time-points of irradiation. Bar, 100 µm. *** p < 0.001 (unpaired Mann-Whitney U-Test).

The kinetics of mitotic and apoptotic frequencies were assessed to monitor radiation sensitivity of collective strands relative to the central tumor mass. The mitotic arrest was uniform in main mass and invasion strands alike and persisted during and after irradiation was completed (Figs. 30a, b). In contrast, apoptotic rates in the main mass increased in average by 2-fold whereas only marginal increases were obtained in the invasion strands (Figs. 30a, c).

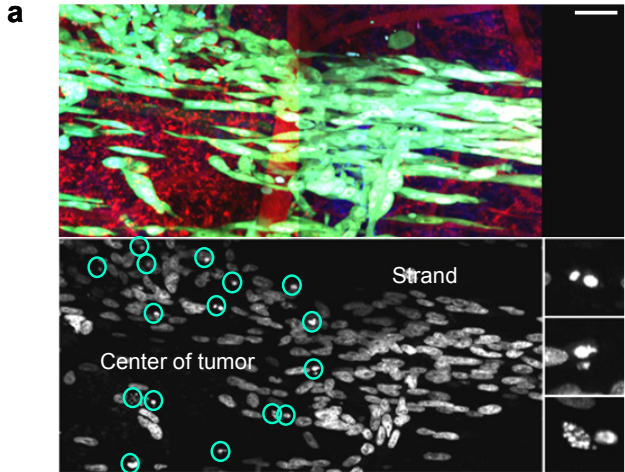
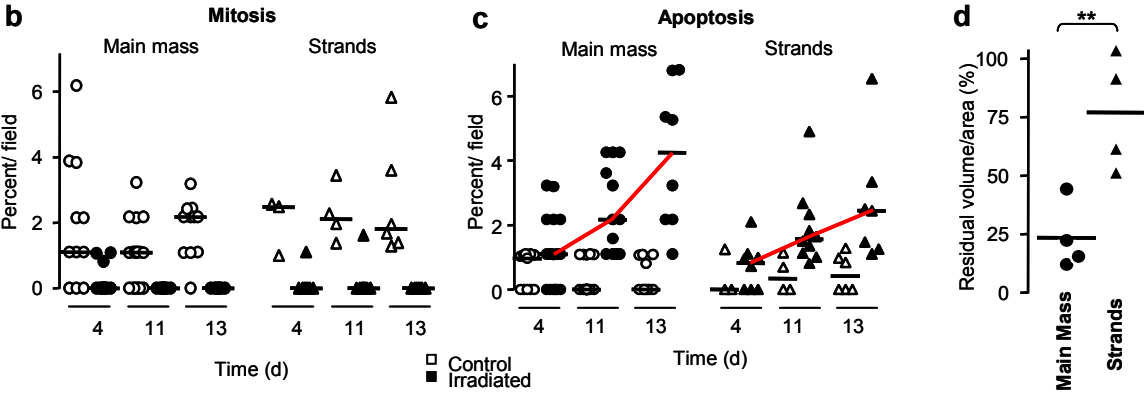


Figure 30. Relative resistance to radiation-induced apoptosis in invasion strands but not in main tumor mass. (a) Images show detail of (Fig. 29, d14). Circles, apoptotic nuclei. Insets, exemplary apoptotic nuclei. Bar, 50 μ m. Frequency of mitotic (b) and apoptotic figures (c) in main mass and collective invasion strands. Data show the fraction from different microscopic fields representing 3-4 irradiated tumors. Line, median. (d) Residual tumor volume (main mass) and residual tumor area (invasion) after completed irradiation (d13) compared to d6. 4 representative and fully analyzable tumors (high- and low-responders). Line, median. ** $p < 0.01$; *** $p < 0.001$ (Paired T-Test).



To quantify the regression of the invasion area, 2D images were reconstructed from z-stacks and the invasion areas were obtained by segmentation and pixel count (Fig. 31). First, tumor appearance at day 6 (maximum invasion area) was reconstructed and a mask for the tumor main mass area was created. Dependent on the vessel alignment this mask was applied to the tumor reconstruction of day 13 (end-point of experiment) and used to subtract the former area of the main mass. Afterwards the invasion area was determined to calculate the absolute and relative regression.

Consistent with incomplete apoptotic response in invasion strands, their response to irradiation was significantly less pronounced compared to the main tumor mass (Fig. 30d). Consequently, even in completely regressing main lesions collective invasion strands persisted in a morphologically intact and viable state, including non-fragmented interphase nuclei and non-compromised DsRed2 containing cytoplasm.

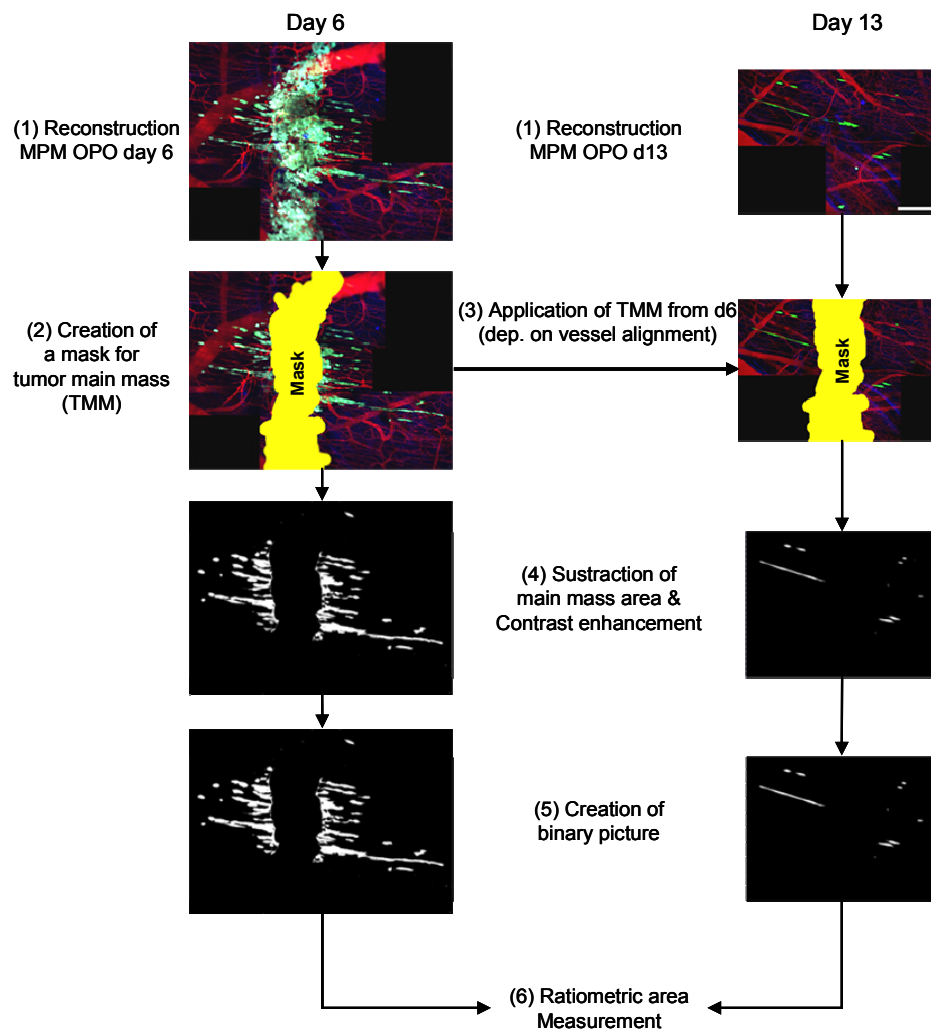


Figure 31. Quantification of the residual tumor area in invasion strands after irradiation. The area measured at d6 was set as 100 %, the area at d13 was used as residual tumor area. Bar, 250 μ m.

3.5.2 Radioresistance of human melanoma (MV3)

To confirm the altered biology, i.e. radioresistance of collective invasion strands in a different tumor model, human MV3 melanoma cells were implanted into the DSFC and irradiated. In pilot experiments, cumulative irradiation doses of 20 or 50 Gy, respectively, led to growth arrest but lacked regression or only partial, not however complete regression of the main mass (Fig. 43, irradiation protocols). High resolution MPM imaging of irradiated lesions revealed that either proliferation was not blocked (20 Gy) or after completed irradiation mitotic activity was switched on again (50 Gy; data not shown). A modified protocol of increased efficiency was used to avoid a restart of mitosis after completion of irradiation (Fig. 32a) and further prevent skin damage which was otherwise obtained using doses higher than 50 Gy (data not shown). This modified protocol resulted in growth arrest followed by partial regression of the tumor main mass (Figs. 32b, c). Topographic quantification of relative regression rates revealed that collective invasion strands, again, showed a trend to regress less efficiently, compared to

the tumor mass (average 20% less; Figs. 32b, d) due a significantly weaker induction of apoptosis (Fig. 32f). As in the HT-1080 model proliferation was arrested completely in both, main mass and strands (Fig. 32e).

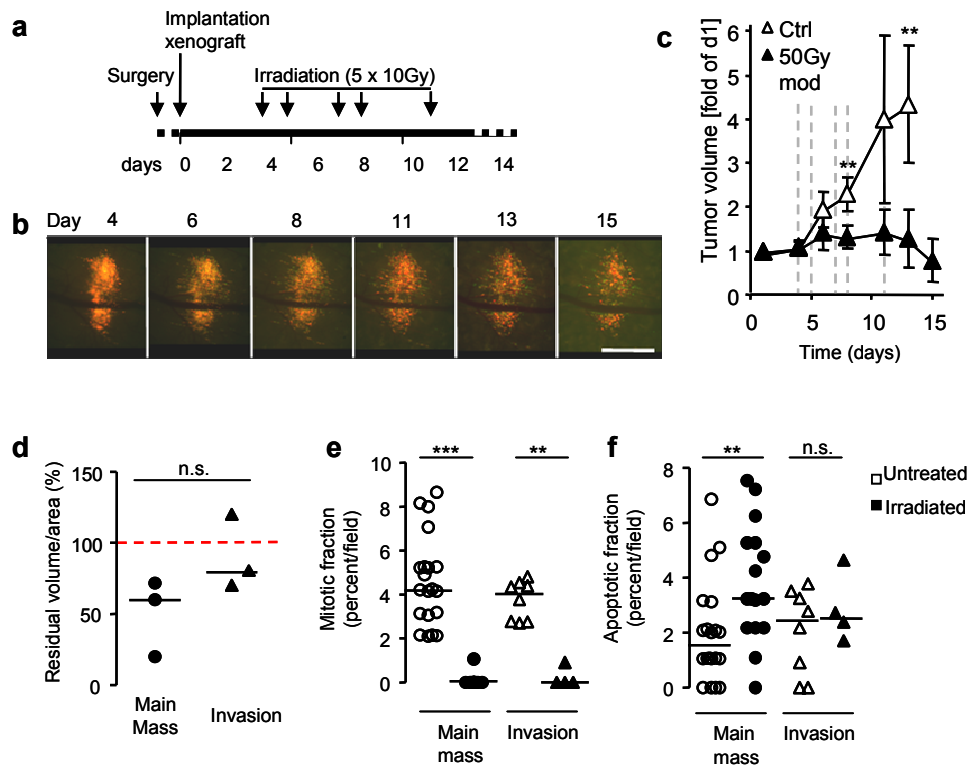


Figure 32. Relative radioresistance of invasion strands and disseminated single cells in MV3 tumors. (a) Time scale and dosing overview for modified fractionated irradiation of MV3 xenografts (cumulative dose 50 Gy). (b) Time course of irradiation response and partial regression after application of modified irradiation protocol (a). Bar, 1 mm. (c) Tumor volume before, during (dashed lines; 5 x 10 Gy) and after irradiation compared to untreated control tumors in independent mice. Data show the means \pm SD (n = 4 - 7 independent tumors). (d) Residual tumor volume (main mass) and residual tumor area (invasion) after completed irradiation (d15) compared to d6). Data points represent the combined values of bilateral invasion zones from 3 independent lesions. Line, median. Paired t-test. (e) Mitotic and (f) apoptotic fraction of untreated and irradiated cells on d6. Main mass compared to invading cells. Data points represent the percentages from multiple independent microscopic regions per lesion from 3 independent tumors. Line, median. ** p < 0.01; *** p < 0.001 (Unpaired Mann-Whitney U-Test).

These findings, in part confirm a decreased radiosensitivity in collective invasion strands in MV3 melanoma lesions, which are a model of high radioresistance similar to clinical experience with melanoma in humans²²¹.

3.6 Molecular mechanisms of collective invasion and radioresistance

3.6.1 Radioresistance despite chemotherapy (doxorubicin)

Doxorubicin belongs to the group of alkylating agents which are cytostatica that prevent DNA replication by binding to nucleic acids thereby leading to cell cycle arrest similar to irradiation. In addition to surgical tumor resection and irradiation, doxorubicin is a most effective chemotherapeutic agent (25% of patients respond) in treatment of advanced soft tissue sarcoma in adults¹⁸².

We therefore determined whether doxorubicin, either alone or in combination with irradiation, had an impact on the persistence of both, main tumor mass and/or collective strands in mice bearing established HT-1080 tumors (Fig. 43, medication protocol).

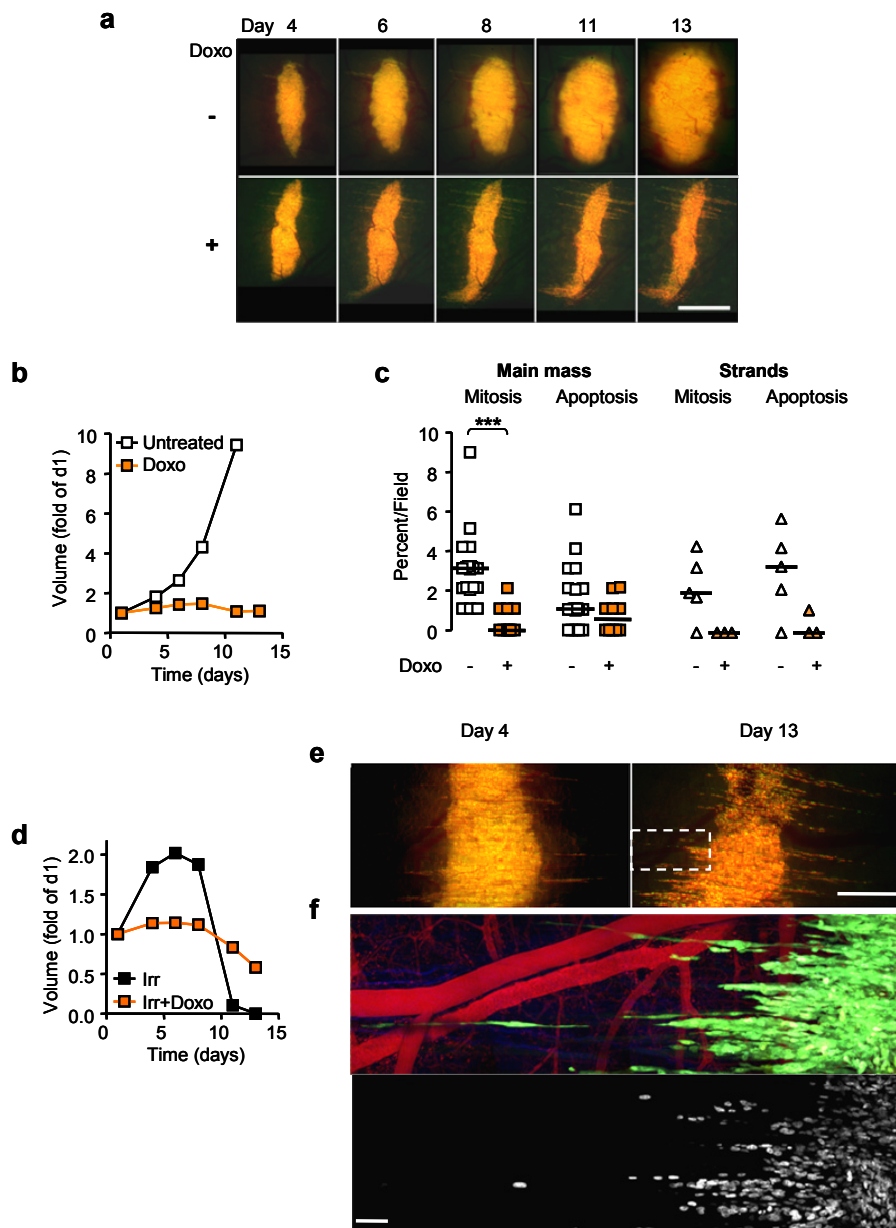


Figure 33. Response of HT-1080 xenografts to systemic chemotherapy with doxorubicin. (a) Time course of growth and invasion of HT-1080 xenograft during and after treatment with doxorubicin (Doxo; lower row) in comparison to untreated control tumor (upper row). White arrowheads, collective invasion strands. (b) Time course of tumor volume in the presence (orange) or absence (white) of doxorubicin treatment. Mean values from 2 to 4 independent tumors. (c) Mitotic and apoptotic fractions of independent visual fields from 2 to 4 independent tumors. Left, tumor main mass. Right, invasion strands. Line, median. (d) Lack of radiosensitization by doxorubicin. Growth response and regression of tumors during and after radiotherapy in absence (black) or presence (orange) of doxorubicin. Mean of 2 to 4 independent tumors. (e) Radioresistance of tumor main mass and collective strands was increased by treatment with doxorubicin. Epifluorescence images before (left) and after (right) radiotherapy. (f) Viable collective invasion strands after irradiation and doxorubicin treatment (detail from (e), dashed box). Z-projections of MPM 3D stacks (120 to 160 μm depth) using 1100 nm excitation. Cytoplasm of tumor cells (DsRed2, green), blood vessels (Alexa Fluor 660-dextran, red) and SHG (blue; top images). A subsequent scan using 832 nm excitation shows tumor nuclei (H2B-EGFP, white) detection (bottom). Bars, 1mm (a), 250 μm (e) and 100 μm (f). *** $p < 0.001$ (unpaired Mann-Whitney U-test).

As maximum cumulative dose of doxorubicin, 9 μg per g body weight were used since higher doses led to the onset of therapy-induced lethality 5 to 7 days after first injection

(data not shown). Treatment of xenografts with doxorubicin alone resulted in growth arrest of the tumor main mass (Figs. 33a, b) due to strongly decreased mitotic and a constant apoptotic rate (Fig. 33c) consistent with effects of the expected cell cycle arrest. Compared with the main mass proliferation was equally well inhibited in collective invasion strands (Fig. 33c) but spontaneous apoptosis was ablated. Similar to irradiation, chemotherapy with doxorubicin neither prevented the onset nor reduced the progression of collective invasion strands (Fig. 33a, white arrowheads).

If combined with irradiation, administration of doxorubicin had no additional effect on the radiation response of the main mass and rather blunted its efficacy compared to single-modality radiotherapy (Fig. 33d). This could be caused by the induced partial cell cycle arrest prior to irradiation that reduces tumor growth and thereby also vulnerability towards irradiation. Moreover, as in irradiated control tumors, viable strands were observed after irradiation was completed (Figs. 33e, f) excluding a radiosensitizing effect of doxorubicin on invasion strands. Thus, although doxorubicin induces *per se* growth arrest of HT-1080 xenografts, it showed no additional efficacy on radiation therapy.

3.6.2 Epidermal growth factor

EGF is known to guide collective invasion of border cells in the *Drosophila* egg²²²; inhibiting EGF receptor (EGFR) signaling has further been shown to increase radiosensitivity in head and neck cancer²²³. *In vitro*, HT-1080 cells express EGFR and show phosphorylation in response to EGF signaling²²⁴.

To test whether EGF signaling contributes to collective invasion of fibrosarcoma lesions and further address its role in radioresistance of invasion strands, the antibody cetuximab which blunts EGFR signaling was injected into mice bearing HT-1080 xenografts and combined to irradiation applying dosing regimen comparable to successful studies on squamous cell carcinoma²²³ (Fig. 43, application protocol).

Although cetuximab led to reduced mitosis in the tumor main mass (day 11) net tumor growth was not inhibited (Figs. 34a-c). Further, cetuximab neither inhibited the onset nor progression of collective invasion despite the application of repeated doses (Fig. 34a, white arrowheads).

Combined application of irradiation with cetuximab (before, during and after completed irradiation) showed no increased regression of main mass or invasion strands, compared to in parallel irradiated control tumors (Figs. 34d, e), which resulted in viable invasion strands after irradiation (Fig. 34f).

Thus, EGF plays no auxiliary role in collective invasion of HT-1080 xenografts and EGF receptor inhibition cannot prevent radioresistance.

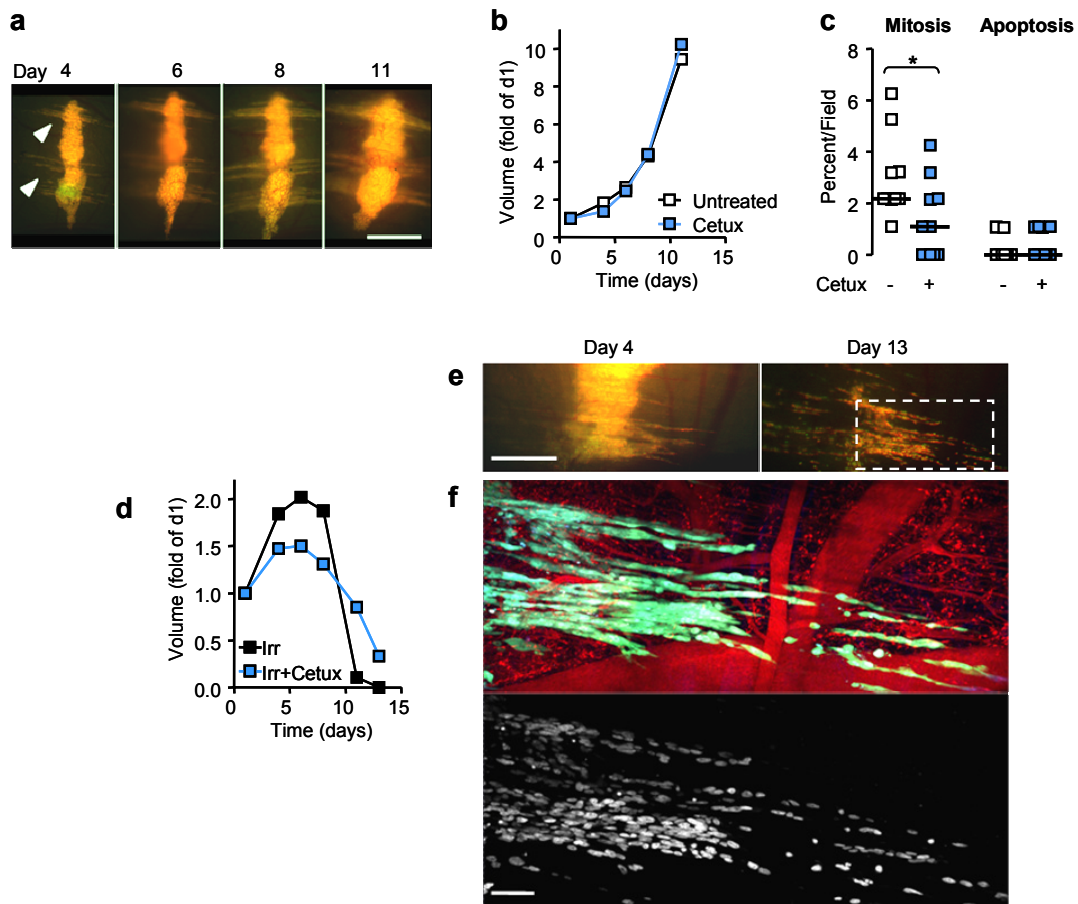


Figure 34. Contribution of EGF signaling on HT-1080 tumor growth and invasion. (a) Time course of growth and invasion of HT-1080 tumor during treatment with Cetuximab (Cetux, EGFR blocking antibody). White arrowheads, collective strands. (b) Time course of tumor volume with (blue) and without (white) Cetuximab treatment. Mean of 2 to 4 independent tumors. (c) Mitotic (left) and apoptotic fractions (right) of independent visual fields from 2 to 4 independent tumors on d11. Fields located in tumor main mass. Line, median. (d) Unchanged regression of tumors during and after radiotherapy in absence (black) or presence (blue) of Cetuximab. Mean of 2 to 4 independent tumors. (e) Persisting radioresistance of collective invasion strands despite Cetuximab treatment. Epifluorescence before (left) and after (right) radiotherapy. (f) Viable collective strands after irradiation. MPM detail of d13 (e, dashed box). 3D stacks (120 to 160 μm in depth) were obtained by 1100 nm excitation and reconstructed. Tumor cell cytoplasm (DsRed2, green), blood vessels (Alexa Fluor 660-dextran, red) and SHG (blue; top images). A subsequent scan using excitation at 832 nm was used to detect tumor cell nuclei (H2B-EGFP, white). Bars, 1 mm (a), 250 μm (e) and 100 μm (f). * $p < 0.05$, *** $p < 0.001$ (unpaired Mann-Whitney U-test).

3.6.3 Integrins

The $\beta 1$ integrin subfamily plays a central role in tumor cell migration^{7,225} as well as in tumor growth and survival by providing costimulatory signaling to input from growth factor receptors¹¹³. Functional blockade of $\beta 1$ integrin *in vitro* strongly reduces single cell migration of HT-1080 and MV3 cells or collective migration from melanoma explants in 3D collagen lattices^{7,8,52} and might be therefore efficient to block invasive migration and/or growth in xenografts *in vivo*. In addition, $\beta 1$ integrin has been shown to increase the radiosensitivity of a breast cancer xenografts in mice²²⁶. Therefore we tested whether interference with $\beta 1$ integrin enhances radiosensitivity in the main tumor mass, collective invasion strands, or both.

3.6.3.1 Establishment of stable knockdown cell lines

3.6.3.1.1 Knock down of $\beta 1$ integrin

As initial approach, stable knockdown of $\beta 1$ integrin expression by lentiviral vectors encoding a short hairpin RNA (shRNA) directed against *ITGB1* in HT-1080 cells was used to test the role of $\beta 1$ integrin on tumor cells *in vivo* while avoiding interference towards the host microenvironment. Four different sequences were tested and the clone with highest knock down efficiency (80%, clone 2) was selected for further experiments (Figs. 35a, b).

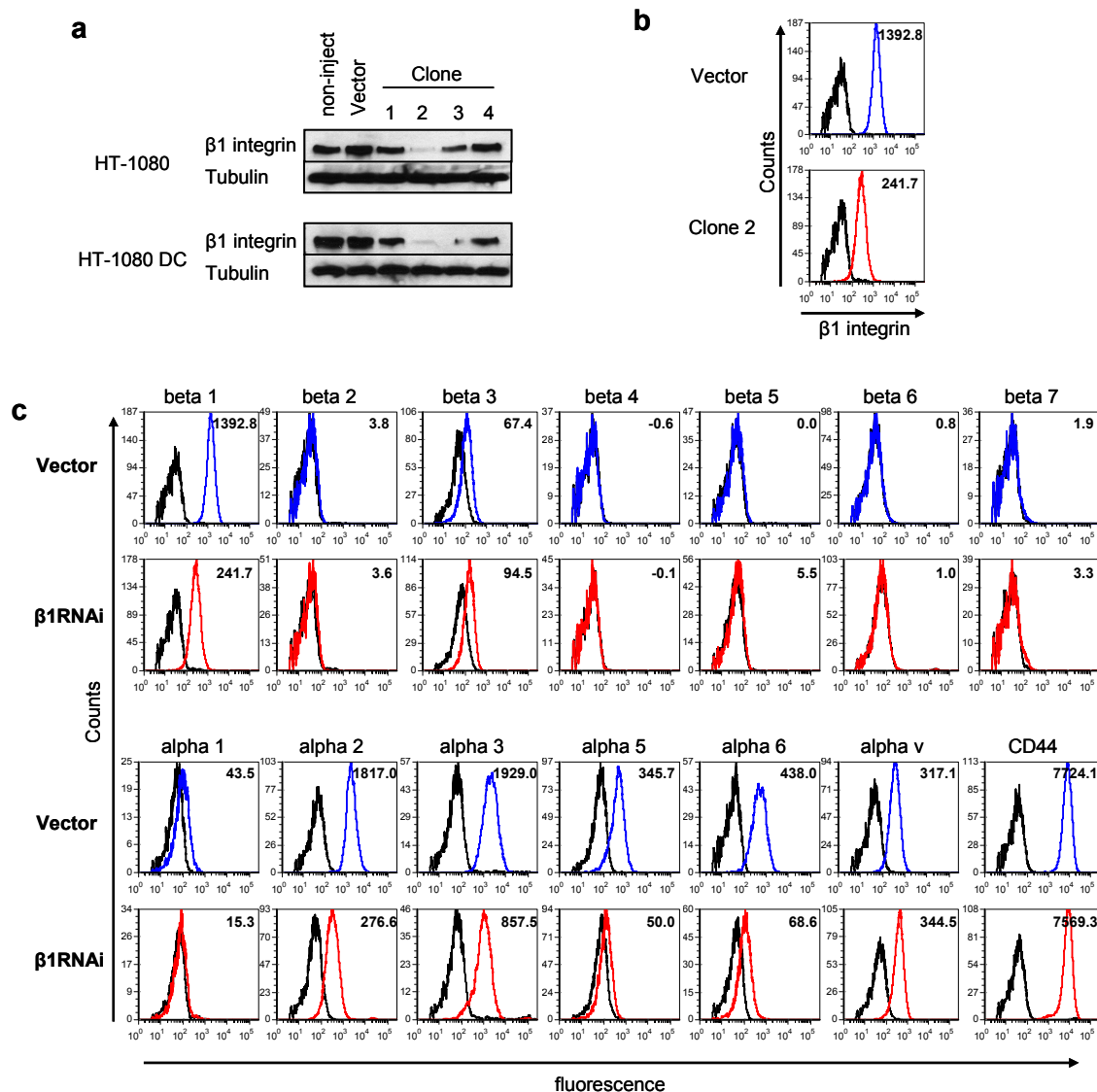


Figure 35. Stable lentiviral shRNA knockdown of $\beta 1$ integrin. **(a)** Knockdown efficiency of 4 different shRNA probes against $\beta 1$ integrin detected by Western Blot in HT-1080 and dual-color HT-1080 (DC) cells. As control wild-type and with empty vector (p-puro) transfected cells were used. β -tubulin was used as loading control. **(b)** Knockdown efficiency of surface $\beta 1$ integrin on shRNA clone 2 assessed by flow cytometry. **(c)** Surface expression profile of known integrin β and α chains as well as CD44 on HT-1080 p-puro (vector control) and HT-1080/ $\beta 1$ kd ($\beta 1$ RNAi clone 2). **(b, c)** To mimic ligand-induced regulation states, integrins were measured on cells after 24 h incubation in 3D collagen lattices after retrieval using collagenase digestion. Isotypic control (black line), antibody signal (blue line – vector, red line - $\beta 1$ RNAi). Numbers indicate relative integrin fluorescence intensity minus isotype value.

To address whether other integrin chains were up- or downregulated as consequence of $\beta 1$ integrin knockdown the surface expression profile of all integrin chains was obtained by flow cytometry. Besides $\beta 1$, only $\beta 3$ integrin was weakly expressed on the surface of HT-1080 cells (Fig. 35c, vector control), whereas none of the other integrin β -chains were either present constitutively or upregulated after $\beta 1$ integrin knockdown (Fig. 35c). The knockdown of $\beta 1$ induced a mild upregulation of $\beta 3$ by 35% (Fig. 35c, $\beta 1$ RNAi), whereas all α chains potentially associated with $\beta 1$ were strongly downregulated ($\alpha 1$: 35%, $\alpha 2$: 15%, $\alpha 3$: 44%, $\alpha 5$: 15%, $\alpha 6$: 16%; Fig. 35c). As only exception, the αv chain which is the sole binding partner of $\beta 3$ was slightly upregulated (Fig. 35c).

3.6.3.1.2 Double knockdown of $\beta 1$ and $\beta 3$ integrin

Inhibition of $\alpha v\beta 3$ was shown to reduce cell migration of cervical tumor cells²²⁷ and radioresistance in melanoma, head and neck cancer, glioblastoma, and colon cancer cells by inhibiting angiogenesis²²⁸.

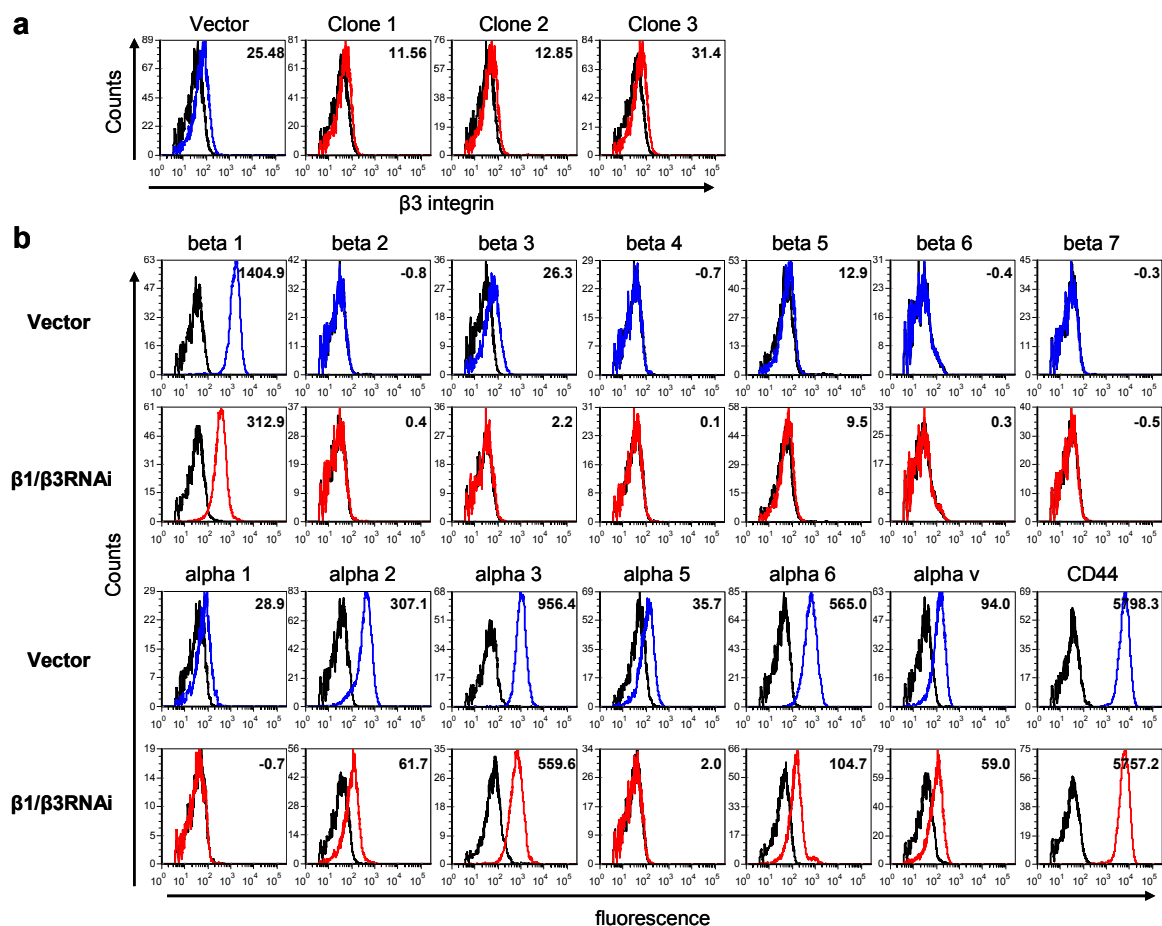


Figure 36. Stable lentiviral knockdown of $\beta 3$ integrin in combination with $\beta 1$ integrin knockdown. **(a)** Knockdown efficiency of 3 different shRNA probes against $\beta 3$ integrin assessed by flow cytometry in HT-1080 cells. As control cells transfected with empty vector (p-neo) were used. **(b)** Surface expression profile of known integrin β and α chains as well as CD44 on HT-1080 p-puro/p-neo (double vector control) and HT-1080/ $\beta 1/\beta 3$ kd ($\beta 1$ RNAi clone 2, $\beta 3$ RNAi clone 1). Upper row, integrin β chains. Lower row, integrin α chains and CD44. **(b, c)** To mimic ligand-induced regulation states, integrins were measured on cells after 24 h incubation in 3D collagen lattices after retrieval using collagenase digestion. Isotypic control (black line), antibody signal (blue line – vector, red line - $\beta 1$ RNAi). Numbers indicate relative integrin fluorescence intensity minus isotype value.

To control for potential compensation by $\beta 3$ integrin after knockdown of $\beta 1$, a second series of experiments aimed at double-interference against $\beta 1$ and $\beta 3$ integrins. Three $\beta 1/\beta 3$ double knock down cell lines using different shRNA clones were established, and the most effective shRNA sequence was selected for use in $\beta 1$ RNAi clone 2 (Fig. 36a). Whereas the αv chain was not affected in cells after $\beta 1$ knockdown alone, additional knockdown of the $\beta 3$ chain led to near-complete loss of $\beta 3$ and strong downregulation of the αv chain (60%; Fig. 36b).

3.6.3.2 *In vitro* characterization of $\beta 1$ RNAi and $\beta 1/\beta 3$ RNAi cells

The stability of integrin downregulation was tested by culturing HT-1080/ $\beta 1$ kd and HT-1080/ $\beta 1\beta 3$ kd cells in the absence of antibiotic selection pressure for 4 weeks. After this period antibiotics puromycin and/or neomycin were added again to the medium. The re-onset of selection caused no increased cell death compared to cells cultured continuously with antibiotics (data not shown), indicating that the HT-1080/ $\beta 1\beta 3$ kd cell line is stable even in the absence of selection pressure for at least 4 weeks, making these cells suitable for *in vivo* use.

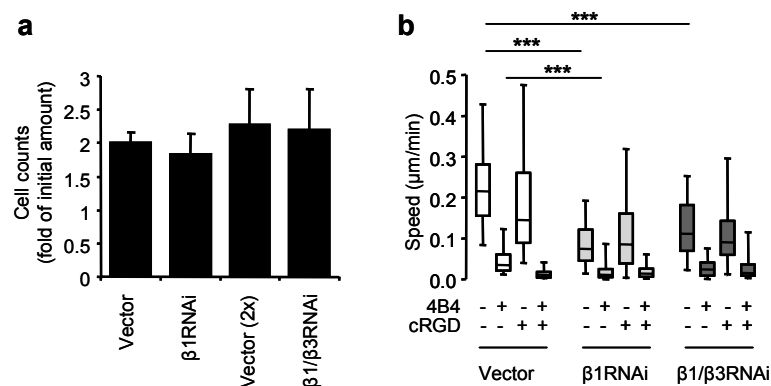


Figure 37. *In vitro* characterization of HT-1080 cells after stable knockdown of $\beta 1$ or $\beta 1$ and $\beta 3$. (a) Proliferation. Cell numbers after 48h in cell culture were obtained from HT-1080/ $\beta 1$ kd and $\beta 1/\beta 3$ kd cells as well as respective vector control cells (Vector, pLBM-puro; Vector (2x), pLBM-puro/pLBM-neo). Mean \pm SD of 3 independent samples. (b) Migration efficiency. HT-1080 cells were incorporated in 3D collagen lattices in the presence or absence of $\beta 1$ integrin blocking antibody (clone 4B4) or cRGD peptide for 24h. Migration velocities were obtained by single-cell tracking. Median, 25th and 75th percentile (box) and 5th / 95th percentiles (whiskers; 20 to 30 cells). *** $p < 0.001$ (unpaired Mann-Whitney U-test).

To characterize the phenotype of $\beta 1$ and $\beta 1/\beta 3$ knock down cells *in vitro* net survival was determined first. The same amount of HT-1080/ $\beta 1$ kd and HT-1080/ $\beta 1\beta 3$ kd cells or cells expressing control vector (pLBM-puro (single vector control) and pLBM-puro/pLBM-neo (dual-Vector control)) were cultured in standard liquid culture plates, and the cell numbers were counted after 48h of growth. Single- or dual-knockdown of $\beta 1$ and $\beta 3$ integrin had no effect on cell numbers compared to control vector (Fig. 37a). In contrast to growth, knockdown negatively impacted the migration of HT-1080 cells in 3D collagen lattices. $\beta 1$ RNAi reduced migration speed by 60% and no additional effect was achieved after $\beta 3$ knockdown (Fig. 37b). This subtotal inhibition was further enhanced by addition

of adhesion perturbing anti- β 1 integrin antibody (clone 4B4) reaching 80% reduction in speed in all cell lines, but not by additional blockade of RGD binding integrins (including α v integrins) using cyclic RGD peptide (Fig. 37b). Thus, HT-1080 cell migration in collagen lattices but not *in vitro* growth in culture plates was dependent upon β 1 integrin and no effect was noted for β 3 integrin. These *in vitro* data further suggest that the knockdown of β 1 integrin is incomplete; to reach maximum efficiency additional neutralization of residual integrin activity by blocking antibody is necessary, as determined by *in vitro* migration efficiency as read-out. The additional knockdown of β 3 integrin was not sufficient to decrease migration efficiency below values achieved by complete blockade of β 1 integrin function indicating a minor role for β 3 integrin *in vitro* migration.

3.6.3.3 Role of β 1 and β 3 integrin in tumor progression *in vivo*

To investigate the contribution of β 1 and β 3 integrin to tumor growth and collective invasion *in vivo* β 1 single and β 1/ β 3 dual integrin knockdown HT-1080 cells were implanted in to the deep mouse dermis of the skinfold chamber and monitored for 2 weeks.

3.6.3.3.1 Tumor growth

In contrast to control shRNA in combination with IgG₁ isotype treatment, knockdown of β 1 integrin resulted in by 70% decelerated tumor volume growth however failed to achieve growth arrest or regression of the lesion (Figs. 38a, b, d).

Additional administration of mAb 4B4 at 5 mg per kg body weight, which was the most effective dosage of comparable antibodies in previous studies²²⁹ (Fig. 43, administration protocol), induced tumor growth arrest with a tendency to regression of the tumor main mass (Figs. 38b, d). This growth defect was associated with both decreased mitotic and significantly increased apoptosis frequencies (Fig. 38e). With similar efficiency tumor growth was arrested by knocking down both β 1 and β 3 integrins (Figs. 38c, d). However, when 4B4 was additionally injected, tumors after β 1/ β 3 knockdown underwent spontaneous, complete regression (Figs. 32c, d) due to strongly increased apoptosis and partial mitosis arrest (Fig. 38e).

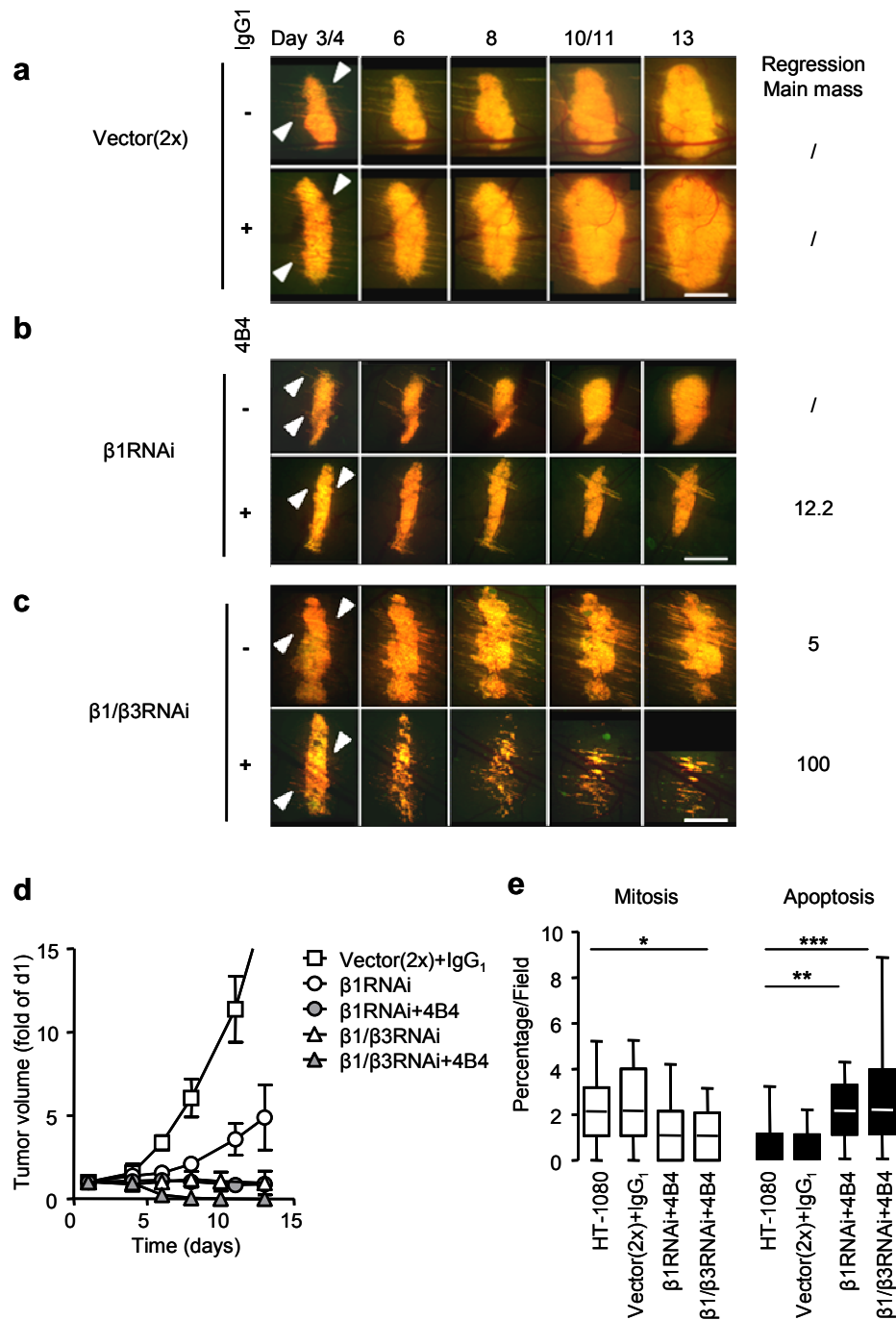


Figure 38. Contribution of $\beta 1$ and $\beta 3$ integrins to tumor growth and survival. **(a-c)** Time course of growth and invasion of **(a)** dual-vector control tumors without (1st row) and with IgG₁ isotype control treatment (2nd row) was compared to **(b)** $\beta 1$ RNAi and **(c)** $\beta 1/\beta 3$ RNAi tumors without (1st row) or with (2nd row) additional treatment with anti- $\beta 1$ integrin mAb 4B4. White arrowheads, collective invasion strands. Numbers in the right column indicate the mean regression (%) of the tumor main mass on d13 compared to day 6 (obtained from 3 to 4 independent tumors). Bars, 1 mm. **(d)** Time course of tumor volume of dual-vector control (IgG₁ isotype control treatment), $\beta 1$ RNAi and $\beta 1/\beta 3$ RNAi tumors with and without combinatorial treatment with $\beta 1$ integrin blocking antibody (clone 4B4). Mean \pm SD of 3 to 4 independent tumors. **(e)** Mitotic (left) and apoptotic fractions (right) displayed as the medians, 25th / 75th (box) and 5th / 95th percentiles (whiskers; 20 independent fields from fields located in tumor main mass). * $p < 0.05$, ** $p < 0.01$, *** $p < 0.005$ (unpaired Mann-Whitney U-

3.6.3.3.2 Role of $\beta 1$ and $\beta 3$ integrins in collective invasion

Although knockdown and blocking of $\beta 1$ and $\beta 3$ impair tumor growth dramatically suggesting that the approach efficiently interferes with integrin function, collective invasion was not prevented (Fig. 38b, c; white arrowheads; 39a).

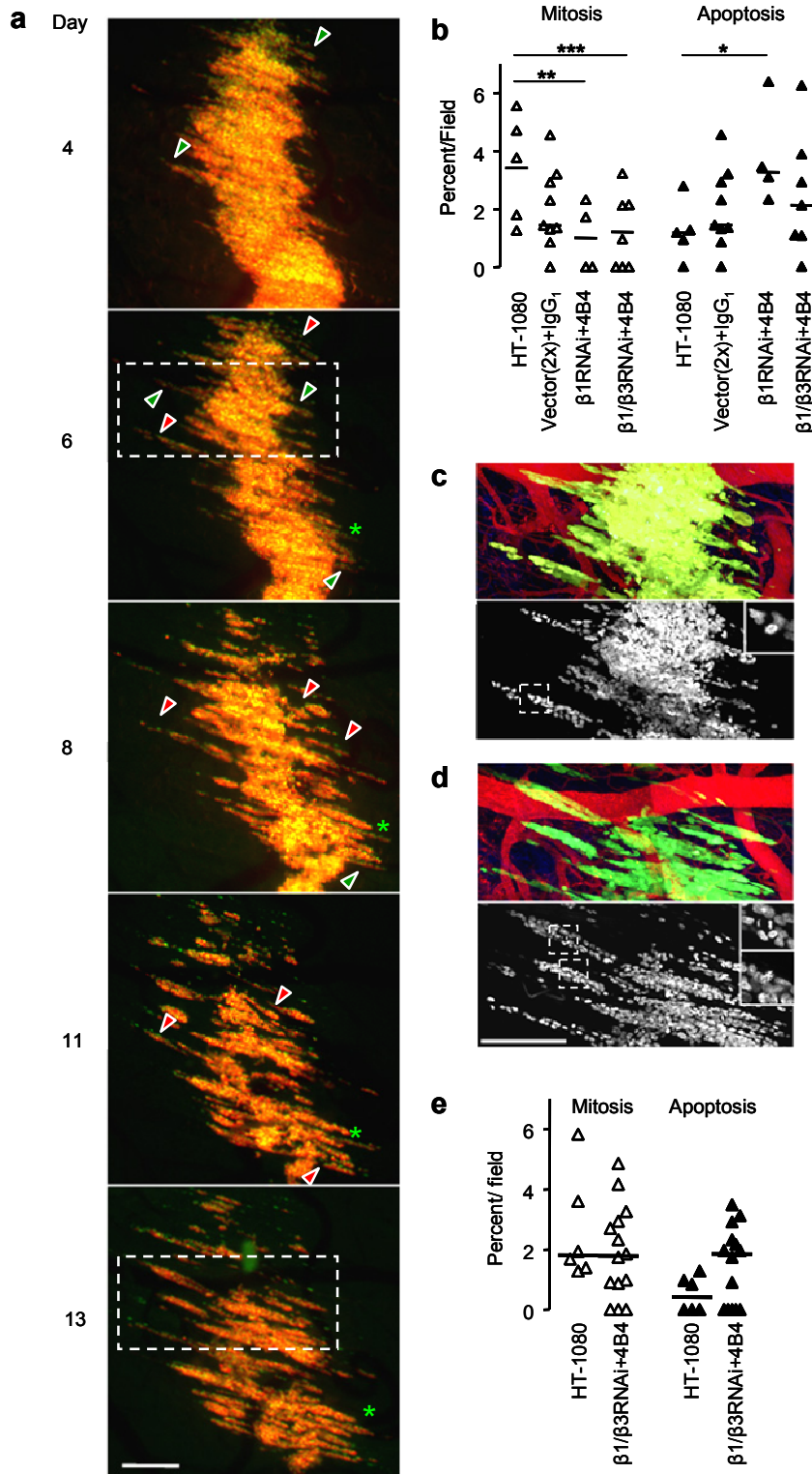


Figure 39. Contribution of $\beta 1$ and $\beta 3$ integrins to individual and collective invasion. (a) Early onset followed by decay of collective invasion of HT-1080/ $\beta 1/\beta 3$ kd xenograft treated with anti- $\beta 1$ integrin mAb 4B4. Green arrowheads, collective strands; red arrowheads, fragmented strands and clusters; green star, persisting collective strands throughout observation period. Occasional individual detached cells were observed to migrate independently of invasion strands. Boxes, region of MPM reconstructions in (c, d). (b, e) Mitotic (left) and apoptotic frequencies (right) in collective strands. Independent visual MPM fields from 3 to 4 independent tumors at d6 (b) and d13 (e). Line, median. (c, d). MPM z-projections at d6 (c) and d13 (d) of 120 μ m deep 3D stacks obtained by 1100 nm excitation for display of tumor cytoplasm (DsRed2, green), blood vessels (Alexa Fluor 660-dextran, red) and SHG (blue; top image) and a subsequent scan using 832 nm excitation for tumor nuclei (H2B-EGFP, white) detection (bottom). Insets, mitotic figures in collective cell clusters. Bars, 250 μ m. * p < 0.05, ** p < 0.01, *** p < 0.005 (unpaired Mann-Whitney U-test).

As in untreated control tumors, invasion after $\beta 1/\beta 3$ knock-down started 1 to 3 days after implantation and appeared mainly, but not exclusively as collective strands (Fig. 39a, green arrowheads). In contrast to controls some collective strands partially fragmented at various time points and locations (Fig. 39a, red arrowheads), whereas others remained intact during invasion progression (Fig. 39a, strand group marked with green star). In the time span from day 4 to 8, individual intact strands migrated with 30 to 86 μm per day, which was 50% slower compared to untreated control tumors (compare Fig. 18) and similar to invasion strands after mitosis-arrest, suggesting that the proliferation-enhancing rather than a direct promigratory integrin function was inhibited in this phase. Beyond day 8 no prolongation of strands could be detected (Fig. 39a) suggesting that maximum extension of strands was achieved and further migration could result in disruption of strands.

Mitotic and apoptotic frequencies in invasion strands from $\beta 1/\beta 3\text{kd}$ tumors were similar to those of the tumor main mass at day 6 (compare Fig. 38e and 39b); significantly reduced mitosis and increased apoptosis rate. Remarkably, on d13, after migration arrest and despite strand fragmentation and individualization of cells, the mitotic fraction increased minimally whereas the apoptosis decreased. This resulted in stabilization of the cell amount (compare d6 Figs. 39b, c to d13 Figs. 39d, e) so that after main mass regression was complete, only cells after invasion survived (Figs. 38a, 39a) and maintained low-level mitotic activity (Fig. 39e).

Thus, although the importance of $\beta 1$ and $\beta 3$ integrin for tumor cell migration is established in defined *in vitro* models, collective invasion *in vivo* occurs largely independent of $\beta 1$ and $\beta 3$ integrin function. Moreover, despite their contribution of cell survival in the main mass, the survival advantage of invasion strands was not substantially compromised even after combining $\beta 1$ and $\beta 3$ knockdown with blocking anti- $\beta 1$ integrin antibody. Taken together, the data suggest that *in vivo* alternative and/or compensatory mechanisms exist for invasion of as well as cell survival within collective strands in the invasive niche which diminish the role of $\beta 1$ and $\beta 3$ integrins established *in vitro*.

3.6.3.4 Prevention of radioresistance by $\beta 1$ and $\beta 3$ integrin knockdown

To test whether $\beta 1$ and $\beta 3$ integrin mediate radioresistance of collective invasion strands, HT-1080/ $\beta 1$ and $\beta 1/\beta 3\text{kd}$ xenografts were irradiated and additionally treated with mAb 4B4.

Dual-vector control xenografts showed no significant differences in basic growth and invasion parameters, therefore irradiation effects in knockdown xenografts were compared to HT-1080 wild-type dual-color xenografts. Compared to control tumors irradiation of tumors after $\beta 1$ and $\beta 1/\beta 3$ knock-down resulted in fast regression (Figs. 40,

compare Fig. 27b) starting after the first irradiation cycle (Fig. 40c). Given that $\beta 1$ and $\beta 3$ knock-down leads to tumor regression *per se* (Fig. 38c), irradiation caused an acceleration of the process (Fig. 40b, c). Moreover, three days after irradiation was completed the tumor main mass was eliminated in a very reproducible manner, which differed from the otherwise obvious tumor-to-tumor variability (compare Fig. 40b to 27b).

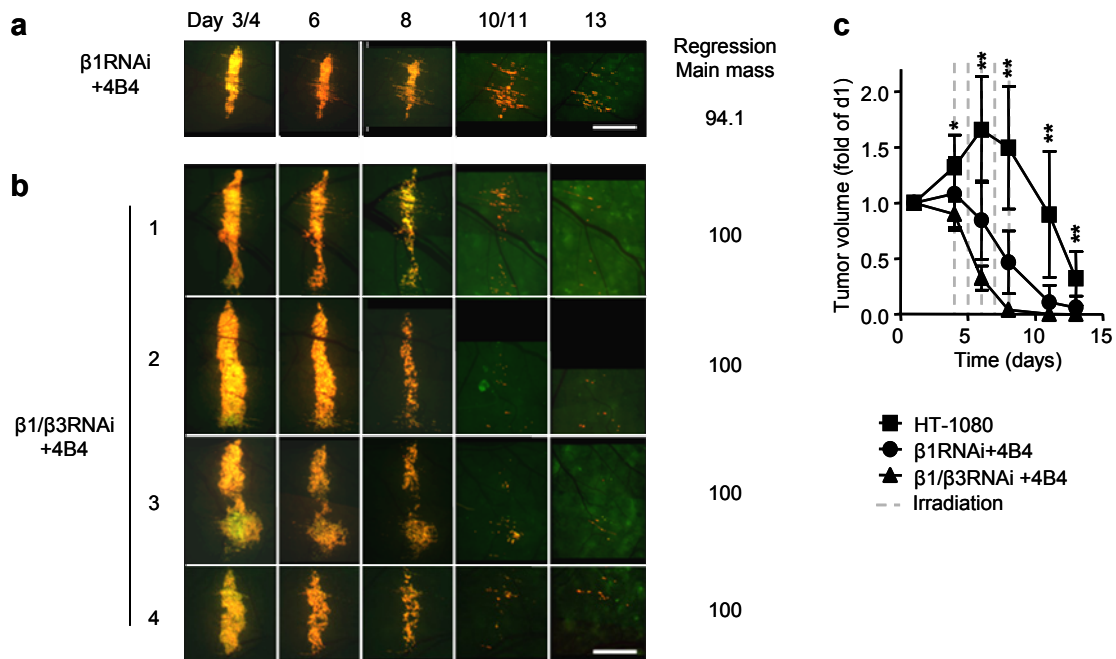


Figure 40. Irradiation-induced regression after interferences with $\beta 1$ and $\beta 3$ integrins. **(a,b)** Time course of regression of **(a)** $\beta 1$ RNAi and **(b)** $\beta 1/\beta 3$ RNAi tumors and additional 4B4 treatment during and after irradiation (5 x 4Gy). Numbers in the right column indicate the mean regression (%) of the tumor main mass on d13 compared to day 6 (obtained from 3 to 4 independent tumors). **(b)** Uniform response of tumors after $\beta 1/\beta 3$ RNAi treated with mAb 4B4. **(c)** Time course of tumor volume regression during and after irradiation treatment (5 x 4Gy) of HT-1080, $\beta 1$ RNAi and $\beta 1/\beta 3$ RNAi tumors treated with mAb 4B4. Means \pm SD of 3 to 4 independent tumors. Bars, 1 mm (a-c, e) and 250 μ m (e, details). Significance: HT-1080 vs. $\beta 1/\beta 3$ RNAi + 4B4; ** $p < 0.01$; *** $p < 0.001$ (unpaired Mann-Whitney U-test).

Despite interference with $\beta 1$ and $\beta 3$ integrins the initial collective invasion capability remained intact (Figs. 38b, c; 39). Also additional radiotherapy did not prevent formation of new collective strands neither in tumors after $\beta 1$ (Fig. 40a) nor $\beta 1/\beta 3$ knockdown (Figs. 40b; 41a, d6: green arrowhead). Whereas invasion was not altered, irradiation induced the regression (Fig. 40b; Fig. 41a, red arrowheads) and fragmentation of collective strands which resulted in enhanced individualization of tumor cells (Fig. 40b, Fig. 41a, yellow arrowheads). Knockdown of $\beta 3$ in addition to interference with $\beta 1$ integrin accelerated this process (compare Figs. 40a and 40b). Although irradiation could not further increase the apoptotic frequency in the main mass, it did so in invasion strands (Fig. 41c). As end-point, mainly individualized, residual individual cells of compromised survival ability and pygnotic, dying cells with residual nuclear EGFP-H2B signal were left behind (Figs. 41a: red arrowhead, individual cells; white star, pygnotic, dying cells; 41b).

Thus, irradiation combined with anti-integrin therapy led to the complete regression of the main tumor mass and an almost complete regression of invasion strands minimizing differences in radiosensitivity between main mass and invasion strands (Figs. 41b, d).

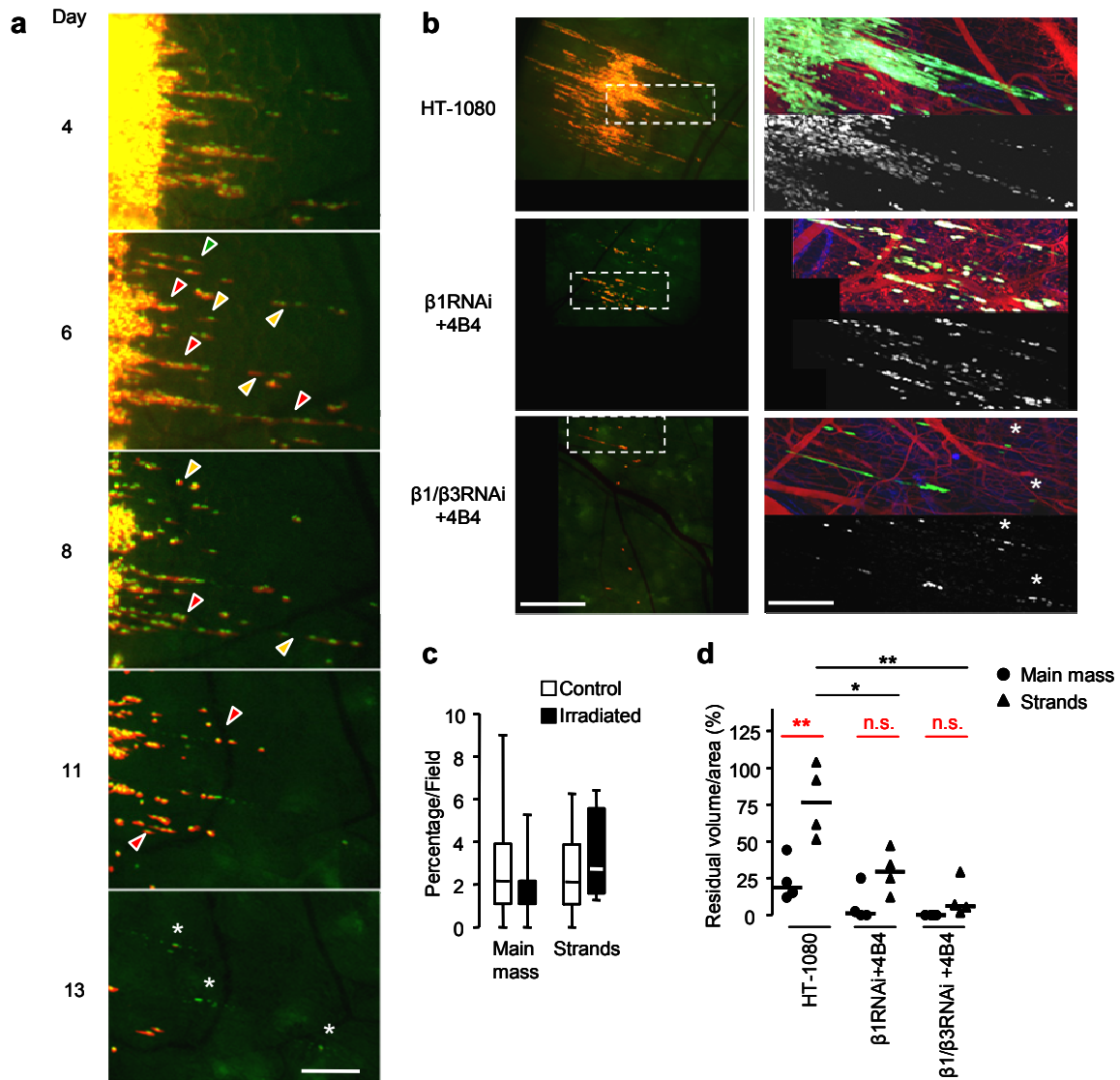


Figure 41. Increased radiosensitivity after interference with $\beta 1$ and $\beta 3$ integrins. **(a)** Time course of regression after $\beta 1/\beta 3$ knockdown and treatment with mAb 4B4 during and after irradiation (5 x 4Gy). Exemplary tumor, detail of Fig. 40b, 1st row. Green arrowhead, progressing invasion; red arrowheads, regressing invasion strands; yellow arrowheads, fragmented strands resulting in individualized tumor cells; white asterisks, pygnotic dying cells. **(b)** Comparison of residual tumor mass in HT-1080 tumors after $\beta 1$ RNAi and $\beta 1/\beta 3$ RNAi (incl. 4B4 treatment) compared to control tumors. Left, epifluorescence image of a representative tumor at d13. Dashed boxes, position of MPM imaging field. Right, MPM z-projections of 120 μ m deep 3D stacks obtained by 1100 nm excitation for display of tumor cytoplasm (DsRed2, green), blood vessels (Alexa Fluor 660-dextran, red) and SHG (blue; top image) and a subsequent scan using 832 nm excitation for tumor nuclei (H2B-EGFP, white) detection (bottom). White asterisks, pygnotic dying cells. **(c)** Apoptotic frequency in tumor main mass and collective strands at d6 in non-irradiated and irradiated tumors after $\beta 1/\beta 3$ RNA knockdown treated with mAb 4B4. Median, 25th / 75th (box) and 5th / 95th percentiles (whiskers; 4 to 20 independent fields). **(d)** Residual tumor volume (main mass) and residual tumor area (cells after invasion) after irradiation (d13) compared to d6. Line, median. Bars, 1 mm (b, overview) and 250 μ m (a; b, details). Significance highlighting the different response rate to irradiation between main mass and invasion strands (red asterisks; paired t-test) and between treatment conditions (black asterisks; unpaired Mann-Whitney U-test). * $p < 0.05$; ** $p < 0.01$.

Taken together, although collective invasion *in vivo* can occur independently of $\beta 1$ and $\beta 3$ integrin function, interference with these molecules is sufficient to compromise tumor growth and survival and break radioresistance of collective invasion strands.

4 DISCUSSION

This study provides novel tools for deep cell and tissue imaging using two-photon near-infrared (NIR) and infrared (IR) excitation and leads to refined orthotopic cancer models for fibrosarcoma and melanoma for direct visualization of tumor growth, invasion and response to therapy. The data show that cooption of preexisting vessels conveys collective invasion as well as a pro-survival niche during radiotherapy and pharmaceutical interference. Whereas invasion strands were resistant to any single-modality interference, multimodal therapy using irradiation combined with integrin blockade successfully interfered with this resistance niche.

4.1 Improved tissue penetration and imaging of red dyes using IR-MPM

Multiphoton microscopy (MPM) has emerged as a significant measurement method for intravital and live cell studies in neuroscience, immunology, and cancer research. Using NIR wavelengths the main advantage of MPM over other imaging approaches is its ability to observe cell migration, cell-cell interaction, and intracellular signaling deeply inside tissues and organs in live animals^{173-175,200}. In addition, MPM enables excitation of the characteristic UV absorption bands of endogenous fluorophores and SHG²⁰²⁻²⁰⁴. Since MPM is typically carried out using a Ti:Sa laser emitting light in the range of 680 to 1080 nm, fluorescent proteins in the blue to yellow are efficiently excited whereas red and NIR fluorophores are not without applying very high laser powers that provoke light-induced toxicity²⁰⁵. Moreover, penetration depth and spatial resolution decrease with increasing depth and optical density of tissues^{148,206-208}. Whereas with NIR excitation for lymph node imaging sufficient penetration is reached to image the T cell zone up to a depth of 200 μm from the lymph node cortex, the same excitation is insufficient to penetrate beyond the tumor surface, due to increased densities and light scattering by peritumoral tissue. By applying an optical parametric oscillator, improved excitation and detection conditions for fluorescent dyes were established and revealed that IR-MPM is superior to NIR-MPM for deep tumor imaging. IR-MPM-excited fluorescence and SHG imaging is suitable for non-toxic time-resolved reconstruction of cell behavior, particularly in deep tissue regions. As advantage compared to other pulsed femtosecond IR laser systems, including Cr:forsterite (1230 nm) and Fianium fiber (1064 nm) lasers, the wavelength generated by the OPO is tuneable and suited to accommodate red and NIR fluorophores at their excitation peak. Without a major compromise in resolution, the wavelength range of 1100 to 1200 nm is well suited for the excitation of red and NIR fluorophores like DsRed2 and AlexaFluor660, as well as for genetically encoded red-shifted fluorescent proteins and broad-band SHG. In addition it benefits from the restrictive water absorption of wavelength below 1300 nm²¹² and is therefore ideally suited for deep tissue microscopy.

The increase in IR-MPM imaging depth approximates 100% compared to conventional NIR excitation, which will be instrumental in dynamically addressing cell functions in deep cancer lesions. Dual-color tumor cells used in this study express cytoplasmic DsRed2 and EGFP coupled to histone 2B²⁰⁹. Although NIR-MPM is restricted in deep resolution as well as phototoxicity, it is necessary to combine IR and NIR excitation to simultaneously visualize blue and/or green fluorescent proteins, including EGFP.

Therefore, a combination of IR and NIR excitation is most suitable to exploit a maximal amount of fluorescent signals from the green to the NIR range and to display the respective associated cellular and tissue structures, thereby utilizing advantages of IR-MPM for deep tumor imaging.

4.2 Impact of the implantation site and maintenance temperature on biology of tumor lesions (dorsal skinfold chamber)

The dorsal skinfold chamber (DSFC) is broadly used for monitoring primary tumor biology¹⁵⁷. As technical variants, cells are implanted between the dermal fascia and the cover slip of the chamber, either in form of tumor cell suspensions^{164,165}, pellets¹⁶⁷, and spheroids¹⁷¹, or solid tumor explants¹⁶³, with or without a carrier¹⁷². These models provide direct optical access to tumor growth and angiogenesis, but yet fail to recapitulate other aspects of the tumor–stroma interaction, including active invasion. As alternative approach, the injection of pelleted tumor cells into the tissue was used here, which likely provides orthotopic and appropriate 3D tumor–stroma interaction to greater extent than other approaches²³⁰. In contrast to DSFC applications where tumor cells or spheroids are implanted by placing them directly onto the surface¹⁵⁷, direct access to 3D tissue structures combined with intact cell–cell junctions between the tumor cells supports early invasion. The application of NIR- and IR-MPM further revealed that invading tumor cells directly interact with surrounding tissue structures which influence and determine diverse modes of invasion (see paragraph 4.3). Fibrosarcoma and melanoma cells were spontaneously and early able to migrate into the surrounding before tumors reached the onset of neoangiogenesis and exponential growth indicating that no complex microenvironmental changes are necessary to start invasion in highly motile HT-1080 fibrosarcoma, and B16/F10 and MV3 melanoma cells. This is consistent with their mesenchymal nature and stands in contrast to epithelial cancer, where invasive and metastatic progression are thought to involve at least transient EMT induced by the microenvironment and the detachment of individually migrating cells from the tumor mass^{57,155,231,232}. Moreover, since the tumor is topographically confined by the surrounding tissue directly after injection, the volume even in relatively small tumors can be reliably assessed. In line with other tumor models, time-resolved quantification of tumor growth after injection shows an initially slow and linear preangiogenic phase

followed by near-exponential growth after the angiogenic switch, consistent with observations in other models²¹³. High-resolution NIR-MPM further allowed direct assessment of mitotic and apoptotic frequencies from the progressing tumor with relevance for kinetic monitoring of tumor progression and therapy-induced regression (further discussed in paragraph 4.4.2).

In addition to a 3D environment tumor biology is influenced by the maintenance temperature of mice carrying a dorsal skinfold chamber. Mice are kept usually at room temperature, thus we hypothesized that the metal chamber on the back could cool down the tissue contained therein and thereby might negatively impact tumor cell motility as described for epidermal or neural cells in 2D *in vitro* studies^{233,234}; data on cell migration in 3D tissues are lacking. Compared to a housing temperature at 28°C, housing at room temperature affected dramatically the biological activity of two different tumor models, fibrosarcoma and melanoma including growth, neoangiogenesis and local invasion. It remains to be elucidated if further tumor functions like the metastatic potential are decreased in these “colder” tumors, comparable to studies in frogs which showed a temperature dependence of metastatic potential of Lucké renal adenocarcinoma cells²³⁵. Besides affecting tumor biology low temperature likely affects the biology of the microenvironment by reducing microvascular perfusion which in turn slows down tumor growth²³⁶.

To optimize environmental conditions and elucidate the exact temperature of tissue contained in a skinfold chamber exact temperature measurements are necessary and might require additional isolation of the chamber. Additionally, a further increase of housing temperature above 28° might be applicable as preliminary studies showed that mice behavior was not impaired also at 31°C.

In conclusion, by injecting tumor cells directly into the dermal tissue and maintaining mice carrying the skinfold chamber at 28°C we have established an *in vivo* model that allows the analysis of tumor progression including invasion into the surrounding healthy tissue suitable. The model thus provides visual access to early stages and molecular mechanisms of cancer invasion and metastasis via repeated imaging of the same tumor sample in context with the tumor stroma.

4.3 Collective cancer invasion in fibrosarcoma and melanoma: principles, guidance and plasticity

From *in vitro* studies, collective invasion is considered as invasion pattern in several human cancer types, including sarcoma, epithelial cancer and melanoma^{35,51,52,57,149}, but this study provides the first evidence for collective invasion of fibrosarcoma and melanoma *in vivo* and its underlying mechanisms.

4.3.1 Diversity of invasion *in vivo*: Collective invasion is predominant in fibrosarcoma and melanoma lesions

Epifluorescence and NIR/IR-MPM imaging combined with 3D reconstruction showed that orthotopic fibrosarcoma and melanoma xeno- and allografts transplanted into the dorsal skinfold chamber invaded the adjacent microenvironment by different mechanisms. These include individual, but preferentially collective invasion modes which are dependent on the guiding structure surrounding the invading tumor cell (guiding structures see paragraph 4.3.3). The diversity is consistent with *in vitro* invasion assays, where the migration mode is determined by the type of cell embedding into the 3D matrix and the composition and density of the matrix. Imbedded as single cells into a collagen matrix, HT-1080 fibrosarcoma as well as MV3 melanoma cells fail to arrange in multicellular chains but migrate individually^{7,8}. If HT-1080 cells invade from multicellular spheroids into 3D ECM, a combined invasion pattern of single cells and collective strands along ECM tracks and ordered patterns emerges¹⁴. Similarly, explants of rhabdomyosarcoma⁵¹, a further soft tissue sarcoma (STS) malignancy, and melanoma⁵² develop individual as well as collective invasion patterns. Seeded on top of matrigel HT-1080 cells form collective grid-like networks that rather digest their way into the matrigel than conventionally migrate (own observations). From histological sections multicellular invasion patterns are prevalent in mesenchymal tumors and more abundant than disseminated single cell patterns^{183,192}. In a recent study multicellular drifts at the border of breast cancer xenografts were identified, which include some hallmarks of collective cohesive movement (cell-cell junctions), but lack others (defined leading edge/tip cells; guidance structures)²³². In contrast the dermis model is spatiotemporally well controlled and shows clear progression of collective invasion strands into and along surrounding tissue, that is independent of proliferative volume expansion and pushing (see discussion below 4.3.2). These differences of cell displacement in different *in vivo* models call for careful technical and biological control and analysis of collective processes and allow a better classification of different modes of collective invasion.

The process and topographic organization of collective cell movement in cancer lesions is reminiscent of multicellular dynamics in regeneration and morphogenesis, including vascular and epithelial sprouting³. Collective cancer strands thereby mimic the overall appearance, and partially consist of tip cells with extensive filopods guiding following cells. In addition collective invasion pattern in MV3 melanoma cells mimics that of their developmental ancestors - neural crest cells²⁴, whereby cells do not form tight/compact collectives but rather cell chains, one individual cell after the other, partially loosely connected via filopods that touch the adjacent cell or the cell ahead. Therefore, collective invasion of cancers likely recapitulates morphogenetic movements, but it is yet unclear whether collective invasion in cancer and morphogenesis use homologous mechanisms³.

Similar to the adoption of particular migration modes to environmental niches and consistent with data described by *in vitro* studies^{7,52} this study indicates that mesenchymal tumor cells can alter and thereby adapt their migration mode in response to molecular interference *in vivo*. When integrin function was impaired, collective strands tended to disintegrate resulting in collective cell clusters and amoeboid movement of individual cells (own observation from time-lapse movies). Therefore, cells adapt also *in vivo* to their background repertoire of molecules in response to extracellular signals (see detailed discussion 4.4.2.2.).

4.3.2 Components of invasive growth in vivo

The term “invasive growth” is a broadly-used concept describing mainly an invasion of tumor cells originating from a proliferating tumor, often associated with the term EMT^{4,111,231}, however the interconnection between the parameters migration and growth as well as an exact definition of invasive growth remain unclear.

In vivo imaging and dynamic time-lapse histopathology of concurrent cell functions, that are migration, cell-cell interaction and mitotic activity (derived from chromosomal H2B), provide the mechanisms of collective invasive growth for fibrosarcoma and melanoma. As hallmark, moving cell collectives feature both phenomena simultaneously – ongoing cell division of included cells while the collective as a functional unit further invades into the surrounding tissue, indicative of a division of tasks. Cells that actively propel migration are coupled with cells that concentrate on proliferation and expansion of cell mass within the collective. Thereby in the same group two potentially conflicting cell functions (cell division, actin-based migration) occur concurrently instead of sequentially.

The orientation of mitotic planes perpendicular to the invasion direction suggests thereby that cells remain coupled in their orientation during collective invasion and implies cell-to-cell signaling control, e.g. via paracrine loops, such as of c-Met/HGF pathway or SDF-1, or gap junctional communication^{33,45,231,237}. To test whether mitotic activity was required for the invasion process, a mitosis-arrest protocol (fractionated low-dosis irradiation leading to proliferation block) was used to interfere with the growth aspect only. After the first irradiation mitosis was immediately blocked completely, resulting in a residual migration speed of ~50 μm , which was further decreased by additional irradiation probably by slight increase in apoptosis. The further progression of collective invasion suggests that invasion and proliferation are coinciding but independently occurring features. Thereby proliferation could be a supporting factor, such as volume expansion and passive cell drift and thereby support the invasion process.

Although proliferation and migration are found in collective strands of all tested cell lines, the relations between varied. B16/F10 melanoma cells migrated slower (50 $\mu\text{m}/\text{d}$) than HT-1080 fibrosarcoma cells, MV3 melanoma cells invaded similarly efficiently (100

$\mu\text{m/d}$). The relatively low velocity of B16/F10 compared to HT-1080 strands may be connected to their low proliferation rates (1% vs. 3.8% resp.). In contrast, the velocity in MV3 strands cannot be caused by their higher mitotic rates as the net growth (mitosis-to-apoptosis ratio) is worse than in HT-1080 as well as B16/F10, suggesting that passive mass expansion is less relevant for the increase in strand length of MV3 cells.

Consequently, invasive growth can be defined as concurrent collective cell migration (active movement) and ongoing mitotic activity (passive movement), which result both in forward migration of the strand. Invasive growth is thus neither reflected by single-cell dissemination after EMT, i.e. sequential migration versus cell division, nor the smoothly-shaped, blunt interface of expansive growth which lacks the migration component. Although all studied tumor cell lines exert this type of invasive growth, the relative contribution of active and passive migration may be diverse.

4.3.3 Guidance and mechanisms of migration

MPM allowed to three-dimensionally display important tissue structures of the deep dermis surrounding and guiding invading tumors: (i) collagen fibers and muscle strands visualized by SHG, (ii) lymphatic vessels at the tumor border displayed by FITC-labeled LyP-1 peptide after intravenous injection, (iii) perfused blood vessels detected by medium-sized fluorescent dextran molecules (70 kD), and (iv) delayed after injection, interstitial phagocytes which take up dextran leaked out from vessels into the tissue.

3D reconstruction of invasion strands and adjacent tissue structures suggests the invasion type to be governed by both, the tumor cells and the microenvironment. Single-cell dissemination is predominantly occurring superficially in connective tissue between the muscle layer and the cover slip or in the fatty tissue layer, both representing areas of very loose (collagen) structures. In contrast to collective invasion that invades deep into the host tissue guided by preexisting and, in the mouse dermis, mostly aligned tissue patterns including collagen fiber strands, muscle strands, lymphatic, and often blood vessels, individual cells were only found close to the tumor mass borders. This indicates either slow migration speed and early cell death, or a return to the tumor main mass, thereby supporting the hypothesis that the collective invasive niche provides pro-survival signals (see following paragraphs). The cancer cell invasion along preexisting vascular tracks, a process termed vascular cuffing, angiotropism, cooption, or extravascular migratory metastasis is already known from the histopathological pattern of invasive cancers, including prostate cancer²³⁸, melanoma²³⁹ and glioma²⁴⁰. Due to the lack of 3D data and dynamic imaging studies thus far this process was not understood as collective invasion but rather described as source for secondary tumor growth²⁴⁰ and place of intravasation for distant metastasis²⁴¹. The mechanisms underlying the cooption of preexisting vessels could be of diverse nature and are poorly understood (Fig. 42).

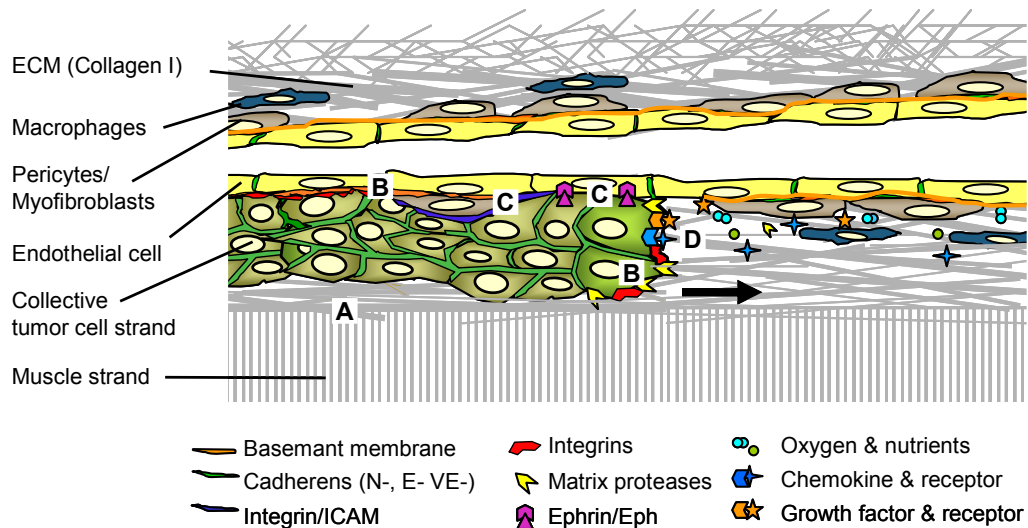


Figure 42. Perivascular invasive niche: stromal, cellular and molecular components and potential interaction sites. Letters indicate location of interaction. Arrow, invasion direction. Abbreviations: BM: basemant membrane; ECM: extracellular matrix; ICAM: Intercellular adhesion molecule.

4.3.3.1 Path of least resistance

Invasion using preexisting tissue structures is consistent with the concept of contact guidance (see 4.3.3.2.), i.e. the migration along tissue discontinuities such as a vessel or muscle strand. Thereby cell movement is further facilitated by the space provided by paths of least resistance (Fig. 42, A). Skin of the back dermis comprises loose as well as more ordered regions with longitudinally oriented collagen fiber bundles of heterogeneous density and interfibrillar spaces⁹³. Non-random, ordered tissue alignments are often associated with adjacent macroscopic structures, such as hair follicles, glands, and parallel muscle strands or blood vessels⁹³. Thus, instead of following anfractuous and poorly structured small tracks in connective tissue areas, such as random collagen networks that might require extensive pericellular proteolysis and/or shape change, cells prefer to move along preexisting linear structures which appear to promote particularly high invasion efficiency. Ordered collagen fibers are often thicker and may represent a stiffer matrix compared to chaotic, loose ECM networks and hence support invasion by providing mechanical cues, a process termed durotaxis⁶⁸.

From *in vitro* studies it is known that invading fibrosarcoma and melanoma cells exert pericellular proteolysis so that hollow tracks are formed within the tissue^{14,188}. These tube-like matrix defects then can be used by following cells, thereby promoting forward movement along aligned ECM structures¹⁴. *In vitro* MT1-MMP is sufficient to abrogate matrix defect generation and collective invasion completely resulting in collective-to-amoeboid transition¹⁴. Due to the heterogeneity of the collagenous organization in interstitial/connective tissue, it is not clear whether such invasion rules also apply *in vivo*. In ongoing experiments stable knockdown of MT1-MMP in HT-1080 fibrosarcoma cells

was recently established (data not shown) so that in future experiments the contribution of tumor-cell derived MT1-MMP to perivascular collective invasion can be tested.

4.3.3.2 Contact guidance

Besides providing tracks of least resistance the perivascular, perilymphatic and perimuscular niches include various possibilities for contact guidance by structural or cellular components.

a) Structural components

Adhesion is a prerequisite for invasion (Fig. 42, B). In addition to the interstitial collagen fibers (discussed in paragraph 4.3.3.1), the basement membrane (BM) is an important structural component separating interstitial tissue compartments, such as by ensheathing blood and lymphatic vessels, as well as muscle strands. Components of the BM include fibronectin, laminins or collagen type IV all of which have been reported to increase cancer cell migration^{241,242}. In case of melanoma, it has been shown ultrastructurally that the melanoma cells are linked to endothelium by an amorphous matrix containing disorganized laminin which is not organized in *bona fide* BMs²³⁹. Accordingly, the C16 laminin peptide, a synthetic laminin 1 fragment, enhances melanoma cell migration *in vitro* and cooption of blood vessels *in vivo* in the CAM model²⁴¹. *In vitro*, most of such ECM derived promigratory signals are transmitted by integrins, such as $\alpha3\beta1$ and $\alpha6\beta1$ for laminin and $\alpha2\beta1$ for fibrillar collagen (Table 1)⁶⁹. However, interference against $\beta1$ and $\beta3$ integrins did not ablate collective invasion along the same tissue tracks *in vivo*, suggesting that adhesion via integrins is not a prerequisite for guidance within the perivascular, perilymphatic or perimuscular niches. We excluded ectopic upregulation of other integrins in $\beta1/\beta3$ knockdown cells *in vitro*, thus it is unlikely albeit not fully excluded that yet another set of integrins (see Table 1) provide functional compensation in knockdown cells. Likewise, non-integrin adhesion molecules including CD44⁸, DDRs⁸³ or surface proteoglycans might be expressed and contribute to collective migration and guidance.

b) Cellular components

High-resolution 3D reconstructions of fibrosarcoma and melanoma strands showed no spatial separation between blood vessels and tumor cells indicating very close proximity (pixel resolution in deep tissue regions around 1 μm). For cooption of blood vessels by melanoma and lung carcinoma after metastatic seeding also direct interaction of tumor cells with endothelial cells or their BM is suggested, but underlying mechanisms remain

unclear²⁴³ (Fig. 42, C). Ephrin/Eph-receptor signaling plays a central role in regulating cell-cell interactions involved in cell migration during development^{195,196}. Members of this protein family are expressed on a wide range of tumor cells, as well as on endothelial cells of the lymphatic and blood vascular system²⁴⁴⁻²⁴⁶. Overexpression of ephrinB2 enhances cell migration and invasion of melanoma cells *in vitro*¹⁹⁷ as well as of glioma cells *in vitro* and *in vivo*²⁴⁷. Since endothelial cells of blood and lymphatic vessels express EphB4¹⁹⁶, the receptor for ephrinB2, and given that vascular BM comprise regions of weakened architecture constitutively²⁴⁸ a direct interaction via these molecules is possible but await direct proof. EphrinB2 and EphB4 are also expressed by HT-1080 fibrosarcoma cells (own preliminary data), yet their role in guiding collective perivascular invasion is unclear. Future experiments are required to address whether stable ephrinB2/EphB4 knockdown will affect their invasion and guidance by blood/lymph vessels. Other direct cell-cell interaction could include molecularly $\beta 2$ integrin/ICAM interactions between tumor and endothelial cells¹³³. The participation of additional cell types, including pericytes, macrophages and myofibroblasts in guided invasion also remains to be elucidated.

4.3.3.3 Chemotaxis and microenvironmental factors

Due to the close proximity of collective tumor cell strands to blood vessels oxygen and nutrients supplied by preexisting capillaries may support the metabolic needs of cell invasion (Fig. 42, D). Moreover, the perivascular stroma is rich in growth factors and chemokines and thus could support altered biology of passenger cells, including invading cancer cells^{249,250}. Growth factors and chemokines play key roles in any guidance of collective invasion during morphogenetic and regenerative processes such as EGF in border cell migration, FGF in tracheal sprouting or SDF-1 in primordium migration³. For instance tumor-associated macrophages originating in the circulation are recruited to the tumor site by tumor-derived attractants and preferentially localize at the tumor-host tissue interface²⁵¹ and release EGF which, in turn, attracts carcinoma cells^{98,99}. Visualization of dextran uptake revealed that phagocytes localized in high numbers around preexisting blood vessels (not shown). Interference with EGF receptor by EGFR blocking antibody (Cetuximab) did not prevent collective fibrosarcoma invasion suggesting that EGF is not essential in promotion and guidance of invasion. Other growth factors not addressed here, including FGF, TGF β or HGF secreted by endothelial cells, pericytes, myoepithelial cells, macrophages or fibroblasts can induce migration of various cancer types^{101,102,104-106,198} and might be important in the fibrosarcoma and melanoma models.

SDF-1 is known to play an essential role in collective primordium migration in zebrafish³. Similarly, myoepithelial cells and myofibroblasts close to invasive breast tumors, but not

those associated with ductal carcinoma *in situ* or normal breast tissue secrete SDF-1¹⁰⁸. Own preliminary experiments with fibrosarcoma xenografts using a CXCR4 (SDF-1 receptor) specific blocking peptide (CTCE-9908)²⁵² revealed that collective invasion was uncompromised, suggesting that SDF-1 is not a prerequisite for collective invasion. However, due to the complexity of the chemokine system, many other chemokines have to be taken into account for compensation. HT-1080 cells express a variety of receptors including CCR3, CCR6, CCR8, CCR10, CXCR1, CXCR3 and CX3CR1 (data not shown). Moreover, chemokines can attract tumor cells to lymphatic vessels, as for CCL21 secreted by lymph endothelial cells in melanoma¹⁹⁸. Thus, likely as consequence of the many growth factor and chemokine receptors expressed by HT-1080 and other tumor cells, no dominant soluble factor driving collective cancer cell invasion *in vivo* could be identified yet.

4.3.4 Match of preclinical mouse model with human disease: similarities and differences

Direct injection of cancer cells into the deep dermis and subcutaneous tissue layers is superior to the commonly used 2D application of cell suspensions onto the tissue interface of xenografts in the skinfold chamber^{167,253} in promoting 3D interaction of the cancer cells with the host tissue. For HT-1080 fibrosarcoma cells this strategy supported a histomorphology strongly mimicking human fibrosarcoma lesions, including the orientation of invasion along small blood vessels and the surrounding pattern of the connective tissue. Importantly, deep 3D scanning allows complete reconstruction of collective invasion strands, whereas 2D histological slicing usually yields potentially misleading round-shaped nests from cross-sectioned invasion strands so that detection of *bona fide* strands requires controlled parallel slicing.

In human melanoma, malignant progression and transition to metastatic state are associated with a vertical growth phase, i.e. deep invasion into the dermis¹⁹². Due to the limited penetration depth using MPM we were not able to detect vertical growth of melanoma in the skinfold chamber, yet the interstitial implantation into the deep dermis mimics tumor progression during vertical growth phase, i.e. direct interaction of melanoma cells with collagenous and vascular tissue structures after loss of BM. Analysis of human melanoma biopsies material show a diversity of invasion pattern including multicellular strands and clusters, as well as individual cells³⁵. Melanoma xenografts implanted in the DSFC bear similarly a great variety of migration modes. Moreover, the cells mimic a phenomenon described to be typically in human malignant melanoma – extravascular migratory metastasis²⁵⁴. Histopathological assessment of human biopsy material detected microscopically melanoma cells in close proximity to microvessels in a

pericytic location²⁵⁴ which is perfectly reflected by B16/F10 and MV3 cells migrating along aligned capillaries of the deep dermal plexus in the dorsal skinfold chamber.

Together, this kinetic study delivers formal evidence for collective invasion from cancer lesions *in vivo*, defines invasive growth as concurrent collective invasion and proliferation, and represents an *in vivo* model that matches the histomorphological invasion patterns of human lesions. The results suggest an important role of the tumor stroma, particularly the pericytic vascular pattern in governing diversity of invasion modes which may explain heterogeneous invasion patterns often observed within the same cancerous lesion^{2,255}. The here discussed negative data suggest a robust invasion route independent of integrins, EGF/EGFR and the SDF-1/CXCR4 (preliminary) axis which poorly responds to molecular interference. Taking this into account, it becomes obvious that invasion and guidance principles *in vivo* are complex and likely depend upon a variety of congruent pathways.

4.4 Microenvironmental control of altered biology in collective invasion strands: identification of a resistance niche

Besides addressing the mechanisms underlying invasion, the use of the modified dorsal skinfold chamber model allows to directly visualize and quantify the response of different tumor compartments to experimental therapy, both conventional as well as novel, molecular therapeutic strategies. The data show an enhanced radio- and chemoresistance of collective invasion strands compared to the tumor main mass and implicate a role for signals provided by the tumor microenvironment in altered tumor biology.

4.4.1 Altered tumor microenvironment

3D reconstruction shows in a controlled way the different anatomic zones of a tumor, suggesting that the tumor main mass and collective invasion strands are surrounded by distinct microenvironments. In the tumor main lesion stromal components such as collagen fibers of intra-tumoral macrophages/phagocytes are rare and tumor cells included mainly exert cell-cell contacts to neighboring tumor cells. In contrast, cells in invasion strands maintain both, cell-cell contacts to tumor cells and to various stromal cells including endothelial cells, pericytes, fibroblasts and macrophages, together with ECM components, that could be of importance in mediating migration, but importantly also in cell survival (see paragraph 4.3.3).

Cell survival may be supported by different pathways located in different regions of the tumor. Altered composition of ECM molecules may mediate integrin-dependent survival

signals⁷¹, and stromal cells surrounding the tumor may provide soluble factors such as EGF, FGF, TGF or HGF, thereby altering gene expression and pro-survival signaling^{101,102,104-106,198,256}. A further major factor is the amount and type of blood vessels. Whereas in the tumor main mass mainly neoangiogenic, tortuous vessels are found that fail to support cell invasion along their outside interface, invasion orientates along aligned preexisting vessels. Newly formed vessels are supposed to be inefficient in nourishing surrounding tissue²⁵⁷; they have a tortuous and irregular shape with abnormal branching patterns and blind ends, lack sphincters and pericytes which make them largely independent from the normal mechanisms regulating capillary blood flow, and are leaky regarding esp. macromolecules²⁵⁸. Cells included in invasion strands do not induce neovessels in the course of 13 days of observation and should be therefore well-supplied with oxygen. Further, the absence of pimonidazole staining (that is an i.v. administered hypoxia marker taken up by hypoxic cells) in histological DSFC samples (data not shown) indicate a normoxic status of collective strands. Due to these anatomic differences, likely oxygen and nutrient delivery differ between invasion strands and main tumor mass. Collective invasion strands may be exposed to more constant oxygen conditions due to close proximity to the preexisting, well-established blood vessel network of the dermal tissue, whereas the growing tumor mass may be confronted with alternating levels of oxygen ranging from normoxia to -hypoxia and thereby impacting proliferation and apoptosis^{259,260}.

Together, anatomic, molecular and functional differences may account for altered cell behavior in different tumor regions.

4.4.2 Altered biology of tumor cells

4.4.2.1 Radiation- and chemoresistance

In fibrosarcoma and other STS, standard post-surgery treatment is achieved by irradiation of the wound bed and adjacent healthy tissue¹⁸². Irradiation thereby is known to induce a great variety of DNA damages including strand breaks, leading to cell cycle arrest thereby allowing damage repair, and if irreparable, induction of apoptosis²⁶¹. Further, STS are a heterogenous group of malignancies in which chemotherapeutic efficacy is difficult to achieve. After surgical tumor resection and irradiation, doxorubicin is thus far the third standard therapy for adult patients with advanced and/or metastatic STS (response rate 25%)¹⁸². Doxorubicin belongs to the group of alkylating agents which are cytostatica that prevent DNA replication by binding to nucleic acids thereby leading to cell cycle arrest similar to irradiation.

Microenvironmental factors that modulate the sensitivity to radiation and chemotherapeutics are the oxidative²⁶⁰ and the adhesive status of a cell²⁶². Well

oxygenated areas such as the invading strands (see paragraph 4.4.1) are supposed to be more radiosensitive²⁶⁰, hence we hypothesized that invasion strands should respond better to radiotherapy than the tumor main mass. Against expectation the tumor main mass regressed efficiently upon irradiation whereas the invasion strands showed near-complete radioresistance and regressed not or only partially.

Besides oxygenation, adhesion to the ECM is known to support radioresistance in different cancer cell lines *in vitro*, including lung, colon, prostate, pancreas, cervix and head and neck, as well as glioblastoma and melanoma, which was termed cell-adhesion mediated radioresistance (CAM-RR)²⁶³. Similarly, cell-adhesion mediated drug resistance (CAM-DR) was detected in glioblastoma²⁶⁴ and myeloma²⁶⁵ cells *in vitro*, yet whether *in vivo* counterparts to CAM-RR and CAM-DR exist is not known. As one of the main hubs for ECM-derived outside-in signaling *in vitro*, integrin engagement regulates cell cycle progression through G1-phase by controlling the expression of key cell cycle proteins, including cyclin D1⁷¹. Consistent with that we found slightly higher mitotic rates in invasion strands compared to the main mass. As part of the cell response to irradiation, contact to ECM proteins supports G1- and G2-cell cycle arrest which prevents cells from potentially damaging replication and provides time for DNA damage repair²⁶². The fact that both main mass and invasion strands underwent complete mitosis arrest excludes differential cell cycle stages/repair of DNA damage as reasons for the difference in radiosensitivity between collective strands and main mass. Conversely, in response to irradiation most invasion strands showed decreased apoptotic rates compared to the tumor main mass. Besides regulating the cell cycle ligated integrins impede pro-apoptotic signaling by upregulation of anti-apoptotic proteins and p53 inactivation, as well as activation of the PI3K/Akt pathway and NF- κ B signaling^{71,82} thereby preventing anoikis⁸¹. Additionally, for small-cell lung cancer β 1 integrin-mediated ECM contact and PI3K activation overrides cell cycle arrest and apoptosis induced by etoposide (a chemotherapeutic agent similar to doxorubicin) treatment *in vitro*, so that cells survive despite persistent DNA damage²⁶⁶. Consistently, doxorubicin treatment of fibrosarcoma xenografts *in vivo* resulted in increased apoptotic frequencies in the tumor main mass but not in invasion strands. An additional link between integrin and chemoresistance was found in pancreatic cancer; here, L1CAM binding to α 5 integrin (e.g. expressed myofibroblasts) leads to the induction of the inducible nitric oxide synthetase and, via nitric oxide release reduces caspase activity²⁶⁷. Furthermore, integrin binding to the ECM can lead to transactivation of EGF receptor signaling without EGF as ligand triggering pro-proliferative and anti-apoptotic signals via the MAPK and PI3K/Akt pathway¹⁰⁹. Besides CAM-RR, other mechanisms underlying radiation resistance observed here could be independent from adhesion; Lewis and colleagues described anchorage-independent radio- and chemoresistance in HT-1080 as well as A375 melanoma cells through modulation of p53²⁶⁸. However, the facts presented in this paragraph suggest

microenvironmental integrin ligands as reason for the differential radiation response in tumor subregions independent of the hypoxic status.

The fate of surviving tumor regions remains unknown at present, due to the currently limited DSFC observation period of 2 weeks. Potentially, cells surviving irradiation could have repaired DNA damage and/or have bypassed apoptosis despite persisting DNA damage, and thereby might restart proliferative activity and form secondary local tumors, as described for glioma^{240,269}. Such post-therapy relapse is not uncommon in fibrosarcoma^{182,191}, and therefore future long-term studies with an extended observation window are needed, such as by using low-weight chambers or re-cultivate explanted (residual) tumor cells to monitor acquired DNA damage.

In contrast to the obvious differential response of tumor main mass and collective invasion strands towards irradiation and doxorubicin, both compartments were similarly resistant to cetuximab treatment, an EGFR blocking antibody and known radiosensitizer²²³. Although cetuximab monotherapy induces tumor regression in approximately 10–20% of advanced cancer patients, many tumors eventually manifest acquired resistance to treatment²⁷⁰. Here, additional resistance mechanisms from those mentioned above may have to be taken into account. *In vitro*, secondary to alterations in trafficking and degradation cetuximab-resistant tumor cells exert increased steady-state EGFR expression, and manifested strong activation of HER2, HER3 and c-Met²⁷⁰.

Taken together, the data provide evidence for collective invasion strands in a specific anatomic region of the peri-tumor microenvironment as location for radio- and chemoresistance *in vivo*. Because of the structural and quantitative differences of available ECM molecules in the perivascular and interstitial dermal niche, interference with integrin function was pursued in order to overcome radioresistance in collective invasion strands.

4.4.2.2 Importance of $\beta 1$ and $\beta 3$ integrins *in vivo*: pro-survival rather than pro-invasion functions

Because of their role in mediating invasion and increased ECM-dependent survival in various tumor cells, interference with integrins was used as potential targeting strategy of fibrosarcoma invasion and radioresistance. To reach maximum interference efficiency of tumor-cell derived integrins and to avoid interference towards the host microenvironment we utilized cells after stable $\beta 1$ and $\beta 3$ RNAi knockdown and supplemented the animal with human-specific anti- $\beta 1$ integrin blocking antibody 4B4. Functional blockade of $\beta 1$ integrin *in vitro* strongly reduces single cell migration efficiency of HT-1080 cells⁷ and leads to the disintegration of collective melanoma clusters⁵². *In*

in vivo however, interference with $\beta 1$ and $\beta 3$ only moderately affected collective invasion in fibrosarcoma lesions. Whereas initial invasion velocities of collective strands after integrin interference were comparable to strands with functional integrins, further invasion beyond day 8 was impeded similar to radiation-induced mitosis-arrest, probably due to an anti-proliferative rather than an anti-invasive effect of integrin interference. This moderate anti-invasive effect might result from compensative upregulation of other integrin β chains *in vivo*, which however was excluded *in vitro*, or the presence of non-integrin adhesion molecules, such as CD44. In contrast, in a non-redundant manner interference with $\beta 1$ and $\beta 3$ integrin strongly affected net-survival of implanted tumor cells by decreasing mitotic and increasing apoptotic frequencies in both, tumor main mass as well as invasion strands. Based on a combined proliferation and survival defect with apoptotic levels elevated above the mitotic level, tumors spontaneously regressed which indicates that integrin-mediated adhesion signaling towards cell survival is massively disturbed during $\beta 1$ and $\beta 3$ integrin interference and not compensated by other receptor pathways. Thus, in HT-1080 fibrosarcoma lesions, integrin functions are essential in pro-survival signaling but not in invasion. These data contrast with the historical view on integrin functions in cancer as to mainly mediate cell adhesion and migration²⁷¹, and rather emphasize outside-in-signaling of integrins in mediating growth aspects of cells²⁷².

The preferential survival of multicellular invasion strands after interference with integrins further suggests that diminished integrin signaling is compensated by additional signals, a phenomenon that was not observed for survival in the main mass. Candidate pathways that might compensate for ablated integrin function include non-integrin adhesion molecules, such as CD44, and growth factor signaling. CD44 is a multifunctional surface receptor to hyaluronic acid and fibronectin which induces phosphorylation of Fyn and Src which are also responsible for regulation of cell proliferation by integrins or growth factors^{273,274}. Other survival-promoting factors include chemokines and growth factors present in the perivascular niche^{101,102,104-106,198,256}. Lastly, cell-cell adhesions exclusively present in this niche (see paragraph 4.3.3.2 b) might account for non-integrin pro-survival signaling.

4.4.2.3 $\beta 1$ and $\beta 3$ integrin-mediated radioresistance

Consistent with the concept of CAM-RR²⁶³, radiotherapy combined to interference with $\beta 1$ and $\beta 3$ integrin resulted in decreased radioresistance with three aspects: (1) accelerated regression of the tumor main mass, (2) significant increase of radiosensitivity of collective invasion strands, and (3) uniform response that lacked the otherwise notable tumor-to-tumor variability. Thus, in combination anti-integrin and radiation therapy caused that tumor masses formerly persisting of nearly half a million cells melt away to

few individualized, residual cells. Thereby the combined interference with $\beta 1$ and $\beta 3$ integrin is of vital importance as single interference of $\beta 1$ alone done before or in other preclinical studies before^{226,228} led to only incomplete tumor regression leaving a substantial amount of viable tumor cells behind. Since high-resolution imaging was not previously used for preclinical studies on anti-integrin therapy, underestimation of residual cell masses is probable^{226,228}. Further, it was not object of these studies, if secondary outgrowth as consequence of remaining cells occurs^{226,228}. Preliminary studies testing the efficiency of anti- $\beta 1$ and αV (the only binding partner for $\beta 3$) antibody treatment on established HT-1080 and MV3 tumors show efficiencies similar to double knockdown approach combined with mAb 4B4, which further supports combinatorial cell-adhesion targeting therapies as attractive radiosensitizing therapy.

In conclusion, we identify a microenvironmentally controlled invasion niche that not only supports efficient collective invasion but also provides integrin-dependent and independent pro-survival signals that compromise therapeutic radio- and chemoefficacy. Dual-interference with $\beta 1$ and $\beta 3$ integrin was sufficient to abrogate the survival advantage leading to complete regression of tumor lesions.

4.5 Implications for human therapy: be aware of the invasive niche!

Patients suffering from fibrosarcoma and other STS malignancies receive as first-line treatment resection of the primary tumor combined to radiotherapy¹⁸²; in case of advanced STS disease Doxorubicin chemotherapy¹⁸². Similarly, melanoma are first excised^{275,276} but not irradiated due to their inherent radioresistance²²¹. First-line treatment of metastatic disease here involves interferon²⁷⁷ and IL-2²⁷⁸, eventually dacarbazine as chemotherapeutic agent²⁷⁹. For both diseases no standard therapy is available for late-stage patients, and various multimodal treatments including classical chemotherapeutics as well as newest molecular substances are tested in clinical trials[†]. Given these therapeutic limitations, the results described in this study suggest that anti-integrin therapy might be an attractive complementary therapy to classical regimens.

4.5.1 Deep tissue invasion: a matter of resection margins

In human STS^{182,280} and melanoma²⁸¹ patients, besides standard prognostic markers such as tumor size and histological grade, the appearance of resection borders is of main importance determining local recurrence and tumor-related mortality. In clinical routine, radial excision margins for fibrosarcoma are in the range of centimeters, as tissue structures permit, and for melanoma in the range of 1 to 2 cm²⁷⁵ (dependent on the

[†] see website U.S. National Cancer Institute

thickness of the primary lesion). To control for tumor-free resection margins in superficial melanoma, digital epiluminescence microscopy was recently introduced into clinical routine²⁸². Thus, clinical practice suggests that primary invasion extends deeply away from the macroscopically visible primary lesion. In human histopathology and in the mouse model used here, collective invasion represents the major invasion mode. HT-1080 fibrosarcoma as well as MV3 melanoma cells invaded very efficient and reached average velocities of calculated 1 cm in 3 months whereby fastest individual strands achieved lengths of 0.5 cm within the two-week observation window. Although the fate of deeply invading multicellular strands is currently unclear, the tips of the strands are macroscopically invisible and thereby may reach or exceed radial excision margins. Post-surgery local recurrences are developed by 20% of STS patients (without postoperative irradiation)²⁸⁰, and by 4% of melanoma patients (with thicker lesions of 2-4 mm)²⁸³. Thus, deep collective invasion but not single-cell dissemination may be accountable for most of peritumor invasion and probably also for local post-operative recurrence of sarcoma. Whether collective invasion strands eventually lead also to metastatic intravasation remains to be purpose of future studies.

4.5.2 Anti-angiogenic therapy: no matter regarding early invasion

In certain tumor models the angiogenic switch supports metastatic cancer cell dissemination, however the early time- and function-relationship is poorly understood^{253,284}. Likely mediated by direct contact to the surrounding stroma, the onset of collective invasion after spheroid implantation occurred before and independently of tumor-induced neoangiogenesis. Thus, tumors prior to or without the angiogenic switch are able to transit to invasion and dissemination stage, and therefore their invasion may be not prevented by anti-angiogenic agents. Conversely, recent studies on melanoma²⁸⁵ and pancreatic cancer²⁸⁶ show that antiangiogenic therapy can facilitate malignant progression resulting in increased local invasion and distant metastasis. Thereby, invasion described in our study could be interpreted as a process arising from the primary ability of a tumor to invade, whereas invasion in response to a treatment could be a secondary ability of a tumor to adapt to and compensate anti-tumor treatment.

4.5.3 Radio- and chemotherapy: a matter of tumor-compartment

Although it is known that tumors are heterogeneous, i.e. the expression and signaling states vary considerably within the same cancer lesion²⁸⁷, most such concepts on cancer resistance are not directly validated by suitable kinetic monitoring, such as intravital imaging, so that little information exist about differential behavior of often small tumor subregions in response to therapy^{221,262,270}. An exception is hypoxia where intratumoral

variations in oxygen supply are commonly monitored by (histological) imaging and suited to control therapy response of different tumor compartments^{259,288,289}.

The “dynamic pathology” approach used here strongly supports the concept of biological heterogeneity within the same tumor lesion *in vivo*. Using high-resolution optical imaging, a hypoxia-independent radio- and chemo-resistance niche was identified, consistent with concepts on CAM-RR²⁶³ or CAM-DR²⁶⁴.

Given that microscopically resolved imaging techniques are not yet standard in animal models of cancer or human patients, the importance of such subregions and their differential response to therapy in early and late progression of malignant disease is unclear. In current practice, the primary diagnosis as well as follow up after therapy are obtained only indirectly by macroscopic imaging and contrast enhancement based on blood flow parameters, such as by computer tomography or magnetic resonance imaging, or glucose uptake by positron emission tomography^{290,291}, thus not sensitive enough to monitor small subregions that are not linked to hyperperfusion, as detected here. Hence, small tumor residues not associated with necrosis, altered metabolic state or hypoxia might contribute to incomplete tumor eradication and post-therapy relapse. To detect such subcompartmental resistance niches preclinical (and eventually clinical) monitoring will need to include before therapy and for follow-up better high-resolution imaging techniques that are not relying upon neovascularization.

4.5.4 Multimodal therapy: Key to success!

The results presented in this study suggest that radiotherapy combined with anti-integrin therapy may enhance tumor regression rates in otherwise radioresistant tumors or tumor subregions. To date, clinical anti-integrin trials tested the efficacy of individual, mainly αV integrin inhibitors in late-stage solid and often already metastasized tumors with the aim to interfere with angiogenesis⁸² (see Table 4).

Table 4. Summary of clinical trials testing efficiency of integrin inhibitors (adapted from Dregosellier & Cherish, 2010⁸²).

Integrin	Inhibitor name	Type	Clinical trial	Tumor type	Results
$\alpha V\beta 3$	Etaracizumab (Medi-522) or Vitaxin (precursor)	Antibody	Phase I	advanced solid tumours, renal cell cancer	some patients antiangiogenic activity, low toxicity, disease stabilization
			Phase II	Metastatic melanoma	no additional effects to dacarbazine treatment
$\alpha V\beta 3/\alpha V\beta 5$	CNTO95	Antibody	Phase I	advanced solid tumors	non-toxic, signs of anti-tumour activity
$\alpha V\beta 3/\alpha V\beta 5$	Cilengitide	Peptide	Phase II / III	Recurrent glioblastoma, refractory brain tumors in children	partially full response, extension of patient survival; probably due to blood flow changes
$\alpha 5\beta 1$	Voloxicimab	Antibody	Phase I / II	Advanced solid tumors	well-tolerated, clinical efficacy
	ATN-61	non-RGD Peptide	Phase I	Advanced solid tumors	well-tolerated, prolonged stable disease

The trials or preclinical studies thus far did not consider integrin interference on early tumor progression nor combination regimens.

Recent preclinical studies have addressed the efficacy of anti- $\beta 1$ ²²⁶ or anti- αV ²²⁸ integrin treatment combined with irradiation, and both report a (partly) improved response to radiotherapy. However no study has addressed the fate of potential residual masses, as well as the combined effect of targeting both, $\beta 1$ and $\beta 3$ integrin. The data here show the importance of combined interference for achieving complete rather than partial regressions. Although the efficacy of single vs. multimodal treatment needs to be validated in detail, the success of preliminary studies testing the efficiency of $\beta 1$ and αV integrin dual antibody treatment combined with radiotherapy on established fibrosarcomas and melanomas suggest combinatorial cell-adhesion targeting therapies as attractive complementary therapy to classical regimens of problematic tumors. Whereas long-term anti- $\beta 1/\beta 3$ -integrin therapy may cause substantial systemic side-effects that are not further discussed here but may preclude their application in humans, short-term interference for defined indications, as used here, may be more promising.

A suitable procedure covering different aspects of tumor progression and resistance might include: (1) irradiation and/or classical chemotherapy to abolish cell proliferation, (2) multi-molecular targeting of potential cell-adhesion molecules as well as growth factor receptors to impede pro-survival signaling, or inhibitors effecting common underlying signaling molecules²⁹²⁻²⁹⁴, and (3) eventually subsequent anti-angiogenic therapy to delay outgrowth of local and distant metastasis.

Taken together, the clinical implications of this study are three-fold. First, collective fibrosarcoma and melanoma invasion penetrates deeply into the surrounding healthy tissue and, after incomplete resection, give rise to secondary outgrowth. Second, the response to therapy of the invasion regions is different than that of the main tumor and requires future work, both preclinically and clinically. Third, first attempts to combine irradiation with dual anti-integrin therapy strongly suggest to consider early multi-molecular treatment of invasive tumors.

4.6 Concluding remarks

The results presented here emphasize the importance of high-resolution imaging combined to orthotopic *in vivo* models to investigate and understand mechanisms of tumor progression and response to experimental therapy. The newly identified collective invasion and survival niche extents current concepts of cancer invasion and implicates epigenetic control mechanisms that warrant future molecular analysis.

Next to established whole-body imaging approaches (radiology, magnetic resonance imaging (MRI), positron emission tomography (PET)/Single photon emission computed tomography (SPECT), IR-MPM is an emerging technique with wide spectral range and sufficient penetration depth to monitor tumor details beyond its surface. If combined with endoscopic imaging and NIR optical molecular tracers, IR-MPM may be a method of choice for future endoscopic detection of tumors inside the body in preclinical and clinical settings.

For future advanced long-term imaging of tumor progression, prolonged observation periods using low-weight chamber types will be mandatory. This will help to broaden the knowledge also about advanced tumor stages including processes such as central necrosis and bleeding, intravasation into blood and lymph vessels as initiative step for distant metastasis, but also development of tumor relapse after therapy.

Both, invasion patterns and mechanisms, here described for fibrosarcoma and melanoma lesions, may hold true also for other cancer types with known multicellular invasion patterns in histopathological sections, including epithelial cancers and other sarcoma types⁵⁷, that are amenable to be monitored as orthotopic lesions using the modified skinfold chamber model. A close link between preclinical and clinical pathology should be standardized and matched not only in histomorphology but also in molecular expression and signaling states. If resembling human lesions, orthotopic xenograft models may be suited to provide insight into progression of various cancer types and regression cascades with relevance for human disease.

5 MATERIAL AND METHODS

5.1 Antibodies, Pharmaceuticals, Inhibitors

The following primary antibodies (Table 5), isotypes (Table 6) and secondary antibodies (Table 7) were used for *in vitro* studies.

Table 5. Primary antibodies.

Antigen	Clone	Species	Conjugation	Stock conc. (mg/ml).	Company	Application
hu α smooth muscle actin	1A4	mouse	/		DAKO	Histo
hu CD31	MEC13.3	rat	/		BD Bioscience	Histo
hu CD31	JC70A	mouse	/		DAKO	Histo
hu CD44	IM7	rat	FITC	0.5	eBioscience	FACS
hu Integrin α 1	TS2/7	mou	/	1	Abcam	FACS
hu Integrin α 2 (CD49b)	AK-7	mou	FITC	0.05	BD Biosciences	FACS
hu Integrin α 3 (CD49c)	C3II.1	mou	PE	0.00625	BD Biosciences	FACS
hu Integrin α 5	SAM-1	mou	/	2	Millipore	FACS
hu Integrin α 6 (CD49f)	GoH3	rat	/	0.5	BD Biosciences	FACS
hu Integrin α V (CD51)	AMF7	mou	FITC	1	Beckman Coulter	FACS
hu Integrin β 1 (CD29)	4B4	mou	FITC	1	Beckman Coulter	FACS
	4B4	mou	/	1	Beckman Coulter	Cell culture
	18/CD29	mou	/	0.25	BD Biosciences	WB
hu Integrin β 2 (CD18)	7E4	mou	FITC	0.1	Beckman Coulter	FACS
hu Integrin β 3 (CD61)	SZ21	mou	FITC	0.15	Beckman Coulter	FACS
hu Integrin β 4 (CD104)	439-9B	rat	FITC	0.0125	BD Biosciences	FACS
hu Integrin β 5	KN52	mou	PE	0.003	eBioscience	FACS
hu Integrin β 6	437211	mou	PE	0.025	R&D	FACS
hu Integrin β 7	FIB504	rat	PE	0.00625	BD Biosciences	FACS
hu α -Tubulin	DM1A	mou	/	1	Millipore	WB

Table 6. Isotypes.

Isotype	Clone	Conjugation	Stock conc. (mg/ml).	Company	Application
mouse IgG1k	679.1Mc7	/	0.1	Beckman Coulter	FACS
	MOPC-21	FITC	0.05	BD Biosciences	FACS
	ICIG1	FITC	0.0125	Immunostep	FACS
	MOPC-21	PE	0.2	BD Biosciences	FACS
mouse IgG2bk	GC198	/	0.5	Millipore	FACS
	27-35	PE	0.2	BD Biosciences	FACS
rat IgG2ak	R35-95	/	0.5	BD Biosciences	FACS
	R35-95	PE	0.2	BD Biosciences	FACS
rat IgG2bk	A95-1	FITC	0.5	BD Biosciences	FACS

Table 7. Secondary antibodies.

Antigen	Species	Conjugation	Stock conc. (mg/ml)	Company	Application
mou IgG (H+L)	goat	Alexa488	2	Invitrogen	FACS
mou IgG (H+L)	goat	HRP	0.4	Jackson Immunoresearch	WB

For *in vivo* experiments the following substances were applied (Table 8).

Table 8. Substances for *in vivo* use.

Substance	Stock concentration	Company
anti-Integrin β 1 (CD29) clone 4B4	1 mg/ml	Beckman Coulter
mouse IgG1 κ clone P3	0.5 mg/ml	eBioscience
Doxorubicin hydrochloride	1 mg/ml	Sigma Aldrich
Erbix (Cetuximab)	5 mg/ml	Merck Serono
CTCE-9908	10mg/ml	Britisch Canadian Biosciences

5.2 Cells and cell culture

HT-1080 human fibrosarcoma and MV3 human melanoma cells were cultured in DMEM (PAN Biotech GmbH), B16/F10 mouse melanoma cells were cultured in RPMI-1640 (PAA, Pasching, Austria) supplemented with 10% fetal calf serum (FCS; Aurion), penicillin and streptomycin (both 100 μ g/ml; PAN) at 37°C in a humidified 5% CO₂ atmosphere. For dual color variants of HT-1080, B16/F10 and MV3, which expressed cytoplasmic DsRed2 and nuclear histone 2B (H2B)-EGFP²⁰⁹, Hygromycin B (0.2 mg/ml; Invitrogen) was added to the medium, for B16/F10 and MV3 additionally G418 sulfate (0.2 mg/ml; Calbiochem). For stable HT-1080 knockdown cell lines medium was supplemented with antibiotics dependent on the shRNA transfection variant (Table 9).

Table 9. Selection antibiotics for shRNA cell line variants.

Cell line	Lentiviral RNAi vectors	Cell lines variants	Antibiotics	Concentration	Company
HT-1080 (and dual color variants)	p-puro	Control	Puromycin	5 μ g/ml	Sigma Aldrich
		b1.2			
	p-puro/p-neo	Control	Puromycin	5 μ g/ml	Sigma Aldrich
		b1.2/b3.1	G418	400 mg/ml	Calbiochem

5.3 Generation of stable knockdown cell lines by lentiviral shRNA

shRNA sequence targeting *ITGB1* (β 1 integrin) and *ITGB3* (β 3 integrin) for gene silencing by RNA interference was cloned into the lentiviral vector pLBM either containing a puromycin (p-puro) or a neomycin (p-neo) cassette for selection by antibiotics as described in Kissler et al²⁹⁵. The shRNA target sequences are listed in Table 10. Lentiviral particles were produced as described previously²⁹⁵ and concentrated by ultracentrifugation. HT-1080 parental and dual-color cells were infected with p-puro or p-neo viruses (vector controls), or with *ITGB1* (on p-puro) or *ITGB3*-targeting (on p-neo) pLBM viruses. For generation of double knock down cells, HT-1080 p-puro or HT-1080 β 1kd (clone 2) cells were additionally infected with *ITGB3*-targeting (clone 1) or p-neo viruses, respectively.

Table 10. shRNA target sequences.

Gene	Clone	Sequence
<i>ITGB1</i>	1	CGCCCTCCAGATGACATAGAAA
	2	CGCCACAGACATTTACATTTAAA
	3	CGCAAATTCTAGCAATGTAATT
	4	AGCAAATTGTCAGAAGGAGTAA
<i>ITGB3</i>	1	CAGTCACTTTCTTCTTCTTAAA
	2	ATGTGGGAGTGTGTAATTTAAA
	3	AGGACTTACTGTGTCATCAAAT

5.4 In vitro assays for proliferation, migration and protein expression

5.4.1 Cell proliferation

The same amount of different cells lines that are to be compared were cultured in standard liquid culture plates, and cell numbers were counted after 48h of growth.

5.4.2 Cell migration assays

Adherent subconfluent cells were detached with 2mM EDTA and suspended in medium to a final concentration of 1×10^6 /ml. One part of cells in FCS-containing medium was incorporated into two parts of a bicarbonate-buffered dermal bovine type 1 collagen (Vitrogen; Nutacon) solution in MEM (Sigma Aldrich) (1.67mg/ml final collagen concentration), and after polymerization overlaid with medium¹⁴⁷. For interference studies medium was supplemented with $\beta 1$ integrin blocking mAb clone 4B4 (10 μ g/ml) and/or cyclic RGD peptide (cyclo(-Arg-Gly-Asp-D-Phe-Val); 575 mg/ml; Bachem).

Cryopreserved skin was diagonally cut into 100 μ m thick slices and placed on coverslips. Multicellular spheroids of dual-color HT-1080 cells were grown in poly-D-lysine coated, non-adhesion cell culture plates (NUNC) overnight, placed on skin slides, and after initial adhesion overlaid with medium.

5.4.3 Flow cytometry

Cells were cultured in 3D collagen lattices for 24h. Suspended cells were obtained by digestion with collagenase I (1000 U/ml, 30 min, 37°C; Sigma Aldrich), pelleted and stained with primary antibodies (Table 1, dilution 1:5 (integrin $\alpha 5$), 1:10 ($\alpha 2$, $\beta 2$, $\beta 3$, CD44), 1:20 (αV , $\beta 4$, $\beta 7$), 1:25 ($\alpha 3$), 1:50 ($\beta 5$, $\beta 6$), 1:100 ($\alpha 1$, $\beta 1$)) or respective isotypes (30 min, on ice) and, if not primary conjugated, afterwards with Alexa488-conjugated goat anti-mouse IgG as secondary antibody (20 μ g/ml). Viability of cells was tested with propidium iodide (1 μ g/ml).

5.4.4 Protein gelelectrophoreses and Western Blot

For detection of integrin knockdown efficiency in HT-1080 dual-color cells western blotting was used. Cells from cell culture were lysed and samples were separated under reducing conditions on SDS-8% PAGE. Proteins were transferred onto a nitrocellulose membrane, blocked with 2% Milk-PBST for 1h, and then incubated overnight with primary antibodies (integrin β 1 0.25 μ g/ml). Afterwards membranes were washed with PBST and incubated with HRP-conjugated anti-mouse IgG (0.125 μ g/ml; Jackson Immunoresearch) for 1h. After final washing signal was detected using Luminol/H₂O₂. To control loaded protein amount membranes were stripped using Restore Western Blot Stripping buffer (Thermo Scientific). Afterwards detection procedure started again with blocking. As control protein α -tubulin was used (1st antibody 1 μ g/ml).

5.5 Dorsal skinfold chamber (DSFC) model

Dorsal skin-fold chambers were transplanted onto 8 to 10 week-old male athymic Balb/c-nu/nu mice (Charles River), as described by Guba and colleagues¹⁶⁷. One day post surgery, either a cell pellet containing approx. 5×10^5 tumor cells was placed onto the tissue surface (drop-on method) or, as injection technique, 2 to 4 μ l of pelleted cells ($\sim 1 \times 10^8$ cells/ml) were injected into the dermis adjacent to the deep dermal vascular plexus with a 30 G needle and monitored for up to 14 days. False-positive results by active or passive cell movement along the injection channel were excluded by injecting tumor cells in perpendicular direction to the length axis of the mouse (i.e. invasion direction). Further, scattering along the injection channel as putative cause for cancer cell dissemination was excluded as follows: (i) by reconstructing the non-perturbed tissue scaffold at the tumor-stroma interface using second harmonic generation (SHG) signal of collagen fibers; and (ii) fluorescence from non-disrupted vessels after i.v. application of FITC- or Alexa Fluor-660-conjugated dextran (70 kD; Invitrogen).

Experimental interference started either with implantation of tumor cells or, as therapy approach, when tumors were established; protocols and dosing see Fig. 43. Local irradiation was performed using a RT 50 (Philips Medical Systems) with a dose-rate of 4.9 Gy/min to generate 3, 4 or 10 Gy per session. Before injection NaN₃-containing substances (mAb 4B4, mIgG1) were dialyzed 1:1000 against 0.9% NaCl. Inhibitors and antibodies were injected i.p.

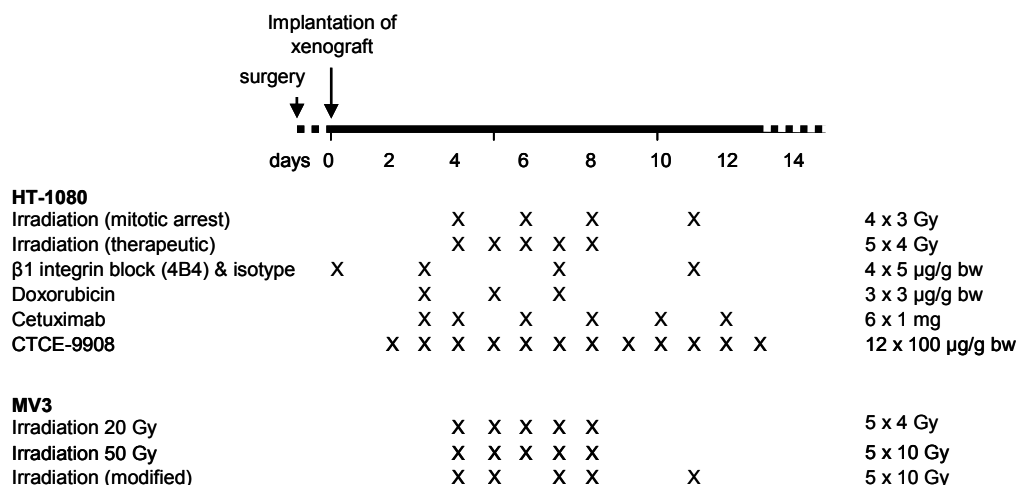


Figure 43. Time scale and dosing overview for treatment of HT-1080 and MV3 xenografts.

5.6 Histochemistry

5.6.1 Dorsal skinfold chamber skin

Tumor bearing, dorsal skinfold chamber carrying mice were sacrificed on day 7 of tumor progression and after tumor status was documented by epifluorescence microscopy dorsal skin was harvested, embedded in O.C.T. compound (Sakura), deeply frozen and stored at -80°C. Prior to staining fresh 10 µm thick cryosections were prepared, mounted on superfrost object slides and routinely stained with eosin and haematoxylin. For immunohistochemistry cryosections were fixed with 2% paraformaldehyde. After blocking of unspecific epitopes (5% BSA, 0.1% water fish skin gelatin) blood vessels were stained using rat monoclonal anti-human CD31 antibody (clone MEC13.3BD Biosciences; 1:100) and, as secondary ab, anti-rat IgG (H+L) -Alexa Fluor 647 (Invitrogen; 1:1000). Cell nuclei were stained by DAPI (2 µg/ml). Afterwards samples were embedded in mowiol mounting medium.

5.6.2 Human primary fibrosarcoma samples (carried out by Uta Flucke)

Human tissue was fixed in 4% buffered formalin, routinely processed and embedded in paraffin; 2-4 µm thick sections were stained with hematoxylin and eosin and immunohistochemically stained by the labelled Streptavidin Biotin (LSAB) technique using mouse monoclonal antibodies anti-human α smooth muscle actin (clone 1A4, 1:500) and anti-human CD31 (clone JC70A, 1:100) (both DAKO). Antigen retrieval was performed. Appropriate positive and negative controls were used throughout.

5.7 Bright-field time-lapse videomicroscopy

For the visualization of cell migration in process, cells were monitored by time-lapse microscopy either in 3D collagen lattices or as spheroids on dermal skin within self-constructed migration chambers (5% CO₂, humidified atmosphere)¹⁴⁷.

To construct the migration chamber an object slide and a coverslip were connected by a spacer composed of vaseline / paraffine (1:1), resulting in an approximate chamber size of 20 x 20 x 0.5 mm and a volume of ~200 µl.

Samples were placed under inverse light microscopes (Leica) coupled to CCD cameras, and maintained at 37°C using an infrared heating system. Images were taken at 4 min intervals for a duration of 24h, using 10x objectives.

5.8 Confocal microscopy

For detection of fluorescence signals in immunohistochemistry samples a Zeiss LSM 500 (Zeiss) confocal microscope with a 63x oil immersion objective was used. For excitation a 488 nm Argon laser combined with a HFT 405/488/543/633 multiple beam splitter was used. A BP 420-480 emission filter was additionally applied for detection of DAPI signals, a NFT 545 dichroic mirror for green signals (H2B-EGFP), a BP 565-615 for cytoplasmic DsRed2 or a BP 650-710 for Alexa647 labeled antibodies. Samples were scanned as z-stacks at steps of 2 µm for simultaneous 3D reconstruction of fluorescence and transmission.

5.9 Near-infrared and infrared multiphoton microscopy (NIR-/ IR-MPM)

5.9.1 Microscope components

An automatic tunable Ti:Sa laser (82 MHz, 180 fs, 1.7 W; Chameleon-XR; Coherent Inc.) generating pulsed radiation in the range of 710 to 980 nm was used as excitation light source for blue and green dyes (conventional MPM) and further served as pump source for an OPO (PPAutomatic; APE) based on a periodically poled crystal. Being synchronously pumped at 775 or 830 nm the OPO emission ranged from 1060 to 1450 nm. Wavelength tuning was achieved by varying the cavity length. The OPO-output power was 250 to 300 mW. The radiation from the Ti:Sa laser and the OPO was guided through 2 independent chirp arrangements, each consisting of two prisms to compensate for pulse broadening caused by the intermediate optics and the objective lens, and then coupled into a customized scanhead (TriM Scope; LaVision BioTec) designed for simultaneous Ti:Sa and OPO imaging. All optical elements in the OPO beam pathway (mirrors, lenses, objective lens) were optimized and chosen for best transmission and

correction over the range of 1060 – 1500 nm, resulting in an excitation power of 100 to 125 mW (1060 to 1300 nm) in the focal plane despite a 15 % over-illumination of the objective lens. The detection unit consisted of 4 non-descanned detectors (PMTs) in backward. Switchable dichroic mirrors and bandpass filters were used to separate the emission signals (typical setup: blue (400/40) for SHG, green (535/50) for EGFP, red (605/70) for DsRed2, and far-red emission (710/75)). For further details see Andresen et al, 2009¹⁴⁴.

5.9.2 Spectroscopy

Wavelength tuning was controlled using a spectrometer, computer-automated and synchronized with the scanhead. Using a linescan mode, fluorescence and SHG signals were projected onto the entrance slit of spectrograph (SP-150; Acton Research Corp.), and recorded with a CCD camera (Imager Intense; PCO). By moving the motorized sample stage perpendicular to the direction of the line, consecutively acquired images allowed the recording of a spectral-resolved image in x and y from a sample plane and the intensity profiles were quantified for specific regions.

The spectrum of EGFP and DsRed2 was analyzed using living HT-1080 dual-color cells, and further, for separation and clean spectral analysis, native gel electrophoresis was carried out using HT-1080 dual-color cell lysates. Cells were lysed in LSB (without β -mercaptoethanol) and loaded on 8% native PAGE. After electrophoresis gels were immediately dried and imaged using a BioRad Pharos FX Plus Molecular Imager (EGFP: 488nm excitation; BP535-30; DsRes2: 532nm excitation; BP695-30) and further investigated using IR- and NIR-MPM. Moreover, SHG and spectral-resolved fluorescence measurements were performed on 30 to 500 μ m thick cryosections from non-fixed human skin.

5.9.3 Time-lapse microscopy of photobleaching, photodamage and migration

Photobleaching of DsRed2 in living HT-1080 dial-color cells was measured as decrease in emission during consecutive scanning at 760, 880, and 1100 nm excitation wavelengths and a power of 75 mW. The samples were subjected to 250 consecutive scans and the emission intensity was quantified as average pixel intensity of the entire scanning field and normalized to the intensity of the first frame. Protein condensation due to continuous excitation was measured by continuous imaging of dual-color HT-1080 cells at a high excitation power (110 mW) and a frame rate of 2.8 fps. Migration of HT-1080 cells from a multicellular spheroid on a dermis slice was analyzed during continuous excitation at 1100 nm and 117 mW power in the focus.

5.9.4 Intravital microscopy

For intravital microscopy, mice were anesthetized with isoflurane and stably mounted onto a temperature-controlled platform (37°C). Overview epifluorescence microscopy of xenografts was performed with a 4x objective (NA 0.3), multiphoton microscopy with a 20x objective (NA 0.95; both Olympus). Sequential 3D stacks were obtained for up to 500 µm penetration depth at a step size of 5 µm. Blood vessels were visualized by injecting 2 to 4 mg of Alexa Fluor 488- or 660-conjugated dextran (70 kD; Invitrogen) into the tail vein or retroorbitally. Activated lymphatic vessels were detected after injection of the lymph-homing cyclic peptide LyP-1 (100 µg)²⁹⁶.

5.10 Image analysis

Images were reconstructed and analyzed using ImageJ 1.40g (W. Rasband, NIH), ImSpector 3.4 (LaVision BioTec GmbH), Photoshop CS 8.0.1 (Adobe Systems Inc.), and Volocity 4.0.1 (Improvision). Single cell velocities were obtained computer-assisted cell tracking using Autocell (Universities of Bremen and Wuerzburg). Tumor volume (V) was calculated as $(\text{tumor width})^2 \times (\text{tumor length}) \times \pi/6/2$. Velocity of invasion strands was analyzed as described in Fig. 18, either by time-lapse microscopy of nuclear dynamics (Fig. 18a), single strand dynamics (Fig. 18b), or from repetitive 3D MPM microscopy over days. Mitotic and apoptotic fractions were determined from the H2B-EGFP pattern from 100 cells per independent visual field. The orientation of mitotic figures was expressed as angle relative to the length axis of the invasion strand. The tortuosity of vessels was calculated as index of the actual length of the vessel divided by the straight-line length from the beginning to the end from a visual field. Residual invasion areas after irradiation were determined as described in Fig. 31.

5.11 Statistical analysis

For statistical analysis the two-tailed Mann-Whitney U-Test for independent and the paired students t-test for dependent samples was used.

6 REFERENCES

1. Friedl, P. & Wolf, K. Plasticity of cell migration: a multiscale tuning model. *J Cell Biol* **188**, 11-19 (2009).
2. Friedl, P. & Wolf, K. Tumour-cell invasion and migration: diversity and escape mechanisms. *Nat Rev Cancer* **3**, 362-374 (2003).
3. Friedl, P. & Gilmour, D. Collective cell migration in morphogenesis, regeneration and cancer. *Nat Rev Mol Cell Biol* **10**, 445-457 (2009).
4. Thiery, J.P. Epithelial-mesenchymal transitions in tumour progression. *Nat Rev Cancer* **2**, 442-454 (2002).
5. Friedl, P., Zanker, K.S. & Brocker, E.B. Cell migration strategies in 3-D extracellular matrix: differences in morphology, cell matrix interactions, and integrin function. *Microsc Res Tech* **43**, 369-378 (1998).
6. Paulus, W., Baur, I., Beutler, A.S. & Reeves, S.A. Diffuse brain invasion of glioma cells requires beta 1 integrins. *Lab Invest* **75**, 819-826 (1996).
7. Wolf, K., *et al.* Compensation mechanism in tumor cell migration: mesenchymal-amoeboid transition after blocking of pericellular proteolysis. *J Cell Biol* **160**, 267-277 (2003).
8. Maaser, K., *et al.* Functional hierarchy of simultaneously expressed adhesion receptors: integrin alpha2beta1 but not CD44 mediates MV3 melanoma cell migration and matrix reorganization within three-dimensional hyaluronan-containing collagen matrices. *Mol Biol Cell* **10**, 3067-3079 (1999).
9. Tester, A.M., Ruangpanit, N., Anderson, R.L. & Thompson, E.W. MMP-9 secretion and MMP-2 activation distinguish invasive and metastatic sublines of a mouse mammary carcinoma system showing epithelial-mesenchymal transition traits. *Clin Exp Metastasis* **18**, 553-560 (2000).
10. Devreotes, P.N. & Zigmond, S.H. Chemotaxis in eukaryotic cells: a focus on leukocytes and Dictyostelium. *Annu Rev Cell Biol* **4**, 649-686 (1988).
11. Haston, W.S., Shields, J.M. & Wilkinson, P.C. Lymphocyte locomotion and attachment on two-dimensional surfaces and in three-dimensional matrices. *J Cell Biol* **92**, 747-752 (1982).
12. Mandeville, J.T., Lawson, M.A. & Maxfield, F.R. Dynamic imaging of neutrophil migration in three dimensions: mechanical interactions between cells and matrix. *J Leukoc Biol* **61**, 188-200 (1997).
13. Lewis, W.H. On the locomotion of the polymorphonuclear neutrophils of the rat in autoplasm cultures. *Bull. Johns Hopkins. Hosp.* **4**, 273-279 (1934).
14. Wolf, K., *et al.* Multi-step pericellular proteolysis controls the transition from individual to collective cancer cell invasion. *Nat Cell Biol* **9**, 893-904 (2007).
15. Friedl, P. & Brocker, E.B. The biology of cell locomotion within three-dimensional extracellular matrix. *Cell Mol Life Sci* **57**, 41-64 (2000).
16. Condeelis, J., Jones, J. & Segall, J.E. Chemotaxis of metastatic tumor cells: clues to mechanisms from the Dictyostelium paradigm. *Cancer Metastasis Rev* **11**, 55-68 (1992).
17. Farina, K.L., *et al.* Cell motility of tumor cells visualized in living intact primary tumors using green fluorescent protein. *Cancer Res* **58**, 2528-2532 (1998).
18. Friedl, P., Borgmann, S. & Brocker, E.B. Amoeboid leukocyte crawling through extracellular matrix: lessons from the Dictyostelium paradigm of cell movement. *J Leukoc Biol* **70**, 491-509 (2001).
19. Verschueren, H., De Baetselier, P. & Bereiter-Hahn, J. Dynamic morphology of metastatic mouse T-lymphoma cells invading through monolayers of 10T1/2 cells. *Cell Motil Cytoskeleton* **20**, 203-214 (1991).
20. Rintoul, R.C. & Sethi, T. Extracellular matrix regulation of drug resistance in small-cell lung cancer. *Clin Sci (Lond)* **102**, 417-424 (2002).
21. Wood, S., Jr. Pathogenesis of metastasis formation observed in vivo in the rabbit ear chamber. *AMA Arch Pathol* **66**, 550-568 (1958).
22. Friedl, P., *et al.* Migration of highly aggressive MV3 melanoma cells in 3-dimensional collagen lattices results in local matrix reorganization and shedding of alpha2 and beta1 integrins and CD44. *Cancer Res* **57**, 2061-2070 (1997).
23. Jacques, T.S., *et al.* Neural precursor cell chain migration and division are regulated through different beta1 integrins. *Development* **125**, 3167-3177 (1998).
24. Teddy, J.M. & Kulesa, P.M. In vivo evidence for short- and long-range cell communication in cranial neural crest cells. *Development* **131**, 6141-6151 (2004).
25. El Fahime, E., Torrente, Y., Caron, N.J., Bresolin, M.D. & Tremblay, J.P. In vivo migration of transplanted myoblasts requires matrix metalloproteinase activity. *Exp Cell Res* **258**, 279-287 (2000).

26. Page, D.L., Anderson, T.J. & Sakamoto, G. *Diagnostic Histopathology of the Breast* (Churchill Livingstone, New York). 219-222 (1987).
27. Pitts, W.C., et al. Carcinomas with metaplasia and sarcomas of the breast. *Am J Clin Pathol* **95**, 623-632 (1991).
28. Sood, A.K., et al. Molecular determinants of ovarian cancer plasticity. *Am J Pathol* **158**, 1279-1288 (2001).
29. Seftor, E.A., et al. Molecular determinants of human uveal melanoma invasion and metastasis. *Clin Exp Metastasis* **19**, 233-246 (2002).
30. Friedl, P. Prespecification and plasticity: shifting mechanisms of cell migration. *Curr Opin Cell Biol* **16**, 14-23 (2004).
31. Montell, D.J. Morphogenetic cell movements: diversity from modular mechanical properties. *Science* **322**, 1502-1505 (2008).
32. Vaughan, R.B. & Trinkaus, J.P. Movements of epithelial cell sheets in vitro. *J Cell Sci* **1**, 407-413 (1966).
33. Ilina, O. & Friedl, P. Mechanisms of collective cell migration at a glance. *J Cell Sci* **122**, 3203-3208 (2009).
34. Carmona-Fontaine, C., et al. Contact inhibition of locomotion in vivo controls neural crest directional migration. *Nature* **456**, 957-961 (2008).
35. Friedl, P., Hegerfeldt, Y. & Tusch, M. Collective cell migration in morphogenesis and cancer. *Int J Dev Biol* **48**, 441-449 (2004).
36. Rorth, P. Collective cell migration. *Annu Rev Cell Dev Biol* **25**, 407-429 (2009).
37. Werner, S., Krieg, T. & Smola, H. Keratinocyte-fibroblast interactions in wound healing. *J Invest Dermatol* **127**, 998-1008 (2007).
38. Hellstrom, M., et al. Dll4 signalling through Notch1 regulates formation of tip cells during angiogenesis. *Nature* **445**, 776-780 (2007).
39. Caussinus, E., Colombelli, J. & Affolter, M. Tip-cell migration controls stalk-cell intercalation during Drosophila tracheal tube elongation. *Curr Biol* **18**, 1727-1734 (2008).
40. Ghabrial, A.S. & Krasnow, M.A. Social interactions among epithelial cells during tracheal branching morphogenesis. *Nature* **441**, 746-749 (2006).
41. Ewald, A.J., Brenot, A., Duong, M., Chan, B.S. & Werb, Z. Collective epithelial migration and cell rearrangements drive mammary branching morphogenesis. *Dev Cell* **14**, 570-581 (2008).
42. Wiseman, B.S. & Werb, Z. Stromal effects on mammary gland development and breast cancer. *Science* **296**, 1046-1049 (2002).
43. Lu, P. & Werb, Z. Patterning mechanisms of branched organs. *Science* **322**, 1506-1509 (2008).
44. Ghysen, A. & Dambly-Chaudiere, C. The lateral line microcosmos. *Genes Dev* **21**, 2118-2130 (2007).
45. Haas, P. & Gilmour, D. Chemokine signaling mediates self-organizing tissue migration in the zebrafish lateral line. *Dev Cell* **10**, 673-680 (2006).
46. David, N.B., et al. Molecular basis of cell migration in the fish lateral line: role of the chemokine receptor CXCR4 and of its ligand, SDF1. *Proc Natl Acad Sci U S A* **99**, 16297-16302 (2002).
47. Rorth, P. Collective guidance of collective cell migration. *Trends Cell Biol* **17**, 575-579 (2007).
48. Fulga, T.A. & Rorth, P. Invasive cell migration is initiated by guided growth of long cellular extensions. *Nat Cell Biol* **4**, 715-719 (2002).
49. Pacquelet, A. & Rorth, P. Regulatory mechanisms required for DE-cadherin function in cell migration and other types of adhesion. *J Cell Biol* **170**, 803-812 (2005).
50. Bianco, A., et al. Two distinct modes of guidance signalling during collective migration of border cells. *Nature* **448**, 362-365 (2007).
51. Friedl, P., et al. Migration of coordinated cell clusters in mesenchymal and epithelial cancer explants in vitro. *Cancer Res* **55**, 4557-4560 (1995).
52. Hegerfeldt, Y., Tusch, M., Bocker, E.B. & Friedl, P. Collective cell movement in primary melanoma explants: plasticity of cell-cell interaction, beta1-integrin function, and migration strategies. *Cancer Res* **62**, 2125-2130 (2002).
53. Nabeshima, K., Inoue, T., Shimao, Y., Kataoka, H. & Koono, M. Cohort migration of carcinoma cells: differentiated colorectal carcinoma cells move as coherent cell clusters or sheets. *Histol Histopathol* **14**, 1183-1197 (1999).
54. Kam, Y., Guess, C., Estrada, L., Weidow, B. & Quaranta, V. A novel circular invasion assay mimics in vivo invasive behavior of cancer cell lines and distinguishes single-cell motility in vitro. *BMC Cancer* **8**, 198 (2008).
55. Wang, F.Q., et al. Lysophosphatidic acid (LPA) effects on endometrial carcinoma in vitro proliferation, invasion, and matrix metalloproteinase activity. *Gynecol Oncol* (2010).

56. Zhu, N., *et al.* Melanoma cell migration is upregulated by tumour necrosis factor-alpha and suppressed by alpha-melanocyte-stimulating hormone. *Br J Cancer* **90**, 1457-1463 (2004).
57. Christiansen, J.J. & Rajasekaran, A.K. Reassessing epithelial to mesenchymal transition as a prerequisite for carcinoma invasion and metastasis. *Cancer Res* **66**, 8319-8326 (2006).
58. Hsu, M., Andl, T., Li, G., Meinkoth, J.L. & Herlyn, M. Cadherin repertoire determines partner-specific gap junctional communication during melanoma progression. *J Cell Sci* **113 (Pt 9)**, 1535-1542 (2000).
59. Radunsky, G.S. & van Golen, K.L. The current understanding of the molecular determinants of inflammatory breast cancer metastasis. *Clin Exp Metastasis* **22**, 615-620 (2005).
60. Lahlou, H., Fanjul, M., Pradayrol, L., Susini, C. & Pyronnet, S. Restoration of functional gap junctions through internal ribosome entry site-dependent synthesis of endogenous connexins in density-inhibited cancer cells. *Mol Cell Biol* **25**, 4034-4045 (2005).
61. Daly, A.J., McIlreavey, L. & Irwin, C.R. Regulation of HGF and SDF-1 expression by oral fibroblasts--implications for invasion of oral cancer. *Oral Oncol* **44**, 646-651 (2008).
62. Czyz, J. The stage-specific function of gap junctions during tumourigenesis. *Cell Mol Biol Lett* **13**, 92-102 (2008).
63. Nabeshima, K., *et al.* Front-cell-specific expression of membrane-type 1 matrix metalloproteinase and gelatinase A during cohort migration of colon carcinoma cells induced by hepatocyte growth factor/scatter factor. *Cancer Res* **60**, 3364-3369 (2000).
64. Wells, A., Yates, C. & Shepard, C.R. E-cadherin as an indicator of mesenchymal to epithelial reverting transitions during the metastatic seeding of disseminated carcinomas. *Clin Exp Metastasis* **25**, 621-628 (2008).
65. Hugo, H., *et al.* Epithelial--mesenchymal and mesenchymal--epithelial transitions in carcinoma progression. *J Cell Physiol* **213**, 374-383 (2007).
66. Sahai, E. & Marshall, C.J. Differing modes of tumour cell invasion have distinct requirements for Rho/ROCK signalling and extracellular proteolysis. *Nat Cell Biol* **5**, 711-719 (2003).
67. Harley, B.A., *et al.* Microarchitecture of three-dimensional scaffolds influences cell migration behavior via junction interactions. *Biophys J* **95**, 4013-4024 (2008).
68. Lo, C.M., Wang, H.B., Dembo, M. & Wang, Y.L. Cell movement is guided by the rigidity of the substrate. *Biophys J* **79**, 144-152 (2000).
69. Takada, Y., Ye, X. & Simon, S. The integrins. *Genome Biol* **8**, 215 (2007).
70. Hynes, R.O. Integrins: versatility, modulation, and signaling in cell adhesion. *Cell* **69**, 11-25 (1992).
71. Giancotti, F.G. & Ruoslahti, E. Integrin signaling. *Science* **285**, 1028-1032 (1999).
72. Amano, M., *et al.* Formation of actin stress fibers and focal adhesions enhanced by Rho-kinase. *Science* **275**, 1308-1311 (1997).
73. Keely, P.J., Westwick, J.K., Whitehead, I.P., Der, C.J. & Parise, L.V. Cdc42 and Rac1 induce integrin-mediated cell motility and invasiveness through PI(3)K. *Nature* **390**, 632-636 (1997).
74. Nobes, C.D. & Hall, A. Rho, rac, and cdc42 GTPases regulate the assembly of multimolecular focal complexes associated with actin stress fibers, lamellipodia, and filopodia. *Cell* **81**, 53-62 (1995).
75. Trikha, M., *et al.* The high affinity alphaIIb beta3 integrin is involved in invasion of human melanoma cells. *Cancer Res* **57**, 2522-2528 (1997).
76. Strobel, T. & Cannistra, S.A. Beta1-integrins partly mediate binding of ovarian cancer cells to peritoneal mesothelium in vitro. *Gynecol Oncol* **73**, 362-367 (1999).
77. Zutter, M.M., Santoro, S.A., Staatz, W.D. & Tsung, Y.L. Re-expression of the alpha 2 beta 1 integrin abrogates the malignant phenotype of breast carcinoma cells. *Proc Natl Acad Sci U S A* **92**, 7411-7415 (1995).
78. Danen, E.H., *et al.* Regulation of integrin-mediated adhesion to laminin and collagen in human melanocytes and in non-metastatic and highly metastatic human melanoma cells. *Int J Cancer* **54**, 315-321 (1993).
79. Fournier, A.K., *et al.* Rac-dependent cyclin D1 gene expression regulated by cadherin- and integrin-mediated adhesion. *J Cell Sci* **121**, 226-233 (2008).
80. Carrano, A.C. & Pagano, M. Role of the F-box protein Skp2 in adhesion-dependent cell cycle progression. *J Cell Biol* **153**, 1381-1390 (2001).
81. Frisch, S.M. & Screaton, R.A. Anoikis mechanisms. *Curr Opin Cell Biol* **13**, 555-562 (2001).
82. Desgrosellier, J.S. & Cheresch, D.A. Integrins in cancer: biological implications and therapeutic opportunities. *Nat Rev Cancer* **10**, 9-22 (2010).
83. Shrivastava, A., *et al.* An orphan receptor tyrosine kinase family whose members serve as nonintegrin collagen receptors. *Mol Cell* **1**, 25-34 (1997).
84. Sternlicht, M.D. & Werb, Z. How matrix metalloproteinases regulate cell behavior. *Annu Rev Cell Dev Biol* **17**, 463-516 (2001).

85. Ellerbroek, S.M., Wu, Y.I., Overall, C.M. & Stack, M.S. Functional interplay between type I collagen and cell surface matrix metalloproteinase activity. *J Biol Chem* **276**, 24833-24842 (2001).
86. Galvez, B.G., Matias-Roman, S., Yanez-Mo, M., Sanchez-Madrid, F. & Arroyo, A.G. ECM regulates MT1-MMP localization with beta1 or alphavbeta3 integrins at distinct cell compartments modulating its internalization and activity on human endothelial cells. *J Cell Biol* **159**, 509-521 (2002).
87. Friedl, P. & Wolf, K. Proteolytic and non-proteolytic migration of tumour cells and leucocytes. *Biochem Soc Symp*, 277-285 (2003).
88. Deryugina, E.I., Bourdon, M.A., Reisfeld, R.A. & Strongin, A. Remodeling of collagen matrix by human tumor cells requires activation and cell surface association of matrix metalloproteinase-2. *Cancer Res* **58**, 3743-3750 (1998).
89. Koblinski, J.E., Ahram, M. & Sloane, B.F. Unraveling the role of proteases in cancer. *Clin Chim Acta* **291**, 113-135 (2000).
90. Hotary, K., Allen, E., Punturieri, A., Yana, I. & Weiss, S.J. Regulation of cell invasion and morphogenesis in a three-dimensional type I collagen matrix by membrane-type matrix metalloproteinases 1, 2, and 3. *J Cell Biol* **149**, 1309-1323 (2000).
91. Maekawa, K., Sato, H., Furukawa, M. & Yoshizaki, T. Inhibition of cervical lymph node metastasis by marimastat (BB-2516) in an orthotopic oral squamous cell carcinoma implantation model. *Clin Exp Metastasis* **19**, 513-518 (2002).
92. Wang, X., Fu, X., Brown, P.D., Crimmin, M.J. & Hoffman, R.M. Matrix metalloproteinase inhibitor BB-94 (batimastat) inhibits human colon tumor growth and spread in a patient-like orthotopic model in nude mice. *Cancer Res* **54**, 4726-4728 (1994).
93. Wolf, K., *et al.* Collagen-based cell migration models in vitro and in vivo. *Semin Cell Dev Biol* **20**, 931-941 (2009).
94. Hotary, K.B., *et al.* Membrane type I matrix metalloproteinase usurps tumor growth control imposed by the three-dimensional extracellular matrix. *Cell* **114**, 33-45 (2003).
95. Kruger, A., *et al.* Hydroxamate-type matrix metalloproteinase inhibitor batimastat promotes liver metastasis. *Cancer Res* **61**, 1272-1275 (2001).
96. Della Porta, P., *et al.* Combined treatment with serine protease inhibitor aprotinin and matrix metalloproteinase inhibitor Batimastat (BB-94) does not prevent invasion of human esophageal and ovarian carcinoma cells in vivo. *Anticancer Res* **19**, 3809-3816 (1999).
97. Overall, C.M. & Lopez-Otin, C. Strategies for MMP inhibition in cancer: innovations for the post-trial era. *Nat Rev Cancer* **2**, 657-672 (2002).
98. Goswami, S., *et al.* Macrophages promote the invasion of breast carcinoma cells via a colony-stimulating factor-1/epidermal growth factor paracrine loop. *Cancer Res* **65**, 5278-5283 (2005).
99. Wyckoff, J., *et al.* A paracrine loop between tumor cells and macrophages is required for tumor cell migration in mammary tumors. *Cancer Res* **64**, 7022-7029 (2004).
100. Sutherland, D., Samakovlis, C. & Krasnow, M.A. branchless encodes a Drosophila FGF homolog that controls tracheal cell migration and the pattern of branching. *Cell* **87**, 1091-1101 (1996).
101. Nomura, S., *et al.* FGF10/FGFR2 signal induces cell migration and invasion in pancreatic cancer. *Br J Cancer* **99**, 305-313 (2008).
102. Kuperwasser, C., *et al.* Reconstruction of functionally normal and malignant human breast tissues in mice. *Proc Natl Acad Sci U S A* **101**, 4966-4971 (2004).
103. Birchmeier, C. & Gherardi, E. Developmental roles of HGF/SF and its receptor, the c-Met tyrosine kinase. *Trends Cell Biol* **8**, 404-410 (1998).
104. Matsumoto, K., Date, K., Shimura, H. & Nakamura, T. Acquisition of invasive phenotype in gallbladder cancer cells via mutual interaction of stromal fibroblasts and cancer cells as mediated by hepatocyte growth factor. *Jpn J Cancer Res* **87**, 702-710 (1996).
105. Nakamura, T., Matsumoto, K., Kiritoshi, A. & Tano, Y. Induction of hepatocyte growth factor in fibroblasts by tumor-derived factors affects invasive growth of tumor cells: in vitro analysis of tumor-stromal interactions. *Cancer Res* **57**, 3305-3313 (1997).
106. Date, K., *et al.* Inhibition of tumor growth and invasion by a four-kringle antagonist (HGF/NK4) for hepatocyte growth factor. *Oncogene* **17**, 3045-3054 (1998).
107. Matsumoto, K., Nakamura, T. & Kramer, R.H. Hepatocyte growth factor/scatter factor induces tyrosine phosphorylation of focal adhesion kinase (p125FAK) and promotes migration and invasion by oral squamous cell carcinoma cells. *J Biol Chem* **269**, 31807-31813 (1994).
108. Allinen, M., *et al.* Molecular characterization of the tumor microenvironment in breast cancer. *Cancer Cell* **6**, 17-32 (2004).
109. Rogers, S.J., Harrington, K.J., Rhys-Evans, P., P, O.C. & Eccles, S.A. Biological significance of c-erbB family oncogenes in head and neck cancer. *Cancer Metastasis Rev* **24**, 47-69 (2005).

110. Turner, N. & Grose, R. Fibroblast growth factor signalling: from development to cancer. *Nat Rev Cancer* **10**, 116-129 (2010).
111. Lehmann, K., *et al.* Raf induces TGFbeta production while blocking its apoptotic but not invasive responses: a mechanism leading to increased malignancy in epithelial cells. *Genes Dev* **14**, 2610-2622 (2000).
112. Rahimi, R.A. & Leof, E.B. TGF-beta signaling: a tale of two responses. *J Cell Biochem* **102**, 593-608 (2007).
113. Streuli, C.H. & Akhtar, N. Signal co-operation between integrins and other receptor systems. *Biochem J* **418**, 491-506 (2009).
114. Busillo, J.M. & Benovic, J.L. Regulation of CXCR4 signaling. *Biochim Biophys Acta* **1768**, 952-963 (2007).
115. Engl, T., *et al.* CXCR4 chemokine receptor mediates prostate tumor cell adhesion through alpha5 and beta3 integrins. *Neoplasia* **8**, 290-301 (2006).
116. Sun, Y.X., *et al.* Expression and activation of alpha v beta 3 integrins by SDF-1/CXC12 increases the aggressiveness of prostate cancer cells. *Prostate* **67**, 61-73 (2007).
117. Grzesiak, J.J., Smith, K.C., Burton, D.W., Deftos, L.J. & Bouvet, M. Integrin-mediated laminin-1 adhesion upregulates CXCR4 and IL-8 expression in pancreatic cancer cells. *Surgery* **141**, 804-814 (2007).
118. Tsutsumi, S., Gupta, S.K., Hogan, V., Collard, J.G. & Raz, A. Activation of small GTPase Rho is required for autocrine motility factor signaling. *Cancer Res* **62**, 4484-4490 (2002).
119. Funasaka, T. & Raz, A. The role of autocrine motility factor in tumor and tumor microenvironment. *Cancer Metastasis Rev* **26**, 725-735 (2007).
120. Lazar-Molnar, E., Hegyesi, H., Toth, S. & Falus, A. Autocrine and paracrine regulation by cytokines and growth factors in melanoma. *Cytokine* **12**, 547-554 (2000).
121. Leivonen, S.K. & Kahari, V.M. Transforming growth factor-beta signaling in cancer invasion and metastasis. *Int J Cancer* **121**, 2119-2124 (2007).
122. Mercurio, A.M., Bachelder, R.E., Bates, R.C. & Chung, J. Autocrine signaling in carcinoma: VEGF and the alpha6beta4 integrin. *Semin Cancer Biol* **14**, 115-122 (2004).
123. Lehembre, F., *et al.* NCAM-induced focal adhesion assembly: a functional switch upon loss of E-cadherin. *EMBO J* **27**, 2603-2615 (2008).
124. Chu, Y.S., *et al.* Force measurements in E-cadherin-mediated cell doublets reveal rapid adhesion strengthened by actin cytoskeleton remodeling through Rac and Cdc42. *J Cell Biol* **167**, 1183-1194 (2004).
125. Chidgey, M. & Dawson, C. Desmosomes: a role in cancer? *Br J Cancer* **96**, 1783-1787 (2007).
126. Lee, J.M., Dedhar, S., Kalluri, R. & Thompson, E.W. The epithelial-mesenchymal transition: new insights in signaling, development, and disease. *J Cell Biol* **172**, 973-981 (2006).
127. Khan, K., *et al.* Desmocollin switching in colorectal cancer. *Br J Cancer* **95**, 1367-1370 (2006).
128. Langbein, L., *et al.* Tight junction-related structures in the absence of a lumen: occludin, claudins and tight junction plaque proteins in densely packed cell formations of stratified epithelia and squamous cell carcinomas. *Eur J Cell Biol* **82**, 385-400 (2003).
129. Smalley, K.S., *et al.* Up-regulated expression of zonula occludens protein-1 in human melanoma associates with N-cadherin and contributes to invasion and adhesion. *Am J Pathol* **166**, 1541-1554 (2005).
130. Ito, A., *et al.* Increased expression of connexin 26 in the invasive component of lung squamous cell carcinoma: significant correlation with poor prognosis. *Cancer Lett* **234**, 239-248 (2006).
131. Casey, R.C., *et al.* Beta 1-integrins regulate the formation and adhesion of ovarian carcinoma multicellular spheroids. *Am J Pathol* **159**, 2071-2080 (2001).
132. Salmenpera, P., *et al.* Formation and activation of fibroblast spheroids depend on fibronectin-integrin interaction. *Exp Cell Res* **314**, 3444-3452 (2008).
133. Valcarcel, M., *et al.* Three-dimensional growth as multicellular spheroid activates the proangiogenic phenotype of colorectal carcinoma cells via LFA-1-dependent VEGF: implications on hepatic micrometastasis. *J Transl Med* **6**, 57 (2008).
134. Vitorino, P. & Meyer, T. Modular control of endothelial sheet migration. *Genes Dev* **22**, 3268-3281 (2008).
135. Boyden, S. The chemotactic effect of mixtures of antibody and antigen on polymorphonuclear leucocytes. *J Exp Med* **115**, 453-466 (1962).
136. Kleinman, H.K. & Jacob, K. Invasion assays. *Curr Protoc Cell Biol* **Chapter 12**, Unit 12 12 (2001).
137. Lamb, R.F., *et al.* AP-1-mediated invasion requires increased expression of the hyaluronan receptor CD44. *Mol Cell Biol* **17**, 963-976 (1997).

138. Schoumacher, M., Goldman, R.D., Louvard, D. & Vignjevic, D. Filopodial actin machinery cooperates with microtubules and vimentin in the elongation of invadopodia. *J. Cell Biol* (accepted).
139. Schindler, M., *et al.* Living in three dimensions: 3D nanostructured environments for cell culture and regenerative medicine. *Cell Biochem Biophys* **45**, 215-227 (2006).
140. Smalley, K.S., Lioni, M. & Herlyn, M. Life isn't flat: taking cancer biology to the next dimension. *In Vitro Cell Dev Biol Anim* **42**, 242-247 (2006).
141. Berking, C. & Herlyn, M. Human skin reconstruct models: a new application for studies of melanocyte and melanoma biology. *Histol Histopathol* **16**, 669-674 (2001).
142. Lo, R.S. & Witte, O.N. Transforming growth factor-beta activation promotes genetic context-dependent invasion of immortalized melanocytes. *Cancer Res* **68**, 4248-4257 (2008).
143. Meier, F., *et al.* Human melanoma progression in skin reconstructs : biological significance of bFGF. *Am J Pathol* **156**, 193-200 (2000).
144. Andresen, V., *et al.* Infrared multiphoton microscopy: subcellular-resolved deep tissue imaging. *Curr Opin Biotechnol* **20**, 54-62 (2009).
145. Gordley, K., Cole, P., Hicks, J. & Hollier, L. A comparative, long term assessment of soft tissue substitutes: AlloDerm, Enduragen, and Dermamatrix. *J Plast Reconstr Aesthet Surg* **62**, 849-850 (2009).
146. Carragher, N.O. Profiling distinct mechanisms of tumour invasion for drug discovery: imaging adhesion, signalling and matrix turnover. *Clin Exp Metastasis* **26**, 381-397 (2009).
147. Friedl, P. & Brocker, E.B. Reconstructing leukocyte migration in 3D extracellular matrix by time-lapse videomicroscopy and computer-assisted tracking. *Methods Mol Biol* **239**, 77-90 (2004).
148. Brown, E.B., *et al.* In vivo measurement of gene expression, angiogenesis and physiological function in tumors using multiphoton laser scanning microscopy. *Nat Med* **7**, 864-868 (2001).
149. Gaggioli, C., *et al.* Fibroblast-led collective invasion of carcinoma cells with differing roles for RhoGTPases in leading and following cells. *Nat Cell Biol* **9**, 1392-1400 (2007).
150. Nakamura, T., Fidler, I.J. & Coombes, K.R. Gene expression profile of metastatic human pancreatic cancer cells depends on the organ microenvironment. *Cancer Res* **67**, 139-148 (2007).
151. Waerner, T., *et al.* ILEI: a cytokine essential for EMT, tumor formation, and late events in metastasis in epithelial cells. *Cancer Cell* **10**, 227-239 (2006).
152. Wicki, A., *et al.* Tumor invasion in the absence of epithelial-mesenchymal transition: podoplanin-mediated remodeling of the actin cytoskeleton. *Cancer Cell* **9**, 261-272 (2006).
153. Wakelin, M.W., *et al.* An anti-platelet-endothelial cell adhesion molecule-1 antibody inhibits leukocyte extravasation from mesenteric microvessels in vivo by blocking the passage through the basement membrane. *J Exp Med* **184**, 229-239 (1996).
154. Mempel, T.R., Moser, C., Hutter, J., Kuebler, W.M. & Krombach, F. Visualization of leukocyte transendothelial and interstitial migration using reflected light oblique transillumination in intravital video microscopy. *J Vasc Res* **40**, 435-441 (2003).
155. Wang, W., *et al.* Single cell behavior in metastatic primary mammary tumors correlated with gene expression patterns revealed by molecular profiling. *Cancer Res* **62**, 6278-6288 (2002).
156. Yamauchi, K., *et al.* Real-time in vivo dual-color imaging of intracapillary cancer cell and nucleus deformation and migration. *Cancer Res* **65**, 4246-4252 (2005).
157. Koehl, G.E., Gaumann, A. & Geissler, E.K. Intravital microscopy of tumor angiogenesis and regression in the dorsal skin fold chamber: mechanistic insights and preclinical testing of therapeutic strategies. *Clin Exp Metastasis* **26**, 329-344 (2009).
158. Mostany, R. & Portera-Cailliau, C. A method for 2-photon imaging of blood flow in the neocortex through a cranial window. *J Vis Exp* (2008).
159. Goldbrunner, R.H., Bendszus, M. & Tonn, J.C. Models for angiogenesis in gliomas. *Cancer Treat Res* **117**, 115-135 (2004).
160. Kienast, Y., *et al.* Real-time imaging reveals the single steps of brain metastasis formation. *Nat Med* **16**, 116-122 (2010).
161. Shan, S., Sorg, B. & Dewhirst, M.W. A novel rodent mammary window of orthotopic breast cancer for intravital microscopy. *Microvasc Res* **65**, 109-117 (2003).
162. Kedrin, D., *et al.* Intravital imaging of metastatic behavior through a mammary imaging window. *Nat Methods* **5**, 1019-1021 (2008).
163. Asaishi, K., Endrich, B., Gotz, A. & Messmer, K. Quantitative analysis of microvascular structure and function in the amelanotic melanoma A-Mel-3. *Cancer Res* **41**, 1898-1904 (1981).
164. Boucher, Y., Leunig, M. & Jain, R.K. Tumor angiogenesis and interstitial hypertension. *Cancer Res* **56**, 4264-4266 (1996).

165. Leunig, M., *et al.* Angiogenesis, microvascular architecture, microhemodynamics, and interstitial fluid pressure during early growth of human adenocarcinoma LS174T in SCID mice. *Cancer Res* **52**, 6553-6560 (1992).
166. Reyes-Aldasoro, C.C., *et al.* Estimation of apparent tumor vascular permeability from multiphoton fluorescence microscopic images of P22 rat sarcomas in vivo. *Microcirculation* **15**, 65-79 (2008).
167. Guba, M., *et al.* Rapamycin inhibits primary and metastatic tumor growth by antiangiogenesis: involvement of vascular endothelial growth factor. *Nat Med* **8**, 128-135 (2002).
168. Vajkoczy, P., *et al.* Glioma cell migration is associated with glioma-induced angiogenesis in vivo. *Int J Dev Neurosci* **17**, 557-563 (1999).
169. Hansen-Algenstaedt, N., *et al.* Femur window--a new approach to microcirculation of living bone in situ. *J Orthop Res* **23**, 1073-1082 (2005).
170. Bertera, S., *et al.* Body window-enabled in vivo multicolor imaging of transplanted mouse islets expressing an insulin-Timer fusion protein. *Biotechniques* **35**, 718-722 (2003).
171. Oye, K.S., *et al.* A novel method for mapping the heterogeneity in blood supply to normal and malignant tissues in the mouse dorsal window chamber. *Microvasc Res* **75**, 179-187 (2008).
172. Griffin, R.J., *et al.* Use of a fluorescently labeled poly-caspase inhibitor for in vivo detection of apoptosis related to vascular-targeting agent arsenic trioxide for cancer therapy. *Technol Cancer Res Treat* **6**, 651-654 (2007).
173. Condeelis, J. & Segall, J.E. Intravital imaging of cell movement in tumours. *Nat Rev Cancer* **3**, 921-930 (2003).
174. Crepel, V., *et al.* A parturition-associated nonsynaptic coherent activity pattern in the developing hippocampus. *Neuron* **54**, 105-120 (2007).
175. Helmchen, F. & Denk, W. Deep tissue two-photon microscopy. *Nat Methods* **2**, 932-940 (2005).
176. Deryugina, E.I. & Quigley, J.P. Chick embryo chorioallantoic membrane model systems to study and visualize human tumor cell metastasis. *Histochem Cell Biol* **130**, 1119-1130 (2008).
177. Hasegawa, S., Maruyama, K., Takenaka, H., Furukawa, T. & Saga, T. A medaka model of cancer allowing direct observation of transplanted tumor cells in vivo at a cellular-level resolution. *Proc Natl Acad Sci U S A* **106**, 13832-13837 (2009).
178. Marques, I.J., *et al.* Metastatic behaviour of primary human tumours in a zebrafish xenotransplantation model. *BMC Cancer* **9**, 128 (2009).
179. Stoletov, K., Montel, V., Lester, R.D., Gonias, S.L. & Klemke, R. High-resolution imaging of the dynamic tumor cell vascular interface in transparent zebrafish. *Proc Natl Acad Sci U S A* **104**, 17406-17411 (2007).
180. Rodriguez, C., Barriuso, V. & Chan, L.S. Extensive basal cell carcinoma with probable bone metastasis. *Cutis* **80**, 60-66 (2007).
181. Frank, S., *et al.* Metastatic glioblastoma cells use common pathways via blood and lymphatic vessels. *Neurol Neurochir Pol* **43**, 183-190 (2009).
182. Fahn, W. & Issels, R.D. Emerging treatments for soft tissue sarcoma of adults. *Expert Opin Emerg Drugs* **9**, 313-334 (2004).
183. Hanada, M., *et al.* Focal adhesion kinase is activated in invading fibrosarcoma cells and regulates metastasis. *Clin Exp Metastasis* **22**, 485-494 (2005).
184. Tomimaru, Y., *et al.* Sclerosing epithelioid fibrosarcoma of the liver infiltrating the inferior vena cava. *World J Gastroenterol* **15**, 4204-4208 (2009).
185. Kim, A., *et al.* Suppression of NF-kappaB activity by NDRG2 expression attenuates the invasive potential of highly malignant tumor cells. *Carcinogenesis* **30**, 927-936 (2009).
186. Carragher, N.O., *et al.* Calpain 2 and Src dependence distinguishes mesenchymal and amoeboid modes of tumour cell invasion: a link to integrin function. *Oncogene* **25**, 5726-5740 (2006).
187. Guo, Y., *et al.* Frzb, a secreted Wnt antagonist, decreases growth and invasiveness of fibrosarcoma cells associated with inhibition of Met signaling. *Cancer Res* **68**, 3350-3360 (2008).
188. Hofmann, U.B., Westphal, J.R., Van Muijen, G.N. & Ruitter, D.J. Matrix metalloproteinases in human melanoma. *J Invest Dermatol* **115**, 337-344 (2000).
189. Agarwala, S.S. & Kirkwood, J.M. Update on adjuvant interferon therapy for high-risk melanoma. *Oncology (Williston Park)* **16**, 1177-1187; discussion 1190-1172, 1197 (2002).
190. Breslow, A. Thickness, cross-sectional areas and depth of invasion in the prognosis of cutaneous melanoma. *Ann Surg* **172**, 902-908 (1970).
191. Clark, W.H., Jr., From, L., Bernardino, E.A. & Mihm, M.C. The histogenesis and biologic behavior of primary human malignant melanomas of the skin. *Cancer Res* **29**, 705-727 (1969).

192. Reed, R.J. & Martin, P. Variants of melanoma. *Semin Cutan Med Surg* **16**, 137-158 (1997).
193. James, W.D. & Berger, T.G. Andrew's Diseases of the Skin: Clinical Dermatology. *Saunders Elsevier* (2006).
194. Trikha, M., *et al.* CNTO 95, a fully human monoclonal antibody that inhibits alphav integrins, has antitumor and antiangiogenic activity in vivo. *Int J Cancer* **110**, 326-335 (2004).
195. Wilkinson, D.G. Multiple roles of EPH receptors and ephrins in neural development. *Nat Rev Neurosci* **2**, 155-164 (2001).
196. Yancopoulos, G.D., *et al.* Vascular-specific growth factors and blood vessel formation. *Nature* **407**, 242-248 (2000).
197. Meyer, S., *et al.* Ephrin-B2 overexpression enhances integrin-mediated ECM-attachment and migration of B16 melanoma cells. *Int J Oncol* **27**, 1197-1206 (2005).
198. Shields, J.D., *et al.* Chemokine-mediated migration of melanoma cells towards lymphatics-- a mechanism contributing to metastasis. *Oncogene* **26**, 2997-3005 (2007).
199. Li, L., Dragulev, B., Zigrino, P., Mauch, C. & Fox, J.W. The invasive potential of human melanoma cell lines correlates with their ability to alter fibroblast gene expression in vitro and the stromal microenvironment in vivo. *Int J Cancer* **125**, 1796-1804 (2009).
200. Theer, P., Hasan, M.T. & Denk, W. Two-photon imaging to a depth of 1000 microm in living brains by use of a Ti:Al₂O₃ regenerative amplifier. *Opt Lett* **28**, 1022-1024 (2003).
201. Denk, W., Strickler, J.H. & Webb, W.W. Two-photon laser scanning fluorescence microscopy. *Science* **248**, 73-76 (1990).
202. Friedl, P., Wolf, K., von Andrian, U.H. & Harms, G. Biological second and third harmonic generation microscopy. *Curr Protoc Cell Biol* **Chapter 4**, Unit 4 15 (2007).
203. Zipfel, W.R., *et al.* Live tissue intrinsic emission microscopy using multiphoton-excited native fluorescence and second harmonic generation. *Proc Natl Acad Sci U S A* **100**, 7075-7080 (2003).
204. Zoumi, A., Yeh, A. & Tromberg, B.J. Imaging cells and extracellular matrix in vivo by using second-harmonic generation and two-photon excited fluorescence. *Proc Natl Acad Sci U S A* **99**, 11014-11019 (2002).
205. Konig, K. Multiphoton microscopy in life sciences. *J Microsc* **200**, 83-104 (2000).
206. Masters, B.R., So, P.T. & Gratton, E. Multiphoton excitation fluorescence microscopy and spectroscopy of in vivo human skin. *Biophys J* **72**, 2405-2412 (1997).
207. Rothstein, E.C., Carroll, S., Combs, C.A., Jobsis, P.D. & Balaban, R.S. Skeletal muscle NAD(P)H two-photon fluorescence microscopy in vivo: topology and optical inner filters. *Biophys J* **88**, 2165-2176 (2005).
208. Niesner, R., Andresen, V., Neumann, J., Spiecker, H. & Gunzer, M. The power of single and multibeam two-photon microscopy for high-resolution and high-speed deep tissue and intravital imaging. *Biophys J* **93**, 2519-2529 (2007).
209. Yamamoto, N., *et al.* Cellular dynamics visualized in live cells in vitro and in vivo by differential dual-color nuclear-cytoplasmic fluorescent-protein expression. *Cancer Res* **64**, 4251-4256 (2004).
210. Dickinson, M.E., Simbuerger, E., Zimmermann, B., Waters, C.W. & Fraser, S.E. Multiphoton excitation spectra in biological samples. *J Biomed Opt* **8**, 329-338 (2003).
211. Eggeling, C., Volkmer, A. & Seidel, C.A. Molecular photobleaching kinetics of Rhodamine 6G by one- and two-photon induced confocal fluorescence microscopy. *Chemphyschem* **6**, 791-804 (2005).
212. Haleand, G. & Querry, M. Optical constants of water in the 200-nm to 200- μ m wavelength region. *Appl Opt* **12**, 555-563 (1973).
213. Sipos, E.P., Tamargo, R.J., Weingart, J.D. & Brem, H. Inhibition of tumor angiogenesis. *Ann N Y Acad Sci* **732**, 263-272 (1994).
214. Fogal, V., Zhang, L., Krajewski, S. & Ruoslahti, E. Mitochondrial/cell-surface protein p32/gC1qR as a molecular target in tumor cells and tumor stroma. *Cancer Res* **68**, 7210-7218 (2008).
215. Tseng, S.H., Bargo, P., Durkin, A. & Kollias, N. Chromophore concentrations, absorption and scattering properties of human skin in-vivo. *Opt Express* **17**, 14599-14617 (2009).
216. Masters, B.R., *et al.* Mitigating thermal mechanical damage potential during two-photon dermal imaging. *J Biomed Opt* **9**, 1265-1270 (2004).
217. Moeller, B.J., Cao, Y., Li, C.Y. & Dewhirst, M.W. Radiation activates HIF-1 to regulate vascular radiosensitivity in tumors: role of reoxygenation, free radicals, and stress granules. *Cancer Cell* **5**, 429-441 (2004).
218. Hunter, A., Hendrikse, A., Renan, M. & Abratt, R. Does the tumor microenvironment influence radiation-induced apoptosis? *Apoptosis* **11**, 1727-1735 (2006).
219. Nakanishi, M., Shimada, M. & Niida, H. Genetic instability in cancer cells by impaired cell cycle checkpoints. *Cancer Sci* **97**, 984-989 (2006).

220. Tredan, O., Galmarini, C.M., Patel, K. & Tannock, I.F. Drug resistance and the solid tumor microenvironment. *J Natl Cancer Inst* **99**, 1441-1454 (2007).
221. Jenrette, J.M. Malignant melanoma: the role of radiation therapy revisited. *Semin Oncol* **23**, 759-762 (1996).
222. Duchek, P. & Rorth, P. Guidance of cell migration by EGF receptor signaling during *Drosophila* oogenesis. *Science* **291**, 131-133 (2001).
223. Feng, F.Y., *et al.* Effect of epidermal growth factor receptor inhibitor class in the treatment of head and neck cancer with concurrent radiochemotherapy in vivo. *Clin Cancer Res* **13**, 2512-2518 (2007).
224. Ren, W., *et al.* Epidermal growth factor receptor blockade in combination with conventional chemotherapy inhibits soft tissue sarcoma cell growth in vitro and in vivo. *Clin Cancer Res* **14**, 2785-2795 (2008).
225. Yamada, K.M., *et al.* Monoclonal antibody and synthetic peptide inhibitors of human tumor cell migration. *Cancer Res* **50**, 4485-4496 (1990).
226. Park, C.C., Zhang, H.J., Yao, E.S., Park, C.J. & Bissell, M.J. Beta1 integrin inhibition dramatically enhances radiotherapy efficacy in human breast cancer xenografts. *Cancer Res* **68**, 4398-4405 (2008).
227. Liu, Y., *et al.* The roles of platelet GPIIb/IIIa and alphavbeta3 integrins during HeLa cells adhesion, migration, and invasion to monolayer endothelium under static and dynamic shear flow. *J Biomed Biotechnol* **2009**, 829243 (2009).
228. Ning, S., Nemeth, J.A., Hanson, R.L., Forsythe, K. & Knox, S.J. Anti-integrin monoclonal antibody CNTO 95 enhances the therapeutic efficacy of fractionated radiation therapy in vivo. *Mol Cancer Ther* **7**, 1569-1578 (2008).
229. Park, C.C., *et al.* Beta1 integrin inhibitory antibody induces apoptosis of breast cancer cells, inhibits growth, and distinguishes malignant from normal phenotype in three dimensional cultures and in vivo. *Cancer Res* **66**, 1526-1535 (2006).
230. Hardee, M.E., *et al.* Erythropoietin blockade inhibits the induction of tumor angiogenesis and progression. *PLoS One* **2**, e549 (2007).
231. Boccaccio, C. & Comoglio, P.M. Invasive growth: a MET-driven genetic programme for cancer and stem cells. *Nat Rev Cancer* **6**, 637-645 (2006).
232. Giampieri, S., *et al.* Localized and reversible TGFbeta signalling switches breast cancer cells from cohesive to single cell motility. *Nat Cell Biol* **11**, 1287-1296 (2009).
233. Coombs, V.A., Nissen, B.K., Marks, R. & Morris, A. The influence of temperature on epidermal cell migration in vitro. *Br J Exp Pathol* **54**, 673-677 (1973).
234. Komuro, H., Yacubova, E. & Rakic, P. Mode and tempo of tangential cell migration in the cerebellar external granular layer. *J Neurosci* **21**, 527-540 (2001).
235. McKinnell, R.G. & Carlson, D.L. Lucke renal adenocarcinoma, an anuran neoplasm: studies at the interface of pathology, virology, and differentiation competence. *J Cell Physiol* **173**, 115-118 (1997).
236. Westermann, S., Vollmar, B., Thorlacius, H. & Menger, M.D. Surface cooling inhibits tumor necrosis factor-alpha-induced microvascular perfusion failure, leukocyte adhesion, and apoptosis in the striated muscle. *Surgery* **126**, 881-889 (1999).
237. Gentile, A., *et al.* Met-driven invasive growth involves transcriptional regulation of Arhgap12. *Oncogene* (2008).
238. Lugassy, C., *et al.* Angiotropism of human prostate cancer cells: implications for extravascular migratory metastasis. *BJU Int* **95**, 1099-1103 (2005).
239. Lugassy, C. & Barnhill, R.L. Angiotropic melanoma and extravascular migratory metastasis: a review. *Adv Anat Pathol* **14**, 195-201 (2007).
240. Holash, J., Wiegand, S.J. & Yancopoulos, G.D. New model of tumor angiogenesis: dynamic balance between vessel regression and growth mediated by angiopoietins and VEGF. *Oncogene* **18**, 5356-5362 (1999).
241. Lugassy, C., Kleinman, H.K., Vernon, S.E., Welch, D.R. & Barnhill, R.L. C16 laminin peptide increases angiotropic extravascular migration of human melanoma cells in a shell-less chick chorioallantoic membrane assay. *Br J Dermatol* **157**, 780-782 (2007).
242. Ryschich, E., *et al.* Promotion of tumor cell migration by extracellular matrix proteins in human pancreatic cancer. *Pancreas* **38**, 804-810 (2009).
243. Winkler, F., *et al.* Imaging glioma cell invasion in vivo reveals mechanisms of dissemination and peritumoral angiogenesis. *Glia* **57**, 1306-1315 (2009).
244. Campbell, T.N. & Robbins, S.M. The Eph receptor/ephrin system: an emerging player in the invasion game. *Curr Issues Mol Biol* **10**, 61-66 (2008).
245. Fuller, T., Korff, T., Kilian, A., Dandekar, G. & Augustin, H.G. Forward EphB4 signaling in endothelial cells controls cellular repulsion and segregation from ephrinB2 positive cells. *J Cell Sci* **116**, 2461-2470 (2003).
246. Kuijper, S., Turner, C.J. & Adams, R.H. Regulation of angiogenesis by Eph-ephrin interactions. *Trends Cardiovasc Med* **17**, 145-151 (2007).

247. Nakada, M., *et al.* The phosphorylation of ephrin-B2 ligand promotes glioma cell migration and invasion. *Int J Cancer* **126**, 1155-1165 (2010).
248. Wang, S., *et al.* Venular basement membranes contain specific matrix protein low expression regions that act as exit points for emigrating neutrophils. *J Exp Med* **203**, 1519-1532 (2006).
249. Vlodavsky, I., *et al.* Extracellular matrix-resident growth factors and enzymes: possible involvement in tumor metastasis and angiogenesis. *Cancer Metastasis Rev* **9**, 203-226 (1990).
250. Colditz, I.G., Schneider, M.A., Pruenster, M. & Rot, A. Chemokines at large: in-vivo mechanisms of their transport, presentation and clearance. *Thromb Haemost* **97**, 688-693 (2007).
251. Siveen, K.S. & Kuttan, G. Role of macrophages in tumour progression. *Immunol Lett* **123**, 97-102 (2009).
252. Huang, E.H., *et al.* A CXCR4 antagonist CTCE-9908 inhibits primary tumor growth and metastasis of breast cancer. *J Surg Res* **155**, 231-236 (2009).
253. Jain, R.K., Munn, L.L. & Fukumura, D. Dissecting tumour pathophysiology using intravital microscopy. *Nat Rev Cancer* **2**, 266-276 (2002).
254. Barnhill, R.L. & Lugassy, C. Angiotropic malignant melanoma and extravascular migratory metastasis: description of 36 cases with emphasis on a new mechanism of tumour spread. *Pathology* **36**, 485-490 (2004).
255. Sahai, E. Illuminating the metastatic process. *Nat Rev Cancer* **7**, 737-749 (2007).
256. Ojalvo, L.S., Whittaker, C.A., Condeelis, J.S. & Pollard, J.W. Gene expression analysis of macrophages that facilitate tumor invasion supports a role for Wnt-signaling in mediating their activity in primary mammary tumors. *J Immunol* **184**, 702-712 (2010).
257. Jain, R.K. Determinants of tumor blood flow: a review. *Cancer Res* **48**, 2641-2658 (1988).
258. Cuenod, C.A., Fournier, L., Balvay, D. & Guinebretiere, J.M. Tumor angiogenesis: pathophysiology and implications for contrast-enhanced MRI and CT assessment. *Abdom Imaging* **31**, 188-193 (2006).
259. Dewhirst, M.W. Relationships between cycling hypoxia, HIF-1, angiogenesis and oxidative stress. *Radiat Res* **172**, 653-665 (2009).
260. Ruan, K., Song, G. & Ouyang, G. Role of hypoxia in the hallmarks of human cancer. *J Cell Biochem* **107**, 1053-1062 (2009).
261. Motoyama, N. & Naka, K. DNA damage tumor suppressor genes and genomic instability. *Curr Opin Genet Dev* **14**, 11-16 (2004).
262. Sandfort, V., Koch, U. & Cordes, N. Cell adhesion-mediated radioresistance revisited. *Int J Radiat Biol* **83**, 727-732 (2007).
263. Cordes, N. & Meineke, V. Cell adhesion-mediated radioresistance (CAM-RR). Extracellular matrix-dependent improvement of cell survival in human tumor and normal cells in vitro. *Strahlenther Onkol* **179**, 337-344 (2003).
264. Westhoff, M.A., Zhou, S., Bachem, M.G., Debatin, K.M. & Fulda, S. Identification of a novel switch in the dominant forms of cell adhesion-mediated drug resistance in glioblastoma cells. *Oncogene* **27**, 5169-5181 (2008).
265. Shain, K.H., *et al.* Beta1 integrin adhesion enhances IL-6-mediated STAT3 signaling in myeloma cells: implications for microenvironment influence on tumor survival and proliferation. *Cancer Res* **69**, 1009-1015 (2009).
266. Hodgkinson, P.S., *et al.* ECM overrides DNA damage-induced cell cycle arrest and apoptosis in small-cell lung cancer cells through beta1 integrin-dependent activation of PI3-kinase. *Cell Death Differ* **13**, 1776-1788 (2006).
267. Sebens Muerkoster, S., *et al.* alpha5-integrin is crucial for L1CAM-mediated chemoresistance in pancreatic adenocarcinoma. *Int J Oncol* **34**, 243-253 (2009).
268. Lewis, J.M., Truong, T.N. & Schwartz, M.A. Integrins regulate the apoptotic response to DNA damage through modulation of p53. *Proc Natl Acad Sci U S A* **99**, 3627-3632 (2002).
269. Holash, J., *et al.* Vessel cooption, regression, and growth in tumors mediated by angiopoietins and VEGF. *Science* **284**, 1994-1998 (1999).
270. Wheeler, D.L., *et al.* Mechanisms of acquired resistance to cetuximab: role of HER (ErbB) family members. *Oncogene* **27**, 3944-3956 (2008).
271. Ruoslahti, E. & Pierschbacher, M.D. New perspectives in cell adhesion: RGD and integrins. *Science* **238**, 491-497 (1987).
272. Ruoslahti, E. Integrin signaling and matrix assembly. *Tumour Biol* **17**, 117-124 (1996).
273. Ilangumaran, S., Borisch, B. & Hoessli, D.C. Signal transduction via CD44: role of plasma membrane microdomains. *Leuk Lymphoma* **35**, 455-469 (1999).
274. Bourguignon, L.Y., Spevak, C.C., Wong, G., Xia, W. & Gilad, E. Hyaluronan-CD44 interaction with protein kinase C(epsilon) promotes oncogenic signaling by the stem cell marker Nanog and the Production of microRNA-21, leading to down-regulation of the tumor

- suppressor protein PDCD4, anti-apoptosis, and chemotherapy resistance in breast tumor cells. *J Biol Chem* **284**, 26533-26546 (2009).
275. Veronesi, U. & Cascinelli, N. Narrow excision (1-cm margin). A safe procedure for thin cutaneous melanoma. *Arch Surg* **126**, 438-441 (1991).
 276. Veronesi, U., *et al.* Thin stage I primary cutaneous malignant melanoma. Comparison of excision with margins of 1 or 3 cm. *N Engl J Med* **318**, 1159-1162 (1988).
 277. Kirkwood, J.M., *et al.* Interferon alfa-2b adjuvant therapy of high-risk resected cutaneous melanoma: the Eastern Cooperative Oncology Group Trial EST 1684. *J Clin Oncol* **14**, 7-17 (1996).
 278. Atkins, M.B., Kunkel, L., Sznol, M. & Rosenberg, S.A. High-dose recombinant interleukin-2 therapy in patients with metastatic melanoma: long-term survival update. *Cancer J Sci Am* **6 Suppl 1**, S11-14 (2000).
 279. Hersey, P., *et al.* A randomized phase 2 study of etaracizumab, a monoclonal antibody against integrin alpha(v)beta(3), +/- dacarbazine in patients with stage IV metastatic melanoma. *Cancer* **116**, 1526-1534 (2010).
 280. Stojadinovic, A., *et al.* Primary adult soft tissue sarcoma: time-dependent influence of prognostic variables. *J Clin Oncol* **20**, 4344-4352 (2002).
 281. Mohrle, M., *et al.* [Prognostic parameters and surgical strategies for facial melanomas]. *J Dtsch Dermatol Ges* **1**, 457-463 (2003).
 282. Robinson, J.K. Use of digital epiluminescence microscopy to help define the edge of lentigo maligna. *Arch Dermatol* **140**, 1095-1100 (2004).
 283. Karakousis, C.P., *et al.* Local recurrence in malignant melanoma: long-term results of the multiinstitutional randomized surgical trial. *Ann Surg Oncol* **3**, 446-452 (1996).
 284. Blouw, B., *et al.* The hypoxic response of tumors is dependent on their microenvironment. *Cancer Cell* **4**, 133-146 (2003).
 285. Ebos, J.M., *et al.* Accelerated metastasis after short-term treatment with a potent inhibitor of tumor angiogenesis. *Cancer Cell* **15**, 232-239 (2009).
 286. Paez-Ribes, M., *et al.* Antiangiogenic therapy elicits malignant progression of tumors to increased local invasion and distant metastasis. *Cancer Cell* **15**, 220-231 (2009).
 287. Glockner, S., Buurman, H., Kleeberger, W., Lehmann, U. & Kreipe, H. Marked intratumoral heterogeneity of c-myc and cyclinD1 but not of c-erbB2 amplification in breast cancer. *Lab Invest* **82**, 1419-1426 (2002).
 288. van Loon, J., *et al.* PET imaging of hypoxia using [(18)F]HX4: a phase I trial. *Eur J Nucl Med Mol Imaging* (2010).
 289. Pistollato, F., *et al.* Intratumoral Hypoxic Gradient Drives Stem Cells Distribution and MGMT Expression in Glioblastoma. *Stem Cells* (2010).
 290. Krug, B., *et al.* Fluor-18-fluorodeoxyglucose positron emission tomography (FDG-PET) in malignant melanoma. Diagnostic comparison with conventional imaging methods. *Acta Radiol* **41**, 446-452 (2000).
 291. Volker, T., *et al.* Positron emission tomography for staging of pediatric sarcoma patients: results of a prospective multicenter trial. *J Clin Oncol* **25**, 5435-5441 (2007).
 292. Board, R.E., *et al.* Detection of BRAF mutations in the tumour and serum of patients enrolled in the AZD6244 (ARRY-142886) advanced melanoma phase II study. *Br J Cancer* **101**, 1724-1730 (2009).
 293. Flaherty, K.T., *et al.* A phase I trial of the oral, multikinase inhibitor sorafenib in combination with carboplatin and paclitaxel. *Clin Cancer Res* **14**, 4836-4842 (2008).
 294. Solit, D.B., *et al.* Phase II trial of 17-allylamino-17-demethoxygeldanamycin in patients with metastatic melanoma. *Clin Cancer Res* **14**, 8302-8307 (2008).
 295. Kissler, S., *et al.* In vivo RNA interference demonstrates a role for Nramp1 in modifying susceptibility to type 1 diabetes. *Nat Genet* **38**, 479-483 (2006).
 296. Laakkonen, P., Porkka, K., Hoffman, J.A. & Ruoslahti, E. A tumor-homing peptide with a targeting specificity related to lymphatic vessels. *Nat Med* **8**, 751-755 (2002).

7 APPENDIX

Abbreviations

Ab/mab	(monoclonal) antibody
ALCAM	Activated leukocyte-cell adhesion molecule
AMF	Autocrine motility factor
BM	Basement membrane
CAM	Chick chorioalloantoic membrane
CAM-DR	Cell-adhesion mediated drugreistance
CAM-RR	Cell-adhesion mediated radioresistance
CCD	Charge-coupled device
CCL/CCR	CC-motif chemokine/receptor
CD	Cluster of differentiation
Cdc42	Cell division control protein 42
Cetux	Cetuximab
c-Met	mesenchymal-epithelial transition factor
CXCL/CXCR	CXC-motif chemokine/receptor
CX3CR1	CX3C-motif chemokine receptor 1
Ctrl	Control
DAPI	4'-6-Diamidino-2-phenylindole
DDR	Discoidin domain receptor
DMEM	Dulbecco's modified eagle medium
DNA	Dioxyribonucleic acid
Doxo	Doxorubicin
DSFC	Dorsal skinfold chamber
E-Cadherin	Epidermal cadherin
ECM	Extracellular matrix
EDTA	Ethylenediaminetetraacetic acid
EGF/EGFR	Epidermal growth factor/EGF receptor
EGFP	Enhanced green fluorescent protein
EMT	Epidermal-to-mesenchymal transition
ERK	Extracellular signal-regulated kinase
FACS	Fluorescence activated cell sorting
FAK	Focal adhesion kinase
FCS	Fetal calf serum
FGF/FGFR	Fibroblast growth factor
FITC	Fluoresceinisothiocyanat
GTPase	Guanosine triphosphate hydrolase
HER	Human epidermal growth factor receptor
HRP	Horse radish peroxidase
H2B	Histone 2B
ICAM	Inter-Cellular Adhesion Molecule 1
IgG	Immunglobulin G
IL	Interleukin
i.p.	Intraperitoneal
IR	Infrared
Irr	Irradiation
<i>ITGB1/ITGB3</i>	Integrin beta 1 or 3 resp. (gene)
i.v.	Intravenous
JNK	c-Jun n-terminal kinase
KGF	Keratincyte growth factor
LSAB	Labeled-Streptavidin-Biotin-Methode
LFA-1	Lymphocyte function-associated antigen 1
L1CAM	L1 (protein) cell adhesion molecule
MAPK	Mitogen-activated protein kinase
MCP-1	Monocyte chemotactic protein-1
MEK	MAPK/ERK kinase

MEM	Minimal essential medium
MET	Mesenchymal-to-epithelial transition
MMP/MT-MMP	Matrix metalloproteinase/membrane type MMP
MPM	Multiphoton microscopy
NF- κ B	Nuclear factor 'kappa-light-chain-enhancer' of activated B-cells
NIR	Near-infrared
OPO	Optical parametric oscillator
PBST	Phosphate-buffered saline tween
PI3K	Phosphoinosid-3-kinase
PMT	Photomultiplier tubes
PVF1	Platelet-derived growth factor- and VEGF-related factor 1
RNA/RNAi	Ribonucleic acid/RNA interference
ROCK	Rho kinase
SCLC	small-cell lung cancer
SDF-1	Stromal cell-derived factor 1
SDS-PAGE	Sodium dodecylsulfate polyacrylamide gel electrophoresis
SHG	Second harmonic generation
shRNA	Short hairpin ribonucleic acid
STS	Soft tissue sarcoma
TAM	Tumor-associated macrophages
TGF β	Transforming growth factor β
Ti:Sa	Titanium:Sapphire (laser)
uPA	Urokinase-type plaminogen activator
UV	Ultraviolet
VE-Cadherin	Vascular endothelial cadherin
VEGF/VEGFR	Vascular endothelial growth factor/VEGF receptor
WB	Western Blot
2D/3D	2-/3-dimensional

Movie legends

Movie 1. Near-infrared multiphoton microscopy of dermal tissue surrounding an HT-1080 dual color xenograft. Z-series (100 μm in total, z-steps every 5 μm) from the intratumoral region (-100 μm) to peritumoral region of a 6 day-old tumor (cytoplasm, red; nuclei, yellow). Perfused blood vessels (green) were visualized by FITC-dextran injection, irregular-shaped neo-vessels within the tumor and pre-existing linear-shaped outside of the tumor. Collagen fibers and muscle strands detected by second harmonic generation (blue). Excitation wavelength 880 nm. The movie corresponds to Fig. 9.

Movie 2. 3D rotation of multicellular tumor strand (red) cuffing a central blood vessel (green). Collective strand was computationally sectioned along the mid region of the strand containing a central blood vessel. The movie corresponds to Fig. 16.

Movie 3. Invasive growth, as defined by collective invasion and simultaneous mitotic activity. Time-lapse microscopy of a single z-plane within a relatively superficial collectively invading strand at 80 μm in depth that shows mitotic planes in perpendicular angle to the invasion direction. Frame rate, 9/min; duration, 30 min; excitation wavelength 880 nm. The movie corresponds to Fig. 17 to 19.

Movie 4. High-resolution reconstructions of radiosensitive and -resistant regions. Comparison of untreated control and irradiated tumor at day 14 after implantation. Movies start with a Z-projection of 250 μm and 120 μm in depth for control and irradiated tumor, respectively, followed by the corresponding z-series (nonprocessed slices from 150 to 50 μm in depth). Tumor cytoplasm (DsRed2, green), tumor nuclei (H2B-EGFP, cyan), and blood vessels and macrophages (Alexa Fluor 660-dextran, red). The movie corresponds to paragraph 3.5.1.3.

Quicktime Player installation file included on CD-ROM.

List of figures

- Figure 1. Cell morphologies and nomenclature of migration modes.
Figure 2. Types and variants of collective cell migration.
Figure 3. The tuning model of cell migration.
Figure 4. NIR and IR 2-photon excitation and emission spectra.
Figure 5. Photobleaching, phototoxicity, and tissue penetration of IR-MPM.
Figure 6. Deep IR 2-photon microscopy.
Figure 7. Deep tissue IR 2-photon microscopy of DsRed2 expressing xenografts in vivo.
Figure 8. Comparison of drop-on and injection methods of HT-1080 fibrosarcoma cells in the dorsal skin-fold chamber.
Figure 9. Near-infrared multiphoton microscopy of constitutive and tumor-induced blood vessels surrounding HT-1080 dual color tumors.
Figure 10. Phases of HT-1080 tumor growth.
Figure 11. Quantification of mitotic and apoptotic fractions. Intravital detection of nuclear morphology of tumor cells containing expressing H2B-EGFP.
Figure 12. Tumor growth and collective invasion dependent on temperature of mouse housing.
Figure 13. Invasion modes of HT-1080 dual color cells in vivo.
Figure 14. Collagen and fat tissue as guidance structures of invasion.
Figure 15. Invasion of HT-1080 cells along lymphatic vessels.
Figure 16. Collective invasion guided by pre-existing blood vessels.
Figure 17. Invasive growth: collective invasion coupled to proliferation in HT-1080 dual-color xenografts.
Figure 18. Collective invasion speed.
Figure 19. Mitotic activity in collective strands.
Figure 20. Uncoupling of mitotic activity from collective invasion.
Figure 21. Collective invasion pattern in human adult fibrosarcoma (primary lesion in subdiaphragmal location).
Figure 22. Melanoma growth after implantation into the mouse dermis.
Figure 23. Mitosis and apoptosis in tumor main masses of HT-1080, B16/F10 and MV3 xeno- and allografts.
Figure 24. Tissue destruction in B16/F10 allografts caused by absorption of laser light.
Figure 25. Collective melanoma invasion in skinfold chamber model.
Figure 26. Speed, mitosis and apoptosis in invading collective melanoma strands.
Figure 27. Radiotherapy of HT-1080 xenografts.
Figure 28. Impact of radiation therapy on mitosis and apoptosis rates in the main tumor mass.
Figure 29. Relative radioresistance of collective invasion strands.
Figure 30. Relative resistance to radiation-induced apoptosis in invasion strands but not the main tumor mass.
Figure 31. Quantification of the residual tumor mass in invasion strands after irradiation.
Figure 32. Relative radioresistance of invasion strands and disseminated single cells in MV3 tumors.
Figure 33. Response of HT-1080 xenografts to systemic chemotherapy with doxorubicin.
Figure 34. Contribution of EGF signaling on HT-1080 tumor growth and invasion.
Figure 35. Stable lentiviral shRNA knockdown of $\beta 1$ integrin.
Figure 36. Stable lentiviral knockdown of $\beta 3$ integrin in combination with $\beta 1$ integrin knockdown.
Figure 37. *In vitro* characterization of HT-1080 cells after stable knockdown of $\beta 1$ or $\beta 1$ with $\beta 3$.
Figure 38. Contribution of $\beta 1$ and $\beta 3$ integrins to tumor growth and survival.
Figure 39. Contribution of $\beta 1$ and $\beta 3$ integrins to individual and collective invasion.
Figure 40. Irradiation-induced regression after interferences with $\beta 1$ and $\beta 3$ integrins.
Figure 41. Increased radiosensitivity after interference with $\beta 1$ and $\beta 3$ integrins.
Figure 42. Perivascular invasive niche: stromal, cellular and molecular components and potential interaction sites.
Figure 43. Time scale and dosing overview for treatment of HT-1080 and MV3 xenografts.

List of tables

- Table 1. Ligand-binding specificities of human integrins.
- Table 2. Soluble factors that induce migration/are involved in metastatic dissemination secreted by stromal cells.
- Table 3. Established window models for cancer studies.
- Table 4. Clinical trials testing efficiency of integrin inhibitors.
- Table 5. Primary antibodies.
- Table 6. Isotypes.
- Table 7. Secondary antibodies.
- Table 8. Substances for *in vivo* use.
- Table 9. Selection antibiotics for shRNA cell line variants.
- Table 10. shRNA target sequences.

Acknowledgement

Though only my name appears on the cover of this dissertation, many people have contributed to its production. I owe my gratitude to all those people who have made this work possible and because of whom my graduate experience has been one that I will cherish forever.

My deepest gratitude is to my supervisor and mentor Prof. Peter Friedl. His infectious enthusiasm and unlimited zeal have been driving forces throughout all the years in his lab. Although not necessarily physically he has been always there to listen, and give support, advice and new ideas in many constructive discussions concerning all the small and big problems in research. Peter represents the guiding structure for my invasion into research.

Moreover, I want to thank all former and current members of the cell migration groups in Würzburg and Nijmegen who had always an open ear and a helping hand. A special thanks to Eva Riedel – her work increased my efficacy, and to Markus Hirschberg without whom routine intravital microscopy would have been never possible. I also appreciate technical assistance of “my” experienced technicians Monika Kuhn and Margit Ott, both being a continuous source of helping hands and comments. Thanks also to Dr. Gudrun Köhl from Regensburg, who supported my work especially in the early stages of working *in vivo*. Also thanks to Huib Croes, who got histochemistry started. Concluding this, I would like to repeat a sentence I wrote already in my master thesis: “Besides nice colleagues, I also found friends” – for life!

Also thanks to our collaborators, especially Dr. Stephan Kissler and his group, and givers of material – they also contributed to the success of this dissertation.

Furthermore, thanks to the members of my supervisory committee Prof. Helga Stopper and Prof. Manfred Scharl for fruitful discussions during the meetings and for reviewing this work.

Finally, I appreciate the support by Prof. Eva-Bettina Bröcker and Prof. Martin Lohse who let me work in their institutes although the group “migrated” to Nijmegen.

Last, but most importantly, thanks to my husband Steve, my parents, my family and my friends. They have been a constant source of love, concern, support, patience and strength all these years.

Stephanie Alexander, B.Sc., M.Sc.
Winterleitenweg 45, 97082 Wuerzburg, Germany
Phone: +49-931-35812062, Mobile: +49-157-73513199
Email: stephaniealexander@gmx.de

EDUCATION

- PhD Life Sciences, University of Wuerzburg 2006 – Present
- M.Sc. Biomedicine (with honors), University of Wuerzburg 2004 - 2006
- B.Sc. Biomedicine, University of Wuerzburg 2001 - 2004

RESEARCH EXPERIENCE

- Rudolf Virchow Center for Experimental Biomedicine and Department of Dermatology, University of Wuerzburg
Subgroup leader In Vivo Imaging 2008 - Present
(Cell dynamics laboratory Prof. P. Friedl)
PhD Thesis: *Collective cancer cell invasion in vivo: function of $\beta 1$ and $\beta 3$ integrins in perivascular invasion and resistance to therapy* 2006 - Present
Master Thesis: *Cancer cell invasion causes stressful nuclear deformation and genomic instability* 2005 - 2006
- Institute for Medical Radiology and Cell Research (MSZ), University of Wuerzburg
Bachelor Thesis: *Functional analysis of Spir-2 structural motifs – The novel KIND module as mediator of Spir/formin interaction* 2004

PUBLICATIONS

- **Alexander S.**, Andresen V, Heupel WM, Flucke U, Koehl GE, Hirschberg M, Flentje M, Hoffman RM, Geissler EK, Harms G, Friedl P. Combined integrin treatment prevents radioresistance of collective cancer invasion strands in vivo. (in revision)
- Wolf K, **Alexander S**, Schacht V, Coussens LM, von Andrian A, van Rheenen J, Deryugina E, Friedl P. Collagen-based cell migration models in vitro and in vivo. *Semin Cell Dev Biol.* 2009 Oct; 20(8):931-41.
- Imle A, Polzer B, **Alexander S**, Klein CA, Friedl P. Genomic instability of micronucleated cells revealed by single-cell comparative genomic hybridization. *Cytometry A.* 2009 July; 75(7):562-8.
- Andresen V, **Alexander S**, Heupel WM, Hirschberg M, Hoffman RM, Friedl P. Infrared multiphoton microscopy: subcellular-resolved deep tissue imaging. *Curr Opin Biotechnol.* 2009 Feb; 20(1): 54-62.
- **Alexander S**, Koehl GE, Hirschberg M, Geissler EK, Friedl P. Dynamic imaging of cancer growth and invasion: a modified skin-fold chamber model. *Histochem Cell Biol.* 2008 Dec; 130(6):1147-54.

SELECTED INVITED PRESENTATIONS

- Cooption of preexisting vessels conveys collective invasion and radioresistance in fibrosarcoma. 4th Goettingen Congress on Molecular & Optical Imaging. Bad Sooden, Germany. May 2009.
- Cell migration causes stressful nuclear deformation and DNA damage. 50th Symposium of the Society of Histochemistry. Interlaken, Switzerland. October 2008.
- From single-cell migration to invasive growth of cancer. Symposium Canceropôle PACA "Mechanisms of Invasion & Innovative Targeted Therapies in Head and Neck Cancer". Nice, France. April 2008.

SELECTED MEETING ABSTRACTS

- **Alexander S**, Flucke U, Koehl GE, Hirschberg M, Flentje M, Geissler EK, Friedl P. Cooption of preexisting blood vessels conveys collective invasion and radioresistance in fibrosarcoma. 100th AACR Annual Meeting. Denver, USA. April 2009.
- **Alexander S**, Koehl GE, Hirschberg M, Hoffman RM, Geissler EK, Friedl P. Collective cancer cell invasion along blood and lymph vessels. 1st International Kloster Seeon Meeting of the DFG SPP1190 "The tumor – vessel interface". Seeon, Germany. September 2007.
- **Alexander S**, Wolf K, Friedl P. Physical limits of cancer cell migration by shape change and deformation. 34th Annual Conference of the ADF (Arbeitsgemeinschaft Dermatologische Forschung). Freiburg, Germany. March 2007.

AWARDS & FELLOWSHIPS

- 1st Poster Prize of the Kloster Seeon "Tumor-vessel" Meeting, 2009
- Best students' Poster of Rudolf Virchow Center Retreat, 2009
- Travel Award of the Jubilaeumsstiftung of the University of Wuerzburg, 2009
- Young Scientist Award 2008 (to Experimental Cancer Research) of the Society for Histochemistry, 2008

SUPERVISION EXPERIENCE

- Supervision of Bachelor and Master Students 2008
- Supervision and training of technicians and trainees 2006 - Present

PERSONAL SKILLS AND QUALIFICATIONS

- *Non-Scientific trainings:*
Effective Scientific Writing, Poster Design, Presentation Techniques, Project management in research
- *Scientific trainings:*
Immunohistochemistry, Statistics

ACTIVITIES

- Speaker of the Doctoral Students' Council 2007 - 2008
Graduate School of Life Sciences, University of Wuerzburg
- Organisation of the 2nd Young Scientist Meeting 2007 - 2008
Priority Program "Tumor-vessel Interface",
Deutsche Forschungsgemeinschaft

- Co-organizer 3rd International Symposium of the International Graduate School, University of Wuerzburg 2007
- Students' Speaker, Undergraduate program Biomedicine, University of Wuerzburg 2002 - 2006

REFERENCES

- Prof. Dr. Peter Friedl
Microscopical Imaging of the Cell
Department of Cell Biology (283)
NCMLS, Radboud University Nijmegen Medical Centre
P.O. Box 9101
6500 HB Nijmegen
The Netherlands

Phone: +31.24.3610907 (office)
E-mail: P.Friedl@ncmls.ru.nl
- Prof. Dr. Martin Lohse
Rudolf Virchow Center
DFG Research Center for Experimental Biomedicine
University of Wuerzburg
Versbacher Str. 9
97078 Wuerzburg
Germany

Phone: +49.931.201.48401
Email: lohse@toxi.uni-wuerzburg.de
- Prof. Dr. Eva-Bettina Bröcker
Department of Dermatology
University of Wuerzburg
Josef-Schneider-Str. 2
97080 Wuerzburg

Phone: +49.931.201.26350
Email: Broecker_E@klinik.uni-wuerzburg.de

Würzburg, April 30th 2010

Stephanie Alexander

Affidavit

(Eidesstattliche Erklärung)

I hereby declare that my thesis entitled:

“Collective cancer cell invasion *in vivo*: function of β 1 and β 3 integrins in perivascular invasion and resistance to therapy”

is the result of own work. I did not receive any help or support from commercial consultants. All sources and / or materials applied are listed and specified in the thesis.

Furthermore, I verify that this thesis has not yet been submitted as part of another examination process neither in identical nor in similar form.

Würzburg, 30.April 2010
Date

Signature